

**CHARACTERIZATION OF CONJUGATED
POLYELECTROLYTES FOR NUCLEIC ACID
SENSING, GENE DELIVERY AND IMAGING**

**A Thesis Submitted to
the Graduate School of Engineering and Sciences of
İzmir Institute of Technology
in Partial Fulfillment of the Requirements for the Degree of**

DOCTOR OF PHILOSOPHY

in Bioengineering

**by
Müge YÜCEL**

**July 2022
İZMİR**

ACKNOWLEDGMENTS

First of all, I would like to thank my advisor Assoc. Prof. Dr. Ümit Hakan YILDIZ for introducing me to polymer science, for his outstanding knowledge, experience, and his endless support, encouragement, and motivation throughout my postgraduate study. Besides, I would like to thank Prof. Dr. Franziska Gröhn for her guidance in scattering analysis. Additionally, I would like to thank Assoc. Prof. Dr. Altuğ KOÇ for his excellent guidance in medical genetics. I am also thankful to Assoc. Prof. Dr. Ahu ARSLAN YILDIZ and Dr. Özge TÜNCEL for their knowledge and help in cell culture studies.

I would like to express my deepest gratitude to my mother Fatma YÜCEL and especially to my father Ahmet H. YÜCEL who is always believing in me and unwaveringly supporting me in my life. I am also very grateful to my friend and collaborator Gün Deniz AKKOÇ for his remarkable knowledge in chemometrics and software development, as well. Additionally, I am very thankful to my sisters Özge ERGUN and Hilmiye ERK for their caring and valuable advice. Besides, I would like to thank Sezer ÖZENLER, Hakan KAYA, Soner KARABACAK, and the members of BioSens&BioApps research group with all the alumni.

This study is supported by the The Scientific and Technological Research Council of Turkey, TÜBİTAK Project: 116Z547. Besides, I would like to acknowledge the support of the Scientific and Technological Research Council of Turkey 2214-A International Doctoral Research Fellowship Programme for Ph.D and Council of Higher Education (CoHE) in the field of Sensor Technologies within the scope of 100/2000 Programme by CoHE.

ABSTRACT

CHARACTERIZATION OF CONJUGATED POLYELECTROLYTES FOR NUCLEIC ACID SENSING, GENE DELIVERY AND IMAGING

In this thesis, cationic derivatives of poly(3-alkylmethoxythiophene) (PT) which are a class of conjugated polyelectrolytes (CPE), have been synthesized. PT has been polymerized via FeCl_3 oxidative polymerization, were treated in a set of solvents to elaborate coil conformation of polymer chain in different physicochemical environment. Spectroscopic and scattering techniques have ascertained that ethylene glycol is a good solvent for PT regarding Flory-Huggins theory. The smaller interaction parameter of PT with respect to ethylene glycol than water drives a thermodynamically driven ultra-small particle (Pdot) formation in aqueous phase by a rapid nanophase separation between PT-rich ethylene glycol and PT-poor water phase. All CPEs have been then employed to prepare single polymer chain polymer dots (Pdot) by “nanophase separation” method. As a next step, Pdots have been characterized in terms of optical and colloidal properties that they possess in the backbone conformations altered by solvation effect. Regarding their colloidal characteristic, translocation of Pdot into cancerous cells was analyzed compared to healthy cells by 2D cell culture and co-culture studies. It has reported that Pdots have ability to penetrate through nuclear envelope in hepatocellular carcinoma whereas accumulate around nucleus of healthy liver cells in cytoplasm. Additionally, Pdots were studied in breast cancer cell lines to understand the behavior of Pdot staining in 2D cell culture of invasive and non-invasive breast cancer types. The findings suggest that Pdots are prone to penetrate into the invasive cancerous cells attributed to the greater deformations on nucleus membrane of triple negative breast cancer cells. In a next application, the enhanced photophysical property of PT exhibited in ethylene glycol media allows PT to be utilized as a fluorescent probe for determination of single nucleotide polymorphism by a non-amplification-based protocol. Fluorescence emission at specific wavelengths resulted from very distinct conformations of PT chain is the key elements for the SNP detection assay. The evaluation of optical data obtained from the probe with principal component analysis proves the separation of healthy individuals from patients with an overall 96% accuracy.

ÖZET

NÜKLEİK ASİT ALGILAMA, GEN İLETİMİ VE GÖRÜNTÜLEMESİ İÇİN KONJUGE POLİELEKTROLİTLERİN KARAKTERİZASYONU

Bu tezde, konjuge polielektrolitlerin (CPE) bir sınıfı olan poli(3-alkilmetoksitiyofen) (PT)'nin katyonik türevleri sentezlenmiştir. FeCl₃ oksidatif polimerizasyonu sonucu elde edilen PT'nin zincir konformasyonunun anlaşılması için farklı fizikokimyasal özelliğe sahip çözücüler içinde incelenmiştir. Spektroskopik ve saçılma teknikleri, Flory-Huggins teorisine göre etilen glikolün PT için iyi bir çözücü olduğunu belirlemiştir. PT-etilen glikol arasındaki etkileşim parametresinin PT – su arasındakine göre daha küçük oluşu PT'den zengin etilen glikol ve PT'den fakir su fazı arasında hızlı bir nanofaz ayrımı ile sulu fazda termodinamik olarak elverişli ultra küçük Pdot oluşumunu yönlendirir. Tüm CPE'ler daha sonra "nanofaz ayırma" yöntemiyle tek polimer zincirli polimer noktaları (Pdot) hazırlamak için kullanılmıştır. Bir sonraki adım olarak, Pdot'lar, solvasyon etkisiyle değiştirilen omurga konformasyonlarında sahip oldukları optik ve kolloidal özellikler açısından karakterize edilmiştir. Pdot'ların bu özelliği ile ilgili olarak, kanserli hücrelerdeki translokasyonu, 2D hücre kültürü ve ortak kültür çalışmaları ile sağlıklı hücrelere kıyasla analiz edildi. Pdot'ların hepatosellüler karsinomda nükleer zarftan geçme kabiliyetine sahip olduğunu, sitoplazmada sağlıklı karaciğer hücrelerinin çekirdeği etrafında biriktiğini bildirmiştir. Ek olarak, invaziv ve invaziv olmayan meme kanseri türlerinin 2D hücre kültüründe Pdot boyamanın davranışını anlamak için meme kanseri hücre dizilerinde Pdot'lar üzerinde çalışılmıştır. Bulgular, üçlü negatif meme kanseri hücrelerinin çekirdek zarındaki daha büyük deformasyonlara atfedilen istilacı kanserli hücrelere Pdot'ların daha fazla nüfuz ettiğini göstermektedir. Ayrıca, etilen glikol ortamında sergilenen gelişmiş fotofiziksel özellik, PT'nin, amplifikasyona dayalı olmayan bir protokolle tek nükleotid polimorfizminin belirlenmesi için bir floresan prob olarak kullanılmasına olanak sağlar. PT zincirinin değiştirilebilir konformasyonlarından kaynaklanan farklı dalga boylarındaki floresan emisyonu, konjuge polielektrolit tabanlı SNP saptama analizi için temel unsurdur. Probdan elde edilen optik verilerin temel bileşen analizi ile değerlendirilmesi, sağlıklı bireylerin hastalardan ayrıldığını genel olarak %96 doğrulukla kanıtlamaktadır.

Dedicated to my father...

TABLE OF CONTENTS

LIST OF FIGURES	ix
LIST OF TABLES	xvi
CHAPTER 1. INTRODUCTION	1
1.1. Motivation and Scope of the Thesis	1
1.2. Conjugated Polyelectrolytes	2
1.3. Polymer Dots and Polymer Nanoparticles	5
1.4. Characterization Methods of Conjugated Polyelectrolytes	8
1.4.1. Fluorescence Spectroscopy	8
1.4.2. Light Scattering	9
1.4.3. Fluorescence Microscopy	12
CHAPTER 2. SYNTHESIS AND CHARACTERIZATION OF CATIONIC POLYELECTROLYTES	14
2.1. Synthesis of Poly(1,4-dimethyl-1-(3-((4-methyl thiophen-3-yl)oxy)propyl)piperazin-1-ium bromide) – PT1	15
2.1.1. Synthesis of 3-Methoxy-4-methylthiophene	15
2.1.2. Synthesis of 3(3-Bromo)propoxy-4-methylthiophene	16
2.1.3. Synthesis of 1,4-Dimethyl-1-(3-((4-methyl thiophen-3-yl)oxy)propyl)piperazin-1-ium bromide	17
2.1.4. Synthesis of Poly(1,4-dimethyl-1-(3-((4-methyl thiophen-3-yl)oxy)propyl)piperazin-1-ium bromide)	19
2.2. Synthesis of Poly(N-allyl-N-methyl-N-(3-((4-methyl thiophen-3-yl)oxy)propyl)prop-2-en-1-aminium bromide)	20
2.2.1. Synthesis of N-allyl-N-methyl-N-(3-((4-methyl thiophen-3-yl)oxy)propyl)prop-2-en-1-aminium bromide	20
2.2.2. Synthesis of Poly(N-allyl-N-methyl-N-(3-((4-methyl thiophen-3-yl)oxy)propyl)prop-2-en-1-aminium bromide)	22
2.3. Synthesis of Poly(1-(3-((4-methylthiophen-3-yl) oxy)propyl-1,4-diazabicyclo[2.2.2]octan-1-ium)	23
2.3.1. Synthesis of 1-(3-((4-methylthiophen-3-yl)oxy) propyl-1,4-diazabicyclo[2.2.2]octan-1-ium)	23
2.3.2. Synthesis of Poly(1-(3-((4-methylthiophen-3-yl)oxy) propyl-1,4-diazabicyclo[2.2.2]octan-1-ium)	24

2.4. Characterization of Cationic Polyelectrolytes	25
CHAPTER 3 PREPARATION AND CHARACTERIZATION OF CONJUGATED POLYMER DOTS	31
3.1. Materials and Methods	33
3.2. Results and Discussion	34
3.2.1. Optical Characterization of CPE and Pdot.....	35
3.2.2. Colloidal characterization of CPE and Pdot.....	44
3.2.2.1. Polyelectrolyte - Water System.....	44
3.2.2.2. Polyelectrolyte / Pdot - Ethylene Glycol System.....	46
3.2.2.3. Polyelectrolyte / Pdot - Dimethyl Sulfoxide System	52
3.2.2.4. Polyelectrolyte /Pdot - 1,4-Butanediol System	57
3.3. Polyelectrolyte - DNA Complexation	61
CHAPTER 4 SELECTIVE DETERMINATION OF HEPATOCELLULAR CARCINOMA CELLS BY POLYMER DOTS	67
4.1. Materials and Methods	68
4.2. Results and Discussion	70
CHAPTER 5 PCR-FREE PROTOCOL FOR NUCLEIC ACID DETECTION BY CONJUGATED POLYELECTROLYTE.....	81
5.1. Introduction	81
5.2. Materials and Method.....	84
5.3. Results and Discussion	86
CHAPTER 6 NUCLEAR PENETRATION OF PDOT IN BREAST CANCER CELL TYPES.....	96
6.1. Materials and Methods	97
6.2. Results and Discussion	98
CHAPTER 7 CONCLUSION	105

LIST OF FIGURES

<u>Figure</u>	<u>Page</u>
Figure 1.1. Schematic representation of interaction between conjugated polyelectrolyte and DNA probe. ¹⁶	3
Figure 1.2. Schematic representation of conjugated polythiophene based assay for detection of miRNA. ¹⁹	4
Figure 1.3. Effect of conjugation length on the orbital band gap of a polyelectrolyte. ²⁷	5
Figure 1.4. Schematic representations for preparation of conjugated polymer nanoparticle by a) miniemulsion and b) nanoprecipitation methods.	6
Figure 1.5. Protocol for preparation of single-chain polymer dots (sPdot). ⁴⁴	7
Figure 1.6. Jablonski diagram of photophysical processes. ⁴⁷	8
Figure 1.7. Schematic for the light scattering process, including detection of the scattered intensity (I) at scattering angle (θ). ⁵¹	10
Figure 1.8. Image of ALV multi angular dynamic and static light scattering set-up.	11
Figure 1.9. Basic setup of an inverted widefield fluorescence microscope. ⁵⁸	13
Figure 2.1. Synthesis of 3-methoxy-4-methylthiophene (precursor 1 (PC1)).	15
Figure 2.2. ¹ H NMR spectrum of Precursor 1.	16
Figure 2.3. Synthesis of 3(3-bromo)propoxy-4-methylthiophene (precursor 2 (PC2)).	16
Figure 2.4. ¹ H NMR spectrum of Precursor 2.	17
Figure 2.5. Synthesis of monomer 1 (M1) 1,4-dimethyl-1-(3-((4-methylthiophen-3-yl)oxy)propyl)piperazin-1-ium bromide.	17
Figure 2.6. ¹ H NMR spectrum of 1,4-dimethyl-1-(3-((4-methylthiophen-3-yl)oxy)propyl)piperazin-1-ium bromide.	18
Figure 2.7. Mass spectrum of 1,4-dimethyl-1-(3-((4-methylthiophen-3-yl)oxy)propyl)piperazin-1-ium bromide.	18
Figure 2.8. ¹ H NMR spectrum of poly(1,4-dimethyl-1-(3-((4-methylthiophen-3-yl)oxy)propyl)piperazin-1-ium bromide) (PT1).	19
Figure 2.9. Synthesis of monomer 2 (M2) N-allyl-N-methyl-N-(3-((4-methylthiophen-3-yl)oxy)propyl)prop-2-en-1-aminium bromide.	20

<u>Figure</u>	<u>Page</u>
Figure 2.10. ¹ H NMR spectrum of N-allyl-N-methyl-N-(3-((4-methylthiophen-3-yl)oxy)propyl)prop-2-en-1-aminium bromide.....	21
Figure 2.11. Mass spectrum of N-allyl-N-methyl-N-(3-((4-methylthiophen-3-yl)oxy)propyl)prop-2-en-1-aminium bromide.....	21
Figure 2.12. Synthesis of polyelectrolyte (PT2) Poly(N-allyl-N-methyl-N-(3-((4-methylthiophen-3-yl)oxy)propyl)prop-2-en-1-aminium bromide).....	22
Figure 2.13. ¹ H NMR spectrum of poly(N-allyl-N-methyl-N-(3-((4-methylthiophen-3-yl)oxy)propyl)prop-2-en-1-aminium bromide).....	22
Figure 2.14. Synthesis of monomer 3 (M3) 1-(3-((4-methylthiophen-3-yl)oxy)propyl)-1,4-diazabicyclo[2.2.2]octan-1-ium.	23
Figure 2.15. ¹ H NMR spectrum of 1-(3-((4-methylthiophen-3-yl)oxy)propyl)-1,4-diazabicyclo[2.2.2]octan-1-ium.....	23
Figure 2.16. Mass spectrum of 1-(3-((4-methylthiophen-3-yl)oxy)propyl)-1,4-diazabicyclo[2.2.2]octan-1-ium.....	24
Figure 2.17. ¹ H NMR spectrum of poly(1-(3-((4-methylthiophen-3-yl)oxy)propyl)-1,4-diazabicyclo[2.2.2]octan-1-ium) (PT3).....	25
Figure 2.18. a) Absorption and b) fluorescence spectra of polythiophene (PT) derivatives dissolved in water.....	26
Figure 2.19. Absorption spectra of cationic polyelectrolyte derivative (PT3) dissolved in a) water, b) ethylene glycol, c) DMSO, d)Tris-EDTA buffer, e) THF, f) glycerol, g) methanol, h) 2-propanol, i) acetonitrile, j) nitromethane, k) DMF, and l)propylene carbonate.....	27
Figure 2.20. Steady-state fluorescence spectra of cationic polyelectrolyte derivative (PT3) dissolved in a) water, b) ethylene glycol, c) DMSO, d)Tris-EDTA buffer, e) THF, f) glycerol, g) methanol, h) 2-propanol, i) acetonitrile, j) nitromethane, k) DMF, and l)propylene carbonate (each solution was excited at corresponding absorption wavelengths).....	28
Figure 2.21. Absorbance spectra of PT3 dissolved in EG a) before and b) after filtration.	29
Figure 3.1. Schematic representation of Pdot formation by “nanophase separation” method between CPE-rich ethylene glycol phase and CPE-poor water phase.	31

<u>Figure</u>	<u>Page</u>
Figure 3.2. Illustration of the phase diagrams in polymer solutions showing the good and poor solvent regions and the demarcations for athermal (B=0) and theta solvents. ⁶⁰	32
Figure 3.3. UV-Vis absorbance spectra of 1.85×10^{-3} M polyelectrolyte solutions of water, ethylene glycol, DMSO and BDO.	35
Figure 3.4. Fluorescence spectra of PT3 in water with excitation wavelengths 360 nm (black trace) and 410 nm (red trace).	36
Figure 3.5. Fluorescence spectra of a) PT3 in ethylene glycol and b) Pdot with excitation wavelengths 350 nm (black trace) and 415 nm (red trace).....	37
Figure 3.6. Fluorescence spectra of a) PT1 in DMSO and b) Pdot with excitation wavelengths 330/360 nm (black trace) and 460/420 nm (red trace) for DMSO and Pdot(DMSO), respectively.	38
Figure 3.7. Fluorescence spectra of a) PT1 in BDO and b) Pdot with excitation wavelengths 330 nm (black trace) and 370 nm (red trace).	39
Figure 3.8. Fluorescence lifetime decay of PT1 dissolved in water.	41
Figure 3.9. Fluorescence lifetime decay of PT1 dissolved in ethylene glycol (left) and Pdot (right).....	41
Figure 3.10. Fluorescence lifetime decay of PT1 dissolved in DMSO (left) and Pdot (right).....	42
Figure 3.11. Fluorescence lifetime decay of PT1 dissolved in BDO (left) and Pdot (right).	42
Figure 3.12. DLS: electric field autocorrelation function $g_1(\tau)$ and distribution of scattering relaxation times $A(\tau)$ of PT1 in water at a scattering angle of $\Theta = 90^\circ$	44
Figure 3.13. a) Diffusion coefficient from dynamic light scattering (DLS) and b) Zimm plot from SLS of PT1 in water obtained.	45
Figure 3.14. DLS: electric field autocorrelation function $g_1(\tau)$ and distribution of scattering relaxation times $A(\tau)$ of PT1 in ethylene glycol (EG) at a scattering angle of $\Theta = 90^\circ$	46
Figure 3.15. a) Diffusion coefficient from DLS and b) Zimm plot from SLS of PT1 in ethylene glycol (EG).	47

<u>Figure</u>	<u>Page</u>
Figure 3.16. DLS: electric field autocorrelation function $g^1(\tau)$ and distribution of scattering relaxation times $A(\tau)$ of Pdot(EG) at a scattering angle of $\Theta = 90^\circ$	48
Figure 3.17. a) Diffusion coefficient plot from DLS and b) Zimm plot from SLS of Pdot(EG).	49
Figure 3.18. Dynamic light scattering electric field autocorrelation function $g_1(\tau)$ and distribution of scattering relaxation times $A(\tau)$ of Pdot(EG) at a scattering angle of $\Theta = 90^\circ$ with increasing volume fraction ranging from 2.4 to 85.	49
Figure 3.19. Light scattering analysis of Pdot(EG) with concentrations a) 0.94, b) 1.87,c) 3.74, d) 7.49, e)11.2, and f) 15.0 mM. $g_1(\tau)$ autocorrelation functions and scattering intensity plot demonstrated at the left and right, respectively.	52
Figure 3.20. Dynamic light scattering electric field autocorrelation function $g_1(\tau)$ and distribution of relaxation times $A(\tau)$ of PT1 in DMSO at a scattering angle of $\Theta = 90^\circ$	53
Figure 3.21. a) Diffusion coefficient from DLS and b) Zimm plot from SLS of PT1 in DMSO.....	54
Figure 3.22. Dynamic light scattering electric field autocorrelation function $g_1(\tau)$ and distribution of relaxation times $A(\tau)$ of Pdot(DMSO) at a scattering angle of $\Theta = 90^\circ$	55
Figure 3.23. a) Diffusion coefficient from DLS and b) Zimm plot from SLS of Pdot(DMSO).....	55
Figure 3.24. DLS: a) electric field autocorrelation function $g_1(\tau)$ and b) relaxation time distribution $A(\tau)$ for Pdot(DMSO) with DMSO volume fraction from 2.4 to 67.	57
Figure 3.25. DLS: electric field autocorrelation function $g_1(\tau)$ and relaxation time distributions $A(\tau)$ of PT1 in 1,4-BDO at a scattering angle of $\Theta = 90^\circ$	58
Figure 3.26. a) Diffusion coefficient from DLS and b) Zimm plot from SLS of PT1 dissolved in BDO.....	58

<u>Figure</u>	<u>Page</u>
Figure 3.27. DLS: electric field autocorrelation function $g_1(\tau)$ and relaxation time distribution $A(\tau)$ of Pdot(BDO) at a scattering angle of $\Theta = 90^\circ$	59
Figure 3.28. a) Diffusion coefficient from DLS and b) Zimm plot from SLS of Pdot(BDO).....	60
Figure 3.29. Schematic for cationic conjugated polythiophene (PT) and DNA complexation.	61
Figure 3.30. Fluorescence titration spectra of PT1 dissolved in water with ssDNA.....	62
Figure 3.31. Fluorescence titration spectra of a) PT1 dissolved in EG and b) Pdot (EG) with ssDNA.	63
Figure 3.32. Fluorescence titration spectra of a) PT1 dissolved in DMSO and b) Pdot(DMSO) with ssDNA.....	64
Figure 3.33. Fluorescence titration spectra of a) PT1 dissolved in BDO and b) Pdot(BDO) with ssDNA.....	65
Figure 3.34. Fluorescence titration spectra of Pdot(EG) having increasing ethylene glycol volume fraction (Φ) a) 2.4, b) 3.3, c) 4.9, d) 9.8, e) 19, and f) 50 with ssDNA.	66
Figure 4.1. Schematic illustration of nanophase separation between ethylene glycol (EG) and water during Pdot formation.	67
Figure 4.2. a) UV-Vis and b) fluorescence spectra of conjugated PT1 dissolved in ethylene glycol (black trace) and Pdot (red trace).....	70
Figure 4.3. a) Dynamic light scattering electric field autocorrelation function $g_1(\tau)$ and b) size distribution of Pdots (inset photograph shows 60 μ M Pdot solution).....	71
Figure 4.4. a) AFM image of Pdots on mica surface. b) Histogram height distribution of Pdots measured by AFM topography.	72
Figure 4.5. Theoretical calculation of end-to-end distance and length of a step.	73
Figure 4.6. a) Confocal microscope image of Pdots in culture medium (inset image is the 100x magnification of the selected Pdot). b) Fluorescence intensity variation of single Pdot tracked in 80 seconds.	74
Figure 4.7. Fluorescence intensity variations of 7 individual Pdots.....	75

<u>Figure</u>	<u>Page</u>
Figure 4.8. a, c) Bright field and b, d) fluorescence confocal images of HuH-7 and THLE-2 cells, respectively. e) Fluorescence intensity ratio of nucleus to cytoplasm from the images shown in Figure 2a-d).....	76
Figure 4.9. Concentration dependent cell imaging study of the 40, 60, and 100 μ M Pdots.	77
Figure 4.10. The localization of Pdot in the nucleus of HuH-7 with phases of mitotic divisions in the cell cycle; a) prophase, b) pro-metaphase, c) metaphase, d) anaphase, e) telophase, f) cytokinesis, and g) newly divided cells.....	78
Figure 4.11. Confocal micrographs of co-cultured THLE-2 and HuH-7 cells a) 20X magnification and b) 100X magnification. c) Fluorescence intensity ratio of nucleus to cytoplasm.....	79
Figure 4.12. a) The images of merged DAPI and Pdot staining co-culture medium. b) only DAPI, and c) only Pdot staining of co-culture.....	80
Figure 5.1. Schematic representation of steps involved in polymerase chain reaction (PCR) protocol. ⁹⁷	83
Figure 5.2. Exponential growth of template DNA in each PCR cycle. (Source: Andy Vierstraete, 1999)	84
Figure 5.3. Schematic of four-stepped PCR-free assay based on conjugated polyelectrolyte. HG: human genome, WT: wild type primer, MT: mutant type primer, HZW: homozygous wild type human genome, HZM: homozygous mutant type human genome, HTZ: heterozygous human genome. ⁹	86
Figure 5.4. a) Fluorescence analysis of PT2 (1.8 mM of 200 μ L) quenched by wild type primer in the concentration between 0 (top) to 108 ng/ μ L). b) Stern-Volmer plot of Figure 5.4a.	88
Figure 5.5. Schematic illustration of hybridization step for HZW samples.	89
Figure 5.6. a) Fluorescence intensity profile at 525 nm of rWT-CPE (orange) and rMT-CPE (pink) complexes of 12 HZW healthy samples and b) typical fluorescence spectra of collected from sample 8 (0.9 mM of 20 μ L of CPE was used in fluorescence analyses).....	90
Figure 5.7. Schematic illustration of hybridization step for HZM samples.	91

<u>Figure</u>	<u>Page</u>
Figure 5.8. a) Fluorescence intensity profile at 525 nm of rWT-CPE (orange) and rMT-CPE (pink) complexes of 14 HZM and HTZ samples and b) typical fluorescence spectra of collected from sample 5 (0.9 mM of 20 μ L of PT2 was used in fluorescence analyses).....	91
Figure 5.9. Melting curve of the MEFV gene variations; M694V-heterozygous, V694V-homozygous mutant and M694M-homozygous wild.....	92
Figure 5.10. Real time-PCR results indicating the melting temperatures of MEFV gene variations (M694V, V694V and M694M). Inset figure represents the data of total 26 genomic DNA studied in this work.	93
Figure 5.11. 2D PCA scores of all samples along with the decision boundary obtained by SVM classification.....	94
Figure 5.12. Loadings plot for principal component 1 (PC1).....	95
Figure 6.1. a) Schematic representation of polymer dot (Pdot) formation. b) DLS autocorrelation function $g_1(t)$ of Pdot with size distribution. c) Fluorescence spectra of PT and Pdot.	97
Figure 6.2. Fluorescence microscope images of MCF-7 cells (10000 cells/well) incubated in a) Pdot and b) DAPI. (20X magnification).....	100
Figure 6.3. A typical normalized fluorescence images of a) Pdot, b) DAPI in MCF-7 cells, and c) matrix difference of images a and b.	100
Figure 6.4. Fluorescence microscope images of MDA-MB-231 cells (10000 cells/well) incubated in a) Pdot and b) DAPI. (20X magnification)	101
Figure 6.5. A typical normalized fluorescence images of a) Pdot, b) DAPI in MDA-MB-231 cells, and c) matrix difference of images a and b.....	102
Figure 6.6. Fluorescence microscope images of NIH 3T3 cells (10000 cells/well) incubated in a) Pdot and b) DAPI. (20X magnification).....	102
Figure 6.7. A typical normalized fluorescence images of a) Pdot, b) DAPI in NIH 3T3 cells, and c) matrix difference of images a and b.	103
Figure 6.8. Average red and blue intensities from Pdot and DAPI, respectively for 30 cells for each cell lines.	104

LIST OF TABLES

<u>Table</u>	<u>Page</u>
Table 1.1. ρ -ratio for common morphologies. ⁵¹	12
Table 2.1. Chemical structures molecular weights of monomers and polymers.	14
Table 2.2. Fluorescence quantum yield of cationic polyelectrolyte (PT3) dissolved in selected solvents from Figure 2.19 and 20.	29
Table 3.1. Photophysical data of PT1 dissolved in water, ethylene glycol, DMSO, 1,4-BDO and Pdot forms of polyelectrolyte in each solvent.	40
Table 3.2. Fluorescence lifetime relaxation times and their relative abundance of polyelectrolyte dissolved in water, ethylene glycol, DMSO, BDO and Pdot forms of polyelectrolyte in each solvent.	43
Table 3.3. Dynamic and static light scattering data of Pdot(EG) with increasing volume fraction of EG ranging from 0 to 100 volume fraction.	50
Table 3.4. Structural data of Pdot(EG) concentration study from light scattering analysis.	52
Table 3.5. Dynamic and static light scattering data for Pdot(DMSO) having DMSO volume fraction (ϕ) ranging from 2.4 to 67.	56
Table 3.6. Overall structural data from dynamic and static light scattering of polyelectrolyte in water, ethylene glycol, DMSO, BDO and their corresponding Pdot forms.	60

CHAPTER 1

INTRODUCTION

1.1. Motivation and Scope of the Thesis

In this thesis, synthesis and characterization of poly(3-alkylthiophene) type conjugated polyelectrolyte were described. Monomers of 3-alkylthiophenes were synthesized using 3-alkylmethoxythiophene as starting precursor. Monomers, 1,4-dimethyl-1-(3-((4-methylthiophen-3-yl)oxy)propyl)piperazin-1-ium bromide, N-allyl-N-methyl-N-(3-((4-methylthiophen-3-yl)oxy)propyl)prop-2-en-1-aminium bromide, and 1-(3-((4-methylthiophen-3-yl)oxy)propyl)-1,4-diazabicyclo[2.2.2]octan-1-ium were polymerized via FeCl_3 catalyzed oxidative polymerization. Poly(3-alkylthiophene) type conjugated polyelectrolytes were then used nucleotide detection and imaging purposes. This thesis describes the potential of poly(3-alkylthiophene) type polyelectrolytes and utilization their optical properties for determination of biomarkers and imaging of cancer cells.

Conjugated polyelectrolytes (CPEs) which show two distinct conformations (random coil and planar) are affected by pH, temperature, ionic strength, and the presence of other charged small or macro molecules. The transition occurred due to those influences in backbone conformation allows CPE to be used as fluorescent probe in determination of biological materials (nucleic acids, protein, enzyme, etc.) and cells. Moreover, notable advances have been achieved in the field of bio-imaging, targeted drug delivery, and photodynamic therapy began with the invention of polymer dots (Pdots) produced from conjugated polyelectrolytes. The photophysical and colloidal characteristics of Pdot having enhanced absorption coefficient (ϵ), fluorescence quantum yield and reduced particle size (around 2-30 nm) have contributed to biological and medical sciences. For the nucleus staining study, Pdots prepared from cationic conjugated polyelectrolyte by “nanophase separation” method which has been recently patented by Turkish Patent and Trademark Office will be investigated in this thesis.

This thesis consists of six chapters, Chapter 1 and 2 describes the introductory and experimental section for poly(3-alkylthiophene) type conjugated polyelectrolyte. In

Chapter 3, solvation effect on polyelectrolyte conformation and Pdot formation by “nanophase separation” are investigated by the aspect of optical and colloidal characteristics. Chapter 4 represents an application for hepatocellular carcinoma cell imaging by Pdot. As another application of conjugated polyelectrolyte, a PCR-free methodology developed for detection of single nucleotide polymorphism is discussed in Chapter 5. The following chapter covers the image analysis of Pdot for differentiation of breast cancer cell types.

1.2. Conjugated Polyelectrolytes

Functionalization of conjugated polymers by cationic, anionic, and ionizable groups yields water-soluble conjugated polyelectrolytes (CPE). The typical cationic conjugated polyelectrolyte is obtained by quaternary ammonium and pyridinium while anionic CPEs are designed by carboxylate, phosphonate, and sulfonate functional groups.¹ Conjugated polyelectrolytes have been synthesized with variety of chemical structure by different methodology which are mostly carbon-carbon bond forming reactions over the 30 years. The well-established polymerization methods include FeCl_3 and electrochemical oxidation, the Yamamoto and Suzuki couplings, or the Wittig, Gilch, and Heck reactions.^{2,3}

Over the years, conjugated polyelectrolytes have been attracted in numerous field such as organic light-emitting diodes (OLEDs), solar cells, and sensors due to their tunable optical and electrical characteristics.⁴⁻⁶ Among several types of CPEs, polythiophene-based CPEs are emerging as interesting class of polymer due to conformation induced optical transition. Conjugated polythiophene (PT) can exist in two different spatial conformations; random coil and planar, and the PT conformations are affected by the presence of small or macro charged structures and environmental factors such as pH, temperature. These two conformations are distinguished by colorimetric or spectroscopic methods such as absorbance and fluorescence spectrophotometers.^{7,8} Since the cationic form of polythiophene can switch between the aforementioned conformations, it is widely studied for the determination of single-stranded DNA (ssDNA) and double-stranded DNA (dsDNA).⁹⁻¹⁵

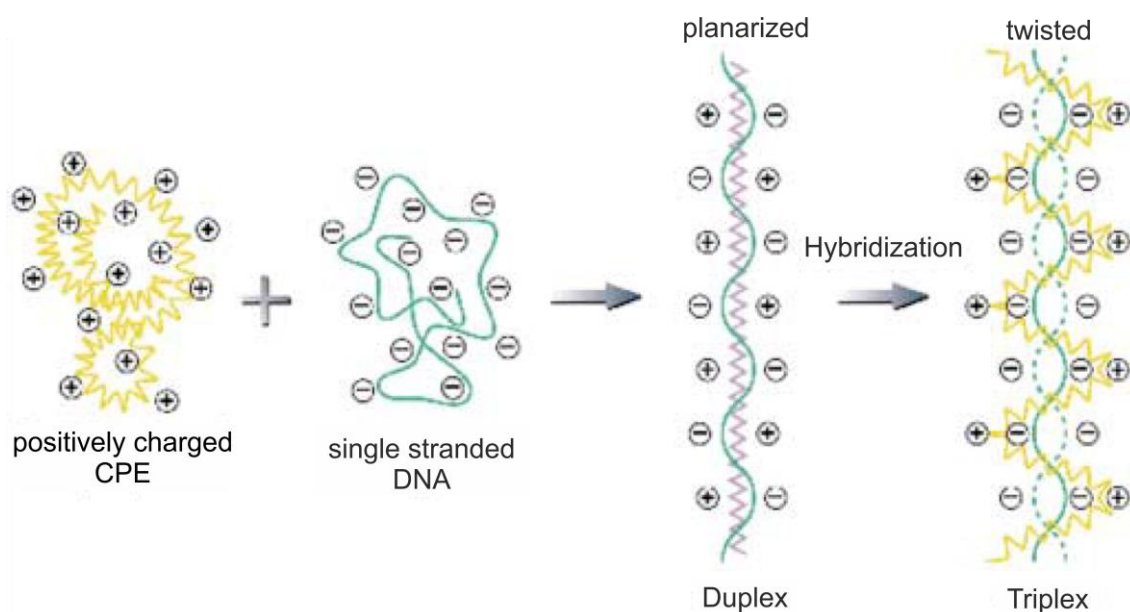


Figure 1.1. Schematic representation of interaction between conjugated polyelectrolyte and DNA probe.¹⁶

The interaction between cationic conjugated polyelectrolyte and single-stranded DNA (ssDNA)/double-stranded DNA (dsDNA) is based on the electrostatic interactions between the positive charges on the polyelectrolyte pendant group and the negative charges on the DNA strand illustrated in Figure 1.1. When the ssDNA is added to PT solution, an electrostatic interaction between the positive quaternary ammonium groups in the polymer and the negative phosphate groups in the DNA occurs, forming a planarized PT-DNA complex (duplex). The planarization in polyelectrolyte backbone enhances the overlap in the π orbitals on polymer backbone, increasing the effective conjugation length and causing changes in the optical properties.^{11,17} The longer effective conjugation length on the backbone decreases the HOMO and LUMO energy level difference, and the absorbance spectroscopy shifts towards the red region in visible spectrum. In addition, quenching occurs in fluorescence spectroscopy. In contrast to single-chain DNA, polyelectrolyte conformation is preserved in random coil geometry when dsDNA is complexed with the polyelectrolyte because of the stable helical structure of double stranded DNA. In this case, the polyelectrolyte sustains its photophysical characteristic like absorbance maximum, fluorescence emission and color. The fact that the differentiation in the optical properties of the polyelectrolyte from conformational changes can be detected by simple spectroscopic methods, even with the naked eye, promotes the use of cationic conjugated polyelectrolyte derivatives as DNA biosensors.¹⁸

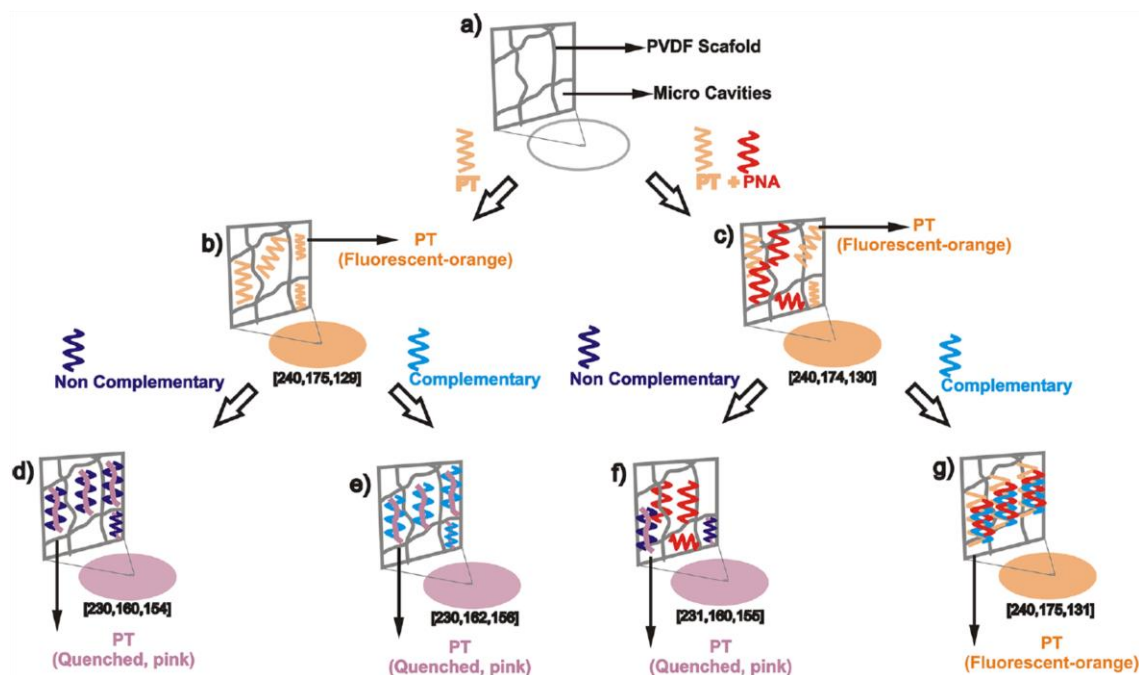


Figure 1.2. Schematic representation of conjugated polythiophene based assay for detection of miRNA.¹⁹

Numerous studies on backbone conformational changes of conjugated polyelectrolyte derivatives have been reported in the area of biosensing. The energy band alteration caused by the distinct conjugation length on polythiophene backbone allows determination of color transition even by naked eye.^{19–22} A biosensor platform of cationic polythiophene embedded PVDF has been developed by Yildiz et al. to detect miR-21 which is a micro RNA sequence associated to NSCLC.¹⁹ The assay principles shown in Figure 1.2 relies on the selectivity of PT - PNA complex to complementary and non-complementary RNA sequences. The introduction of complementary sequence results in color preservation in the biosensor platform, forming triplex complex with PT – PNA whereas non-complementary sequence causes color change from orange to pink by the reason of strong electrostatic interaction between PT and the sequence. An assay based complex formation of polythiophene was designed by Yildiz et al. for detection of enzyme activity of ATPase, discriminating ATP and ADP coordinated with polythiophene backbone.²³ Same group has also examined ATP-dependent processes related to ATP-permeable vesicles by fluorescence polythiophene reporter.²⁴

The primary sensing mechanism of polythiophene is based on the changes in backbone conformation or backbone stacking. These structural arrangement in polythiophene backbone provides sensitivity and responsiveness to analytes.²⁵ Beyond

this concept, the flexibility of tailoring fluorescence nature of polyelectrolyte by increasing conjugation length surpasses on fluorescent small molecule. As the number of monomer units in a polymer chain is increasing, the gap between highest occupied and lowest unoccupied molecular orbitals decreases which resulting in lower energy gaps. Therefore, typical lower-energy gap properties of polyelectrolyte enable them to be characterized by fluorescence spectroscopy which one of the most sensitive techniques. Fluorescence emission signals are collected against a low (*dark*) background and fluorescence intensity is directly proportional to excitation power but slightly pathlength compared to other techniques.²⁶

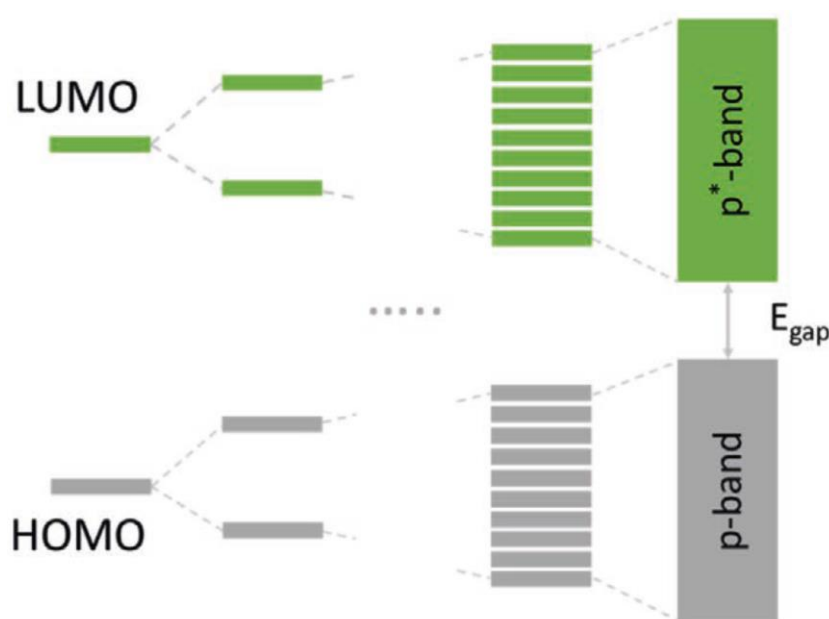


Figure 1.3. Effect of conjugation length on the orbital band gap of a polyelectrolyte.²⁷

1.3. Polymer Dots and Polymer Nanoparticles

Development of polymer nanoparticles and polymer dots (Pdots) obtained from conjugated polyelectrolytes reveals their significant advances in biological imaging, diagnosis, and drug delivery studies.²⁹⁻³⁴ Polymer nanoparticles have been widely preferred for biological applications due to their excellent fluorescence emission, colloidal stability, and biocompatibility as well as their reversible conformation changes on the polyelectrolyte backbone.^{35,36} These unique characteristics of polymer nanoparticles and Pdots enable them to be utilized in vivo and in vitro imaging studies

along with the cell penetration capability of the particles.³⁷⁻³⁹ In addition to tremendous emission features of polymer dots, tunable particle size has increased their utilization as fluorescent probe to deliver drugs and biological materials into cells. Polymer dots with a size of 2-30 nm have a greater absorption coefficient, fluorescence quantum efficiency, photostability and colloidal stability than conjugated polymer nanoparticles, which are known to be larger than 30 nm.^{38,40,41} Nanoprecipitation and miniemulsion are two well-known preparation methods for polymer nanoparticle in the literature.^{39,42,43} Modifications to commonly used techniques (for example, the use of solid support) can be utilized to make small-sized single-chain polymer dots.⁴⁴ These well-known procedures, on the other hand, have drawbacks in terms of the duration of the protocol and the chemicals needed. Surfactants, hydrophobes, and harsh solvents used in the preparation of polymer dots, pose an issue for cell viability in biological imaging. The polymer dot preparation methods in the literature are classified below.

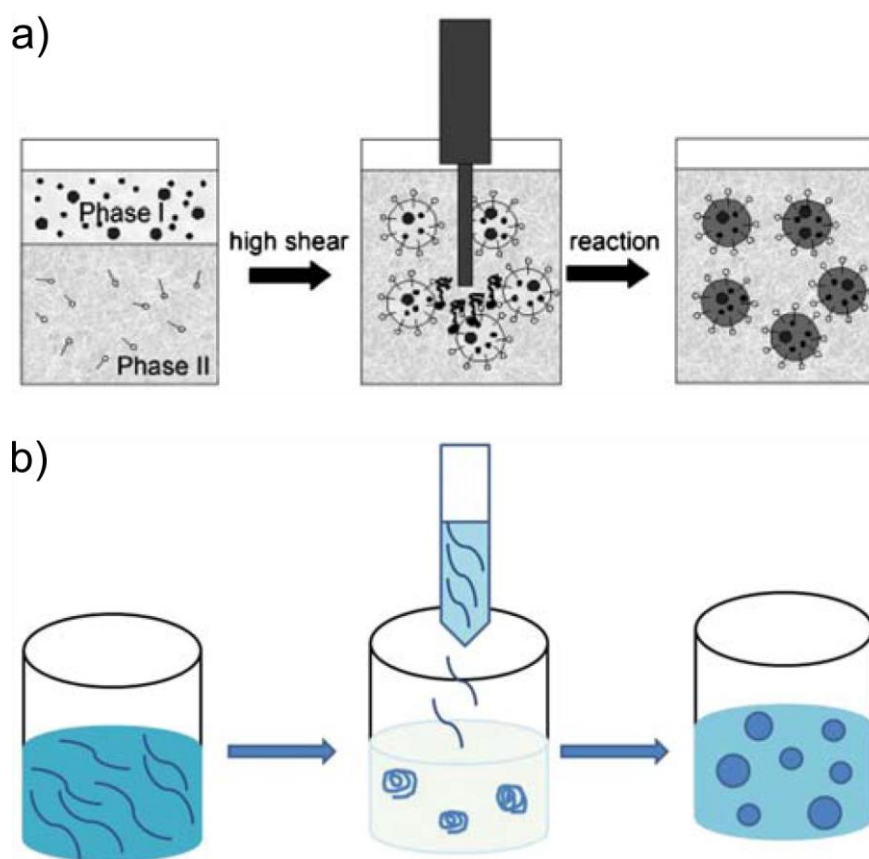


Figure 1.4. Schematic representations for preparation of conjugated polymer nanoparticle by a) miniemulsion and b) nanoprecipitation methods.

Nanoprecipitation. Conjugated polymer is dissolved in good solvent, which is mostly organic solvent, of CPE to prepare a stock solution. The stock solution is then added to water and sonicated. The organic solvent is removed by N₂ flow and the resulting Pdot solution is filtered through a microfilter.⁴⁵

Miniemulsion. Conjugated polymer is dissolved in a water-immiscible organic solvent and added to a surfactant solution to prepare a dispersion. The solution is vigorously sonicated for the preparation of miniemulsion. Final solution is stirred in a hot water bath to evaporate the organic phase and then filter through a micro membrane to yield polymer nanoparticle.⁴²

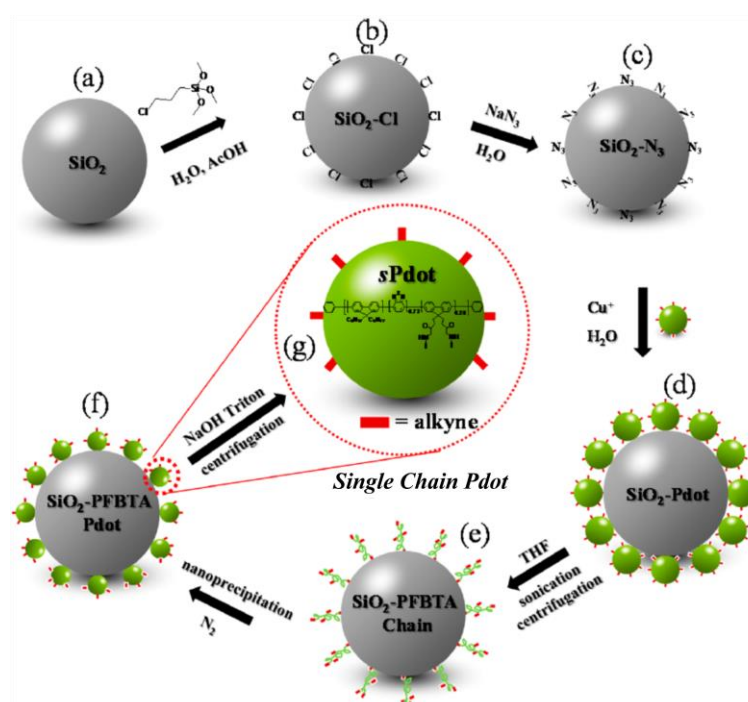


Figure 1.5. Protocol for preparation of single-chain polymer dots (sPdot).⁴⁴

Solid support for Pdot preparation. The polymer dots prepared by the reprecipitation method are added to a solution of functionalized silica particles. The polymer dots are attached through the functional groups on the silica surface via click chemistry, then precipitated by centrifugation and washed with pure water. The polymer dot-silica complex in good solvent is added to the aqueous phase and the solvent is removed under N₂ atmosphere and heat. After the solution is filtered, polymer dots are detached from silica surface with NaOH and Triton 100.⁴⁴

1.4. Characterization Methods of Conjugated Polyelectrolytes

1.4.1. Fluorescence Spectroscopy

Luminescence which describes the emission of light from any substance is investigated in two class, fluorescence, and phosphorescence, depending on the nature of the excited state.⁴⁶ The electron in excited-state orbital is paired with the electron in the ground-state orbital by oppositely spin. As a result of returning of the electron from excited state to the ground state is spin allowed, therefore, an emission of a photon occurs rapidly.

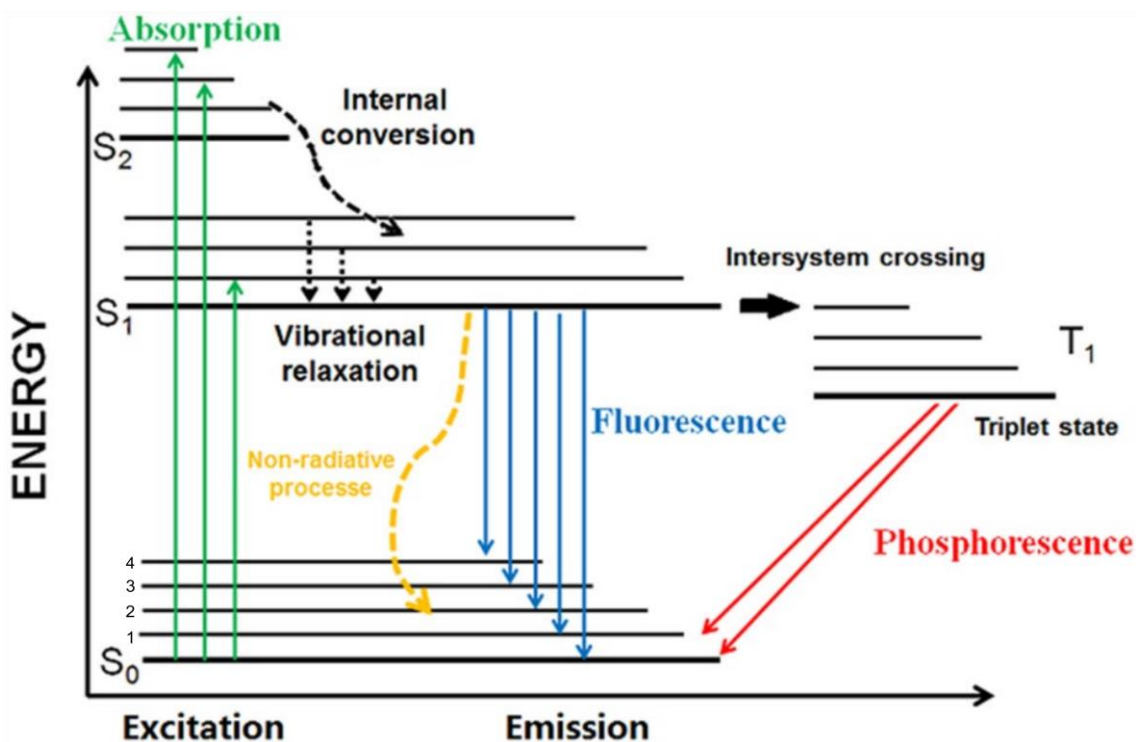


Figure 1.6. Jablonski diagram of photophysical processes.⁴⁷

A three-energy-level diagram showing the photophysical processes occurring between excited and ground state was first proposed by the Polish physicist Aleksander Jablonski in 1933. A more detailed diagram including the vibronic transition have been called *Jablonski diagram* illustrated in Figure 1.6 in which the singlet ground, first, and second electronic states are designated as S_0 , S_1 , and S_2 , respectively.⁴⁸ Horizontal lines above each electronic state are pointed vibronic states numbered as 0, 1, 2, 3, etc.

Absorption and emission processes are in general emerged from the lowest vibronic state. After absorption, which is the process known as *excitation*, a fluorophore can be excited to higher vibrational levels of S_1 or S_2 and the rapid relaxation ($\sim 10^{-12}$ s) of molecules occurs to the lowest vibronic states of S_1 , called as *internal conversion*.⁴⁶ The fluorophore molecules persist in the lowest vibrational state of the excited electronic state for a level of nanoseconds which measures the fluorescence lifetime. Hereupon, returning of the fluorophore from singlet excited state to an allowed vibronic level in the ground state is henceforth called *fluorescence emission*.⁴⁹ Transition of excited molecules in the S_1 electronic state to the first triplet state T_1 might occur which is called *intersystem crossing*. Radiative relaxation of excited molecules from the first triplet state to the ground state is the process of *phosphorescence* that has a longer lifetime in the order of microseconds and seconds compared to fluorescence. However, rate constants of phosphorescence are quite smaller than those of fluorescence since the transition from triplet to the singlet ground state is forbidden.⁴⁶

1.4.2. Light Scattering

Scattering technique, in which microwave, infrared, X-rays and neutrons are used as sources, is one of the important methods used to investigate the structural and colloidal features of materials. The most commonly used scattering techniques are static/dynamic light scattering, X-ray scattering, and neutron scattering. These three techniques are characterized primarily by the source as a scattered element and consequently by the wave vector difference. Visible light with a wavelength of several hundred nanometers, X-ray with 0.1-0.2 nanometers, and neutron with a wavelength of roughly 0.5 nanometers are utilized in light, X-ray, and neutron scattering techniques, respectively.⁵⁰ The scattering wave vector (q) can be calculated with the formula in equation 1.1. The schematic representation of the light scattering setup is demonstrated in Figure 1.7.

$$q = \frac{4\pi}{\lambda} \sin \frac{\theta}{2} \quad (1.1)$$

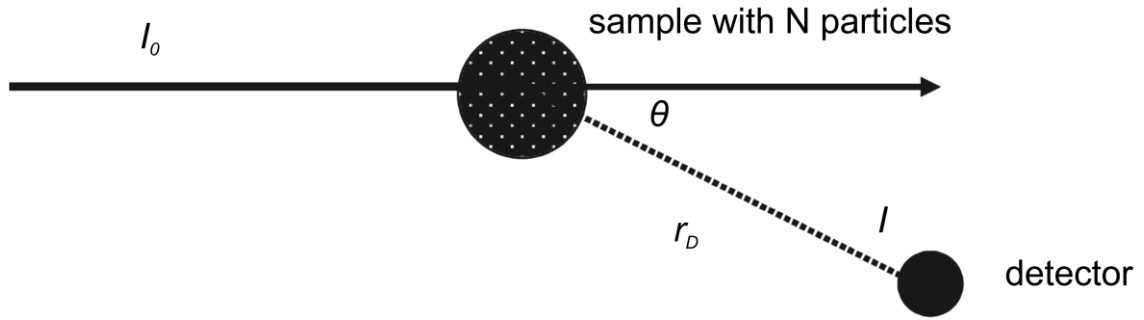


Figure 1.7. Schematic for the light scattering process, including detection of the scattered intensity (I) at scattering angle (θ).⁵¹

If the scattering particles are moving in the solution state, Brownian motion of the particles results in scattering intensity fluctuated with time. Dynamic light scattering (DLS) is a widely used technique for measuring the Brownian motion of particles and this motion, which depends on particle size, temperature, and viscosity of solvent, is then associated to diffusion coefficient of the particles. Large particles diffuse slowly in a homogenous environment, therefore, have similar positions at different time. However solvent molecules are moving very fast and cannot possess a specific position.⁵¹⁻⁵³

In DLS technique, the incident light is scattered in all directions after the laser light hits the particles in sample and intensity of the scattered light is monitored by a detector. Since the particles are still in motion, Doppler phenomenon occurs in the incident light and the scattered light produces detectable signal by generating mutually destructive and/or constructive phases.⁵³ Intensity correlation function $G_2(\tau)$ which is obtained by a digital autocorrelator set-up to correlate the intensity fluctuation in scattered light is measured for analyzing the diffusion characteristics of the particles.⁵⁴

$$G_2(\tau) = \langle I(t)I(t + \tau) \rangle \quad (1.2)$$

However, a typical light scattering cannot determine the exact movement of each particle, an electric field correlation function, $G_1(\tau)$, also known as the first-order correlation function, is utilized to correlate the relative movement of particles to each other and expressed as:

$$G_1(\tau) = \langle E(t)E(t + \tau) \rangle \quad (1.3)$$

where, $E(t)$ and $E(t+\tau)$ symbolize the scattered electric fields at times (t) and $(t + \tau)$.⁵²

Hydrodynamic radius (R_H) of particles can be determined by the Stokes-Einstein relation (equation 1.4). The equation utilizes diffusion coefficient of particles measured by light scattering experiment and viscosity of solvent as well for calculation of hydrodynamic radius of hypothetically sphere particles.^{51,52}

$$R_H = k_B T / (6\pi\eta D) \quad (1.4)$$

where R_H : hydrodynamic radius, k_B : Boltzmann constant, T : temperature, η : viscosity of solvent, and D : diffusion coefficient of particles in Stokes-Einstein equation.



Figure 1.8. Image of ALV multi angular dynamic and static light scattering set-up.

Angular dependent light scattering (The instrumentation is illustrated in Figure 1.8) provides important structural information about the conformation and interaction parameter of the polymer chain. Besides, X-ray and neutron scattering ensures detailed structure analysis due to higher wave vector. The form factor $P(q)$, as a function of scattering angle defines the light scattering from particle which then utilize to determine its size and shape. After a series of expansion and mathematical calculations, particle form factor can be expressed by equation (1.5):⁵¹⁻⁵⁵

$$P(q) = 1 - \frac{1}{3} s^2 q^2 + \dots \quad (1.5)$$

$$\frac{K_c}{R} = \frac{1}{MP(q)} + 2A_2c + \dots \quad (1.6)$$

$$\frac{Kc}{R} = \frac{1}{M} + 2A_2c \quad (1.7)$$

When the form factor is placed in normalized absolute scattering intensity (Equation 2), the Zimm equation can be derived. The Zimm equation provides very significant parameter like molar mass, second virial coefficient and most importantly radius of gyration (R_g) directly related to size and shape of a particle. Some ρ -ratios are given in Table 1 for the most typical particle morphology.

$$\text{Slope} = \frac{R_g^2}{3M} \quad (1.8)$$

$$\rho = \frac{R_g}{R_H} \quad (1.9)$$

Table 1.1. ρ -ratio for common morphologies.⁵¹

Topology	ρ-ratio
Homogenous sphere	0.775
Hollow sphere	1
Ellipsoid	0.775 - 4
Random polymer coil	1.505
Cylinder of length l , diameter D	$\frac{1}{\sqrt{3}} \ln \left(\frac{l}{D} - 0.5 \right)$

1.4.3. Fluorescence Microscopy

A fluorescence microscope is an optical microscope which uses appropriate fluorophores as filters to illustrate any synthetic or natural fluorescent materials. The technique exploits a black background, analogue to the night for observing only targeted object by fluorescence emission. By the developments achieved on setup of the microscope to increase the contrast between a sample (signal) and everything else (background), fluorescence imaging has become the backbone of microscopy in biology because of inherent selectivity of fluorescence emission. Organic chemists, thereafter, have developed thousands of fluorescent probes, allowing them to label almost any component of biological systems.⁵⁶⁻⁵⁸

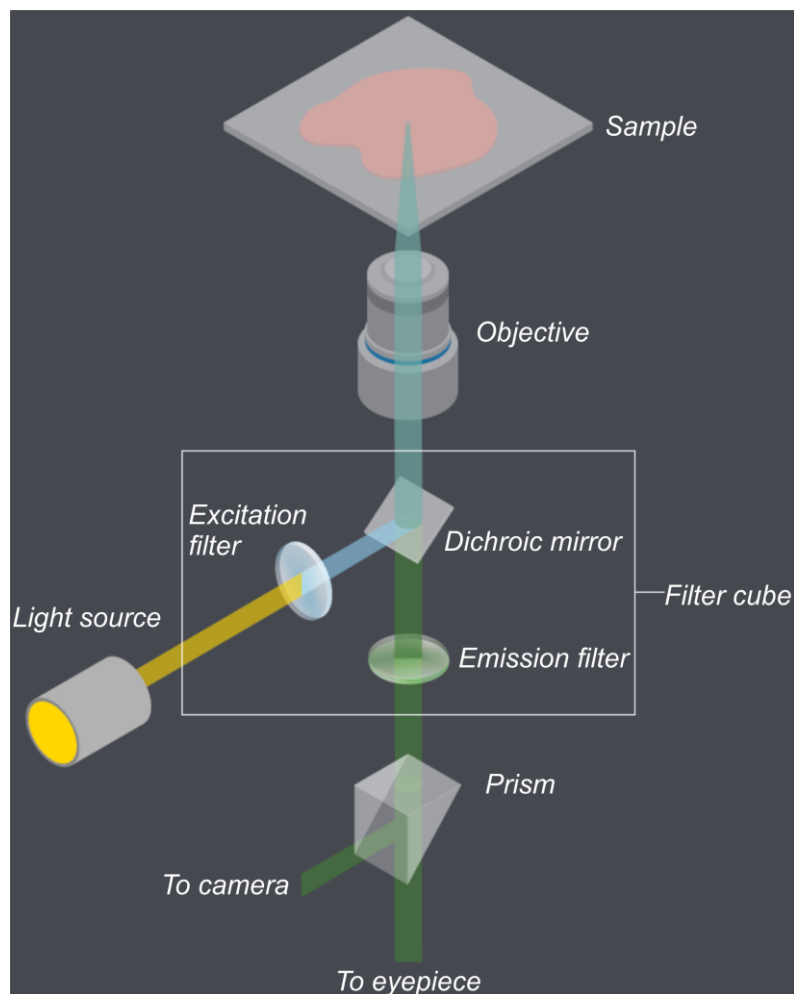


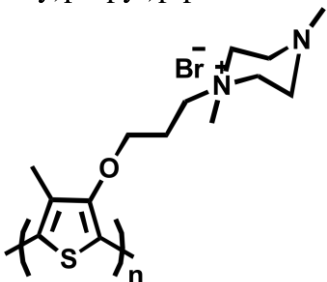
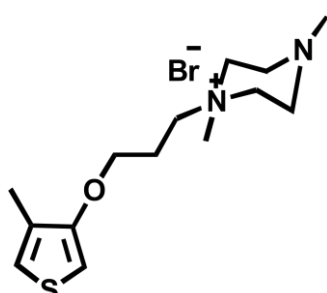
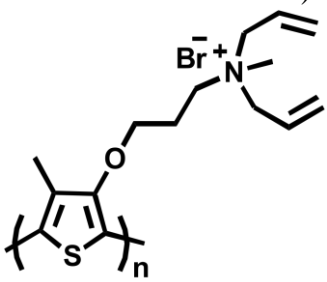
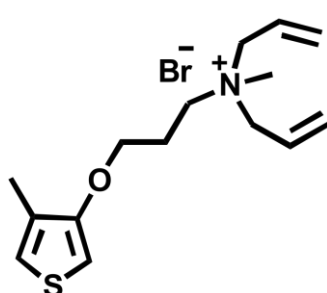
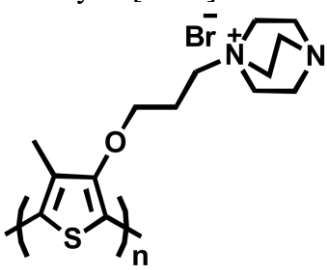
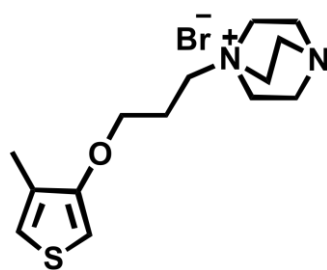
Figure 1.9. Basic setup of an inverted widefield fluorescence microscope.⁵⁹

The basic instrumentation of fluorescence microscope is illustrated in Figure 1.9. Filter cube is the key component responsible for both excitation of sample and collection of the emission from sample. A narrow wavelength which is close to the absorption wavelength of the sample is permitted to pass through the excitation filter while any other wavelengths are partially or totally blocked by the excitation filter. A dichroic mirror was designed for reflecting the light below a specific wavelength (a cutoff wavelength) and allowing the other wavelengths to pass through. The wavelength which corresponds to 50% transmission of is called as cutoff wavelength directly related to the mirror. Besides reflecting the excitation wavelength, the dichroic mirror plays an important role to transmit the emission light from the sample to the sensing system by placing one the mirror into the instrumentation at 45° with respect to the incident light. As a final element of filter cube, emission filters are specifically designed to transmit the target emission at wavelength with a narrow band while blocking the remaining wavelengths.^{59,60}

CHAPTER 2

SYNTHESIS AND CHARACTERIZATION OF CATIONIC POLYELECTROLYTES

Table 2.1. Chemical structures molecular weights of monomers and polymers.

Polymers	Monomers	Monomer based MW
PT1 - Poly(1,4-dimethyl-1-(3-((4-methylthiophen-3-yl)oxy)propyl)piperazin-1-ium bromide) 	M1 	269.25 g/mol
PT2 - Poly(N-allyl-N-methyl-N-(3-((4-methylthiophen-3-yl)oxy)propyl)prop-2-en-1-aminium bromide) 	M2 	266.23 g/mol
PT3 - Poly(1-(3-((4-methylthiophen-3-yl)oxy)propyl)-1,4-diazabicyclo[2.2.2]octan-1-ium) 	M3 	267.23 g/mol

Throughout the thesis, understanding of polyelectrolyte chain conformations in different environments (water, ethylene glycol, DMSO, and 1,4-butanediol) and characterization of polymer dots (Pdots) of three poly(3-alkylthiophene) derivatives shown in Table 2.1 have been the major two bullets for research interest. Moreover, implementation of these unique materials into nucleic acid sensing and cell imaging is the further curiosity covering the thesis.

2.1. Synthesis of Poly(1,4-dimethyl-1-(3-((4-methylthiophen-3-yl)oxy)propyl)piperazin-1-ium bromide) – PT1

2.1.1. Synthesis of 3-Methoxy-4-methylthiophene

25% of sodium methoxide (0.479 g, 8.85 mmol) which is freshly synthesized, in methanol (1.8 mL) and 1-methyl-2-pyrrolidinone (NMP) (1.0 mL) were mixed in a reaction flask. 0.5 g of 3-bromo-4-methylthiophene (2.82 mmol) and 0.25 g of CuBr (1.74 mmol) were respectively added to the reaction mixture. The mixture was reflux for 3 days at 110°C.

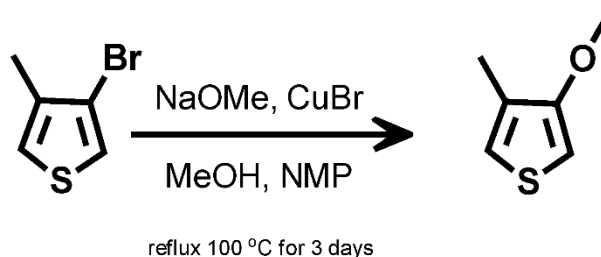


Figure 2.1. Synthesis of 3-methoxy-4-methylthiophene (precursor 1 (PC1)).

The mixture was cooled down to room temperature after reaction is completed. 1.0 M sodium bromide solution was then added to the reaction mixture and stirred for an hour at room temperature. The mixture was filtered and the precipitate was extracted with ~10 mL diethyl ether 5 times. The organic phase was washed with deionized water and then dried over MgSO₄. Remnant solvent was removed by rotary evaporator and purification was accomplished by column chromatography to obtain a light-yellow oil, 3-methoxy-4-methylthiophene (PC1 (~90%)). ¹H NMR (400 MHz, CDCl₃) δ (ppm): 6.82 (1H, d), 6.16 (1H, d), 3.82 (3H, s), 2.10 (3H, s).

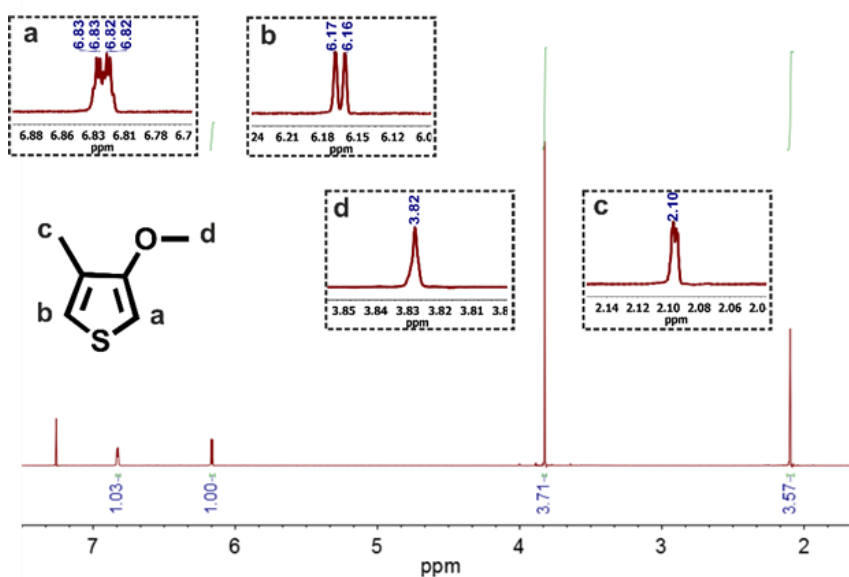


Figure 2.2. ^1H NMR spectrum of Precursor 1.

2.1.2. Synthesis of 3(3-Bromo)propoxy-4-methylthiophene

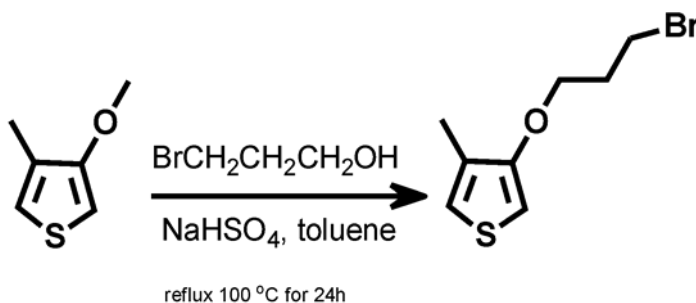


Figure 2.3. Synthesis of 3(3-bromo)propoxy-4-methylthiophene (precursor 2 (PC2)).

0.78 mmol of 3-methoxy-4-methylthiophene (PC1), 1.66 mmol of 3-bromo-1-propanol, 0.1 mmol of NaHSO_4 and 2 mL toluene were mixed in a round bottom flask. The reaction mixture was heated at 100°C and reflux for 1 day under nitrogen atmosphere. The mixture was then cooled down the room temperature and toluene was evaporated by rotary evaporator. The remaining phase was extracted with diethyl ether several times and washed with deionized water. The remnant was dried over MgSO_4 and diethyl ether was removed by rotary evaporator. For the purification of the product was performed by column chromatography method to obtain precursor 2, 3(3-bromo)propoxy-4-

methylthiophene (PC2 (~85%)) as a colorless oil. ^1H NMR (400 MHz, CDCl_3) δ (ppm): 6.84 (1H, d), 6.18 (1H, d), 4.09 (2H, t), 3.61 (2H, t), 2.34 (2H, p), 2.09 (3H, s).

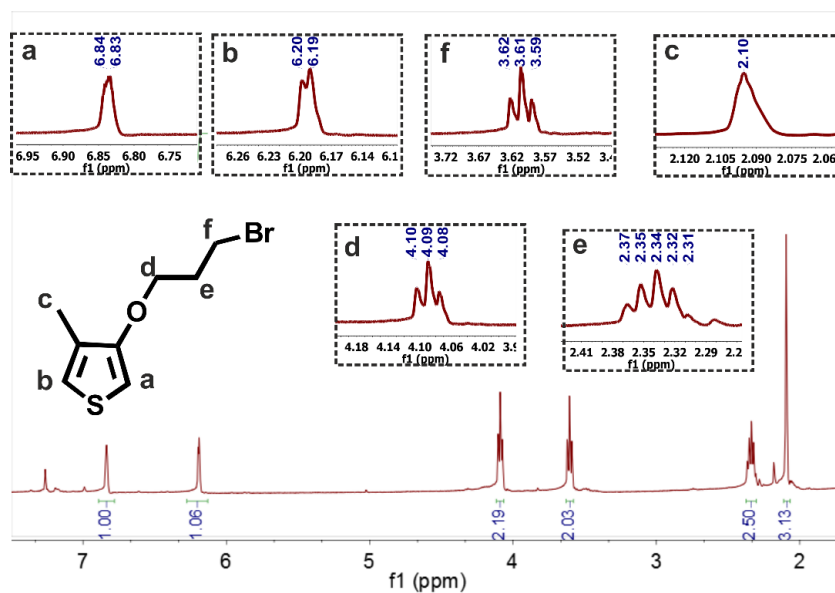


Figure 2.4. ^1H NMR spectrum of Precursor 2.

2.1.3. Synthesis of 1,4-Dimethyl-1-(3-((4-methylthiophen-3-yl)oxy)propyl)piperazin-1-ium bromide

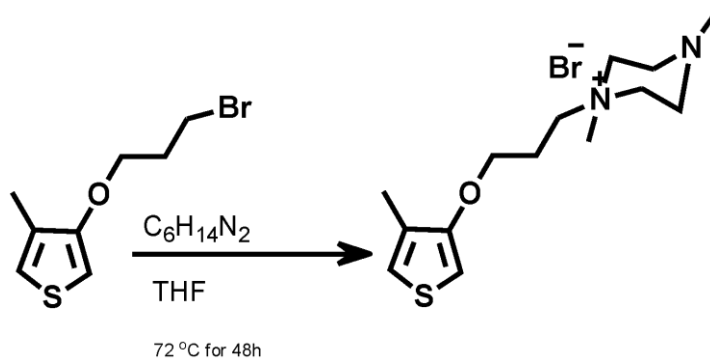


Figure 2.5. Synthesis of monomer 1 (M1) 1,4-dimethyl-1-(3-((4-methylthiophen-3-yl)oxy)propyl)piperazin-1-ium bromide.

To a round bottom flask 3(3-bromo)propoxy-4-methylthiophene (60 mg, 0.26 mmol), 1,4-dimethylpiperazine (690 μL , 5.0 mmol) and 2.5 mL THF were added. The mixture stirred at 72°C for 48 h. After cooled down to room temperature the reaction medium poured into falcon and centrifuged at 3000 rpm for 5 minutes. The supernatant was removed and washed again with THF, then centrifuged at 3000 rpm for 10 minutes.

2.1.4. Synthesis of Poly(1,4-dimethyl-1-(3-((4-methylthiophen-3-yl)oxy)propyl)piperazin-1-ium bromide)

0.08 mmol of (1,4-dimethyl-1-(3-((4-methylthiophen-3-yl)oxy)propyl)piperazin-1-ium bromide) (M1) was dissolved in 1.5 ml CHCl_3 and 0.38 mmol of FeCl_3 was dissolved in 2.3 ml CHCl_3 . FeCl_3 solution added to M1 solution dropwise. The reaction was then stirred for 1 day at room temperature under nitrogen (N_2) atmosphere. After polymerization was accomplished, the dark green precipitates were washed with the CHCl_3 and centrifuged at 4000 rpm for 5 minutes.

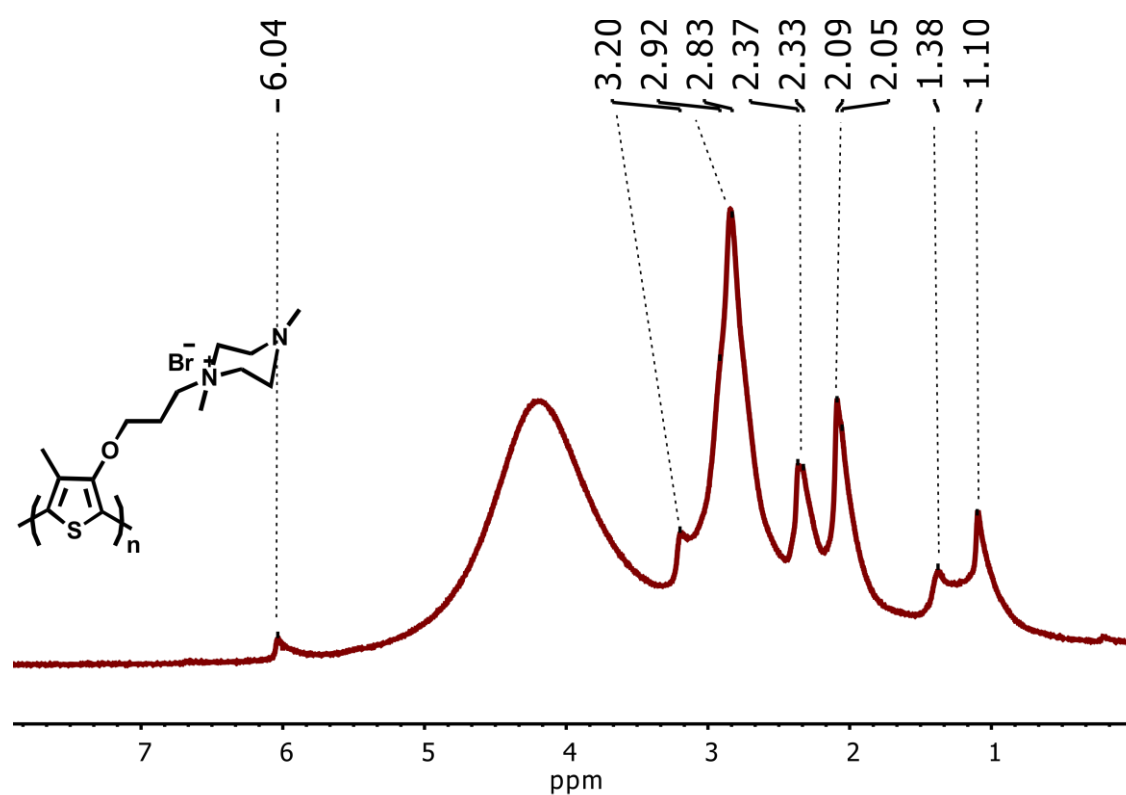


Figure 2.8. ^1H NMR spectrum of poly(1,4-dimethyl-1-(3-((4-methylthiophen-3-yl)oxy)propyl)piperazin-1-ium bromide) (PT1).

2.2. Synthesis of Poly(N-allyl-N-methyl-N-(3-((4-methylthiophen-3-yl)oxy)propyl)prop-2-en-1-aminium bromide)

2.2.1. Synthesis of N-allyl-N-methyl-N-(3-((4-methylthiophen-3-yl)oxy)propyl)prop-2-en-1-aminium bromide

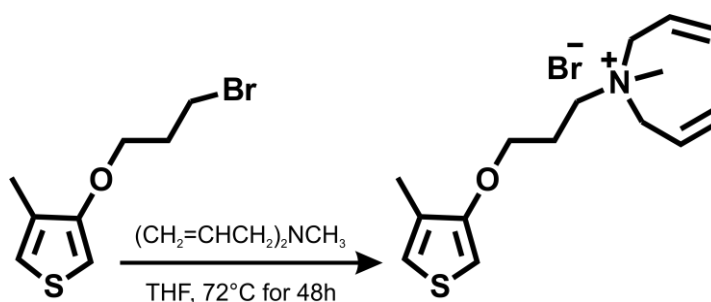


Figure 2.9. Synthesis of monomer 2 (M2) N-allyl-N-methyl-N-(3-((4-methylthiophen-3-yl)oxy)propyl)prop-2-en-1-aminium bromide.

0.26 mmol of precursor 2 (PC2), 5.0 mmol of diallylmethylamine and 2.5 mL THF were added into a round bottom flask and stirred at 72°C for 48 h. The reaction mixture was cooled down to room temperature then transferred to a 15 mL centrifuge tube. The mixture was then centrifuged at 3000 rpm for 5 minutes and this step repeated for several times and final precipitate (M2, ~67%) dried under vacuum. ¹H NMR (400 MHz, D₂O) δ (ppm): 6.90 (1H, d), 6.36 (1H, d), 5.89 (2H, ddt), 5.57 (4H, dt), 4.02 (2H, t), 3.80 (4H, m), 3.30 (2H, t), 2.89 (3H, s), 2.17 (2H, p), 1.95 (3H, s). Figure 2.11 shows the mass spectrum of N-allyl-N-methyl-N-(3-((4-methylthiophen-3-yl)oxy)propyl)prop-2-en-1-aminium bromide (M2) and base peak was found to be at 266.25 (m/z) which is correlates with the calculated molar mass of monomer 2.

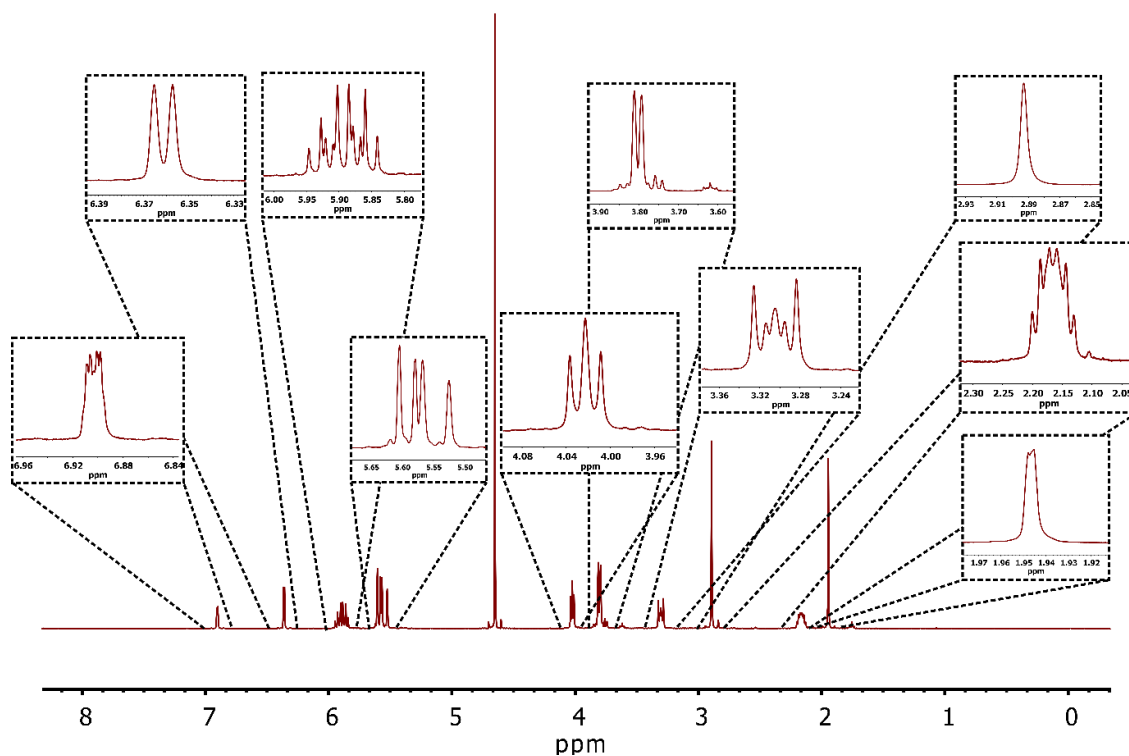


Figure 2.10. ^1H NMR spectrum of N-allyl-N-methyl-N-(3-((4-methylthiophen-3-yl)oxy)propyl)prop-2-en-1-aminium bromide.

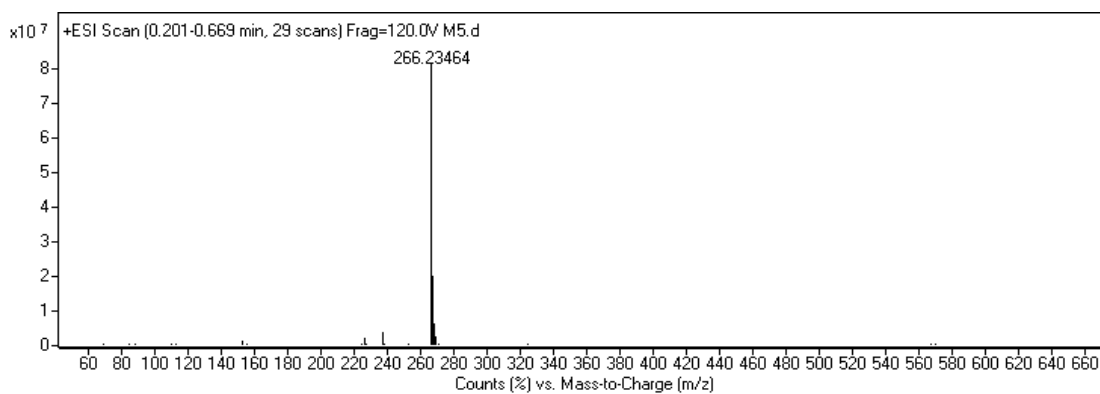


Figure 2.11. Mass spectrum of N-allyl-N-methyl-N-(3-((4-methylthiophen-3-yl)oxy)propyl)prop-2-en-1-aminium bromide.

2.2.2. Synthesis of Poly(N-allyl-N-methyl-N-(3-((4-methylthiophen-3-yl)oxy)propyl)prop-2-en-1-aminium bromide)

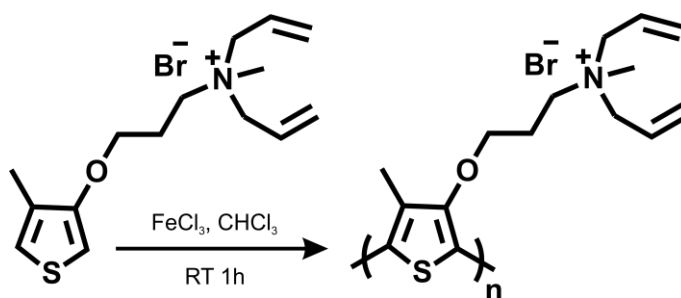


Figure 2.12. Synthesis of polyelectrolyte (PT2) Poly(N-allyl-N-methyl-N-(3-((4-methylthiophen-3-yl)oxy)propyl)prop-2-en-1-aminium bromide).

0.38 mmol of FeCl_3 was dissolved in 2.3 mL CHCl_3 then added dropwise to 0.11 mmol of monomer solution dissolved in 1.5 mL CHCl_3 . The mixture was stirred for 1 day at room temperature under N_2 atmosphere. The reaction mixture was washed with CHCl_3 and centrifuged at 4000 rpm for 5 minutes. The dark green precipitate was dried under vacuum. The NMR characterization for the polymer has been performed 400 MHz in D_2O (2 mg/mL). The typical NMR spectrum of the polymer yields broadened peaks at around 5.70, 5.40, 3.67, 2.75 and 1.94 ppm.

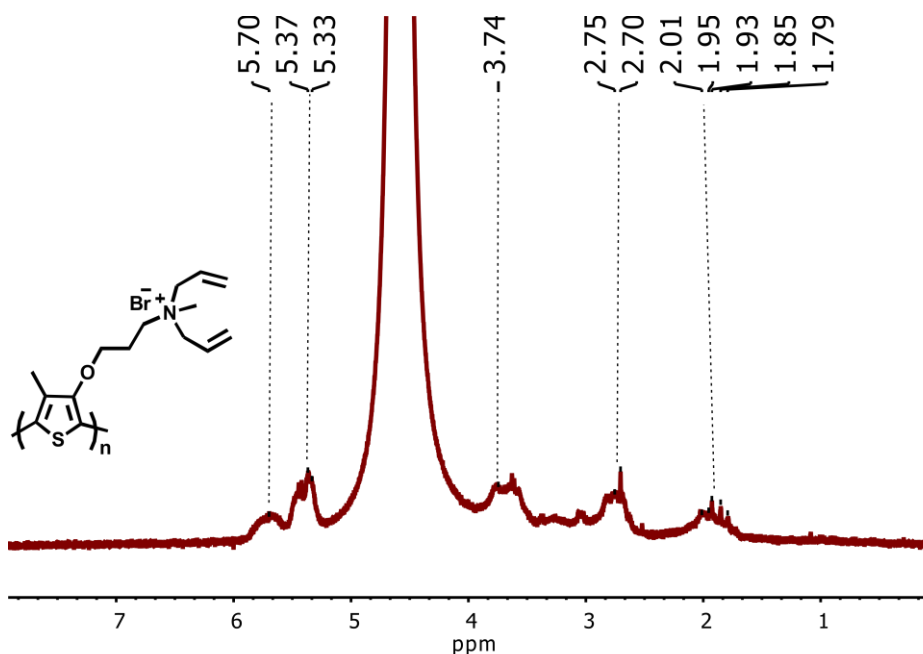


Figure 2.13. ^1H NMR spectrum of poly(N-allyl-N-methyl-N-(3-((4-methylthiophen-3-yl)oxy)propyl)prop-2-en-1-aminium bromide).

2.3. Synthesis of Poly(1-(3-((4-methylthiophen-3-yl)oxy)propyl)-1,4-diazabicyclo[2.2.2]octan-1-ium)

2.3.1. Synthesis of 1-(3-((4-methylthiophen-3-yl)oxy)propyl)-1,4-diazabicyclo[2.2.2]octan-1-ium

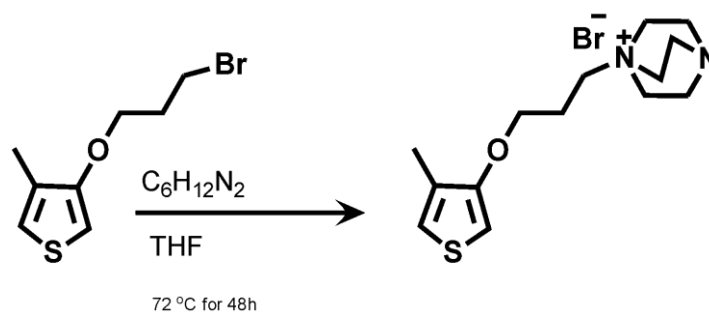


Figure 2.14. Synthesis of monomer 3 (M3) 1-(3-((4-methylthiophen-3-yl)oxy)propyl)-1,4-diazabicyclo[2.2.2]octan-1-ium.

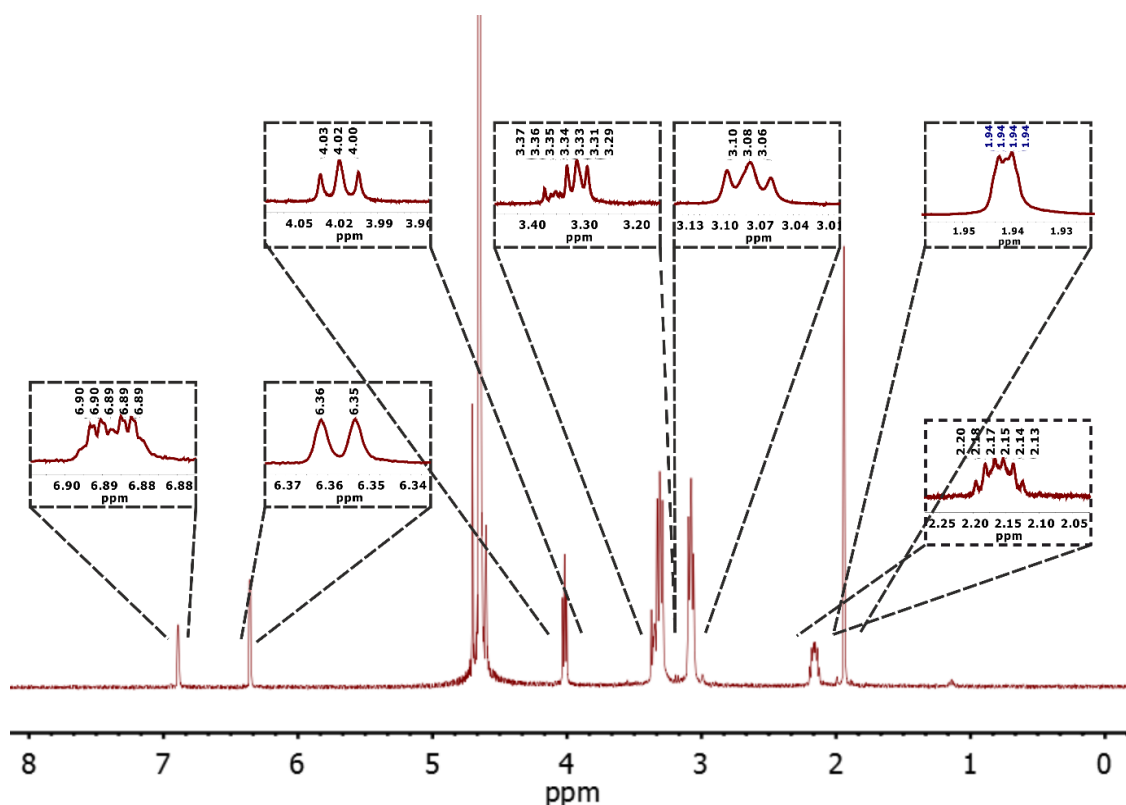


Figure 2.15. ^1H NMR spectrum of 1-(3-((4-methylthiophen-3-yl)oxy)propyl)-1,4-diazabicyclo[2.2.2]octan-1-ium.

To a round bottom flask 0.26 mmol of 3(3-bromo)propoxy-4-methylthiophene, 5.0 mmol of 1,4-diazabicyclo[2.2.2]octane and 2.5 ml THF were added. The mixture was stirred at 72°C for 48 h. After the reaction was cooled down to room temperature, the reaction medium poured into falcon and centrifuged at 3000 rpm for 5 minutes. The supernatant was removed and washed again with THF, then centrifuged at 3000 rpm for 10 minutes. The supernatant was removed again, white color precipitate (M3 (70%)) observed and dried under vacuum. ¹H NMR (400 MHz, D₂O) δ (ppm): 6.89 (1H, d), 6.33 (1H, d), 4.02 (2H, t), 3.34 (3H, t), 3.08 (3H, s), 2.69 (4H, t), 2.21 (3H, s), 2.15 (2H, p), 1.92 (3H, s). Figure 2.16 represents the mass spectrum of 1-(3-((4-methylthiophen-3-yl)oxy)propyl)-1,4-diazabicyclo[2.2.2]octan-1-ium (M3) and base peak was found to be at 267.23 (m/z) that matches with the calculated value of molar mass of M3.

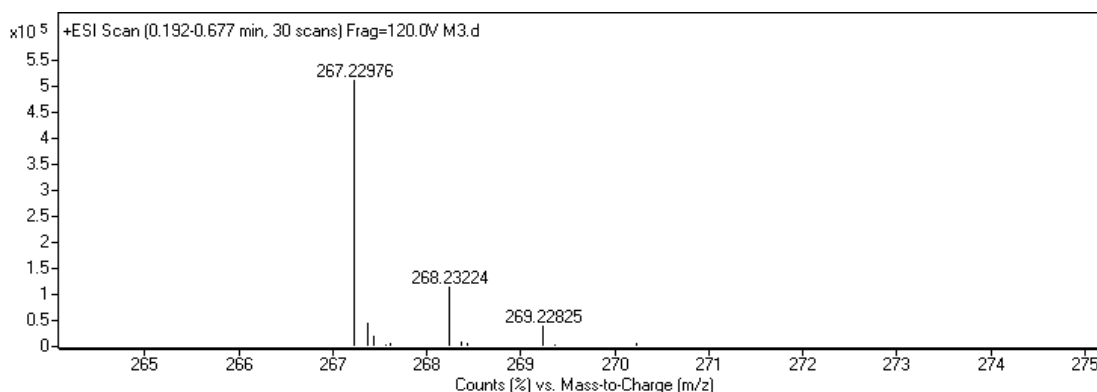


Figure 2.16. Mass spectrum of 1-(3-((4-methylthiophen-3-yl)oxy)propyl)-1,4-diazabicyclo[2.2.2]octan-1-ium.

2.3.2. Synthesis of Poly(1-(3-((4-methylthiophen-3-yl)oxy)propyl)-1,4-diazabicyclo[2.2.2]octan-1-ium)

FeCl₃ (60 mg, 0.38 mmol) was dissolved in 2.3 mL CHCl₃ then added dropwise to the monomer (30 mg, 0.11 mmol) solution dissolved in 1.5 mL CHCl₃. The mixture was stirred at room temperature for 1 day under N₂ atmosphere. The reaction mixture was washed with CHCl₃ and centrifuged at 4000 rpm for 5 minutes. The dark green precipitate was dried under vacuum. The NMR characterization for the polymer has been performed 400 MHz in D₂O (2 mg/mL). The typical NMR spectrum of the polymer yields broadened peaks at around 3.47, 3.36, 3.23, and 1.68 ppm (shown in Figure 2.17 with dashed lines).

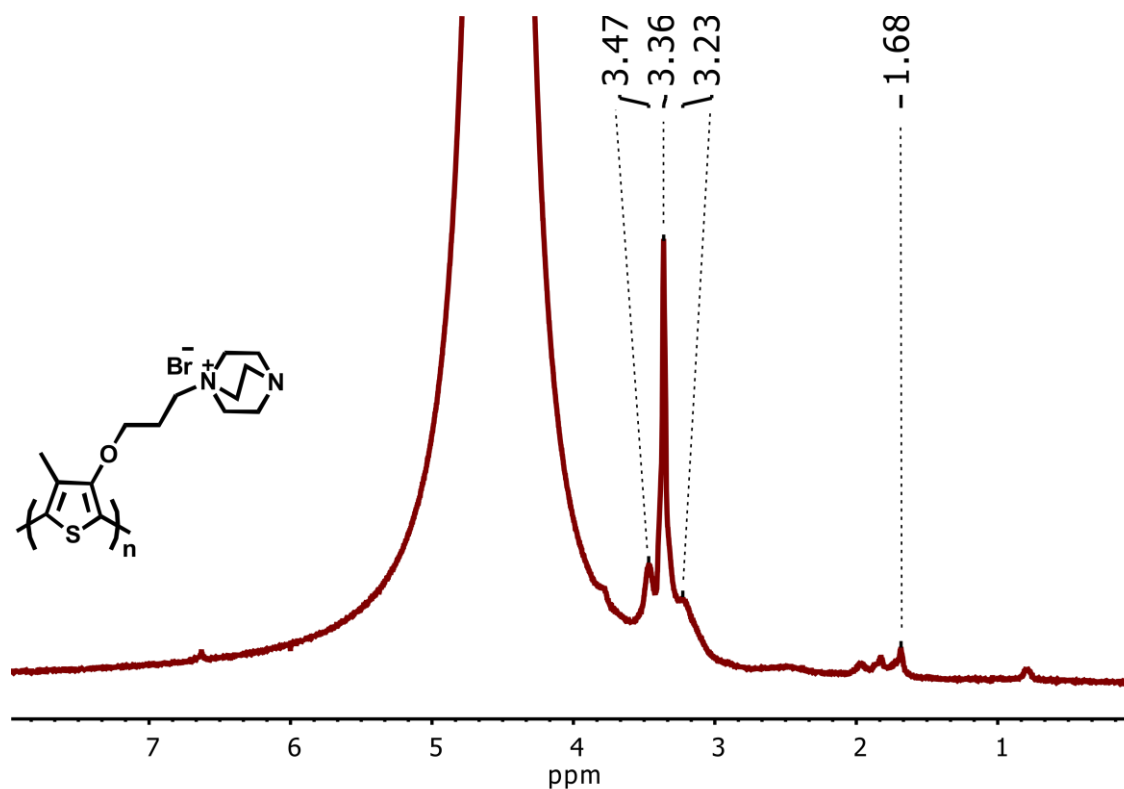


Figure 2.17. ^1H NMR spectrum of poly(1-(3-((4-methylthiophen-3-yl)oxy)propyl)-1,4-diazabicyclo[2.2.2]octan-1-ium) (PT3).

2.4. Characterization of Cationic Polyelectrolytes

The synthesized cationic polyelectrolytes were dissolved in distilled water to characterize optical properties of polyelectrolytes. Figure 2.18 demonstrates normalized absorbance and state-state fluorescence spectra of polyelectrolytes (PT1-PT2-PT3). The absorbance of PTs was found to be around 400 nm with an approximately similar conjugation length. The slight shifts which are less than 5 nm, on absorption maxima of polyelectrolytes can be attributed to the polarity of each monomer structure. The fluorescence spectra of the polyelectrolyte shown in Figure 2.18b was recorded with a 400 nm excitation wavelength. Fluorescence emission at around 530 nm was observed for the polyelectrolytes dissolved in water.

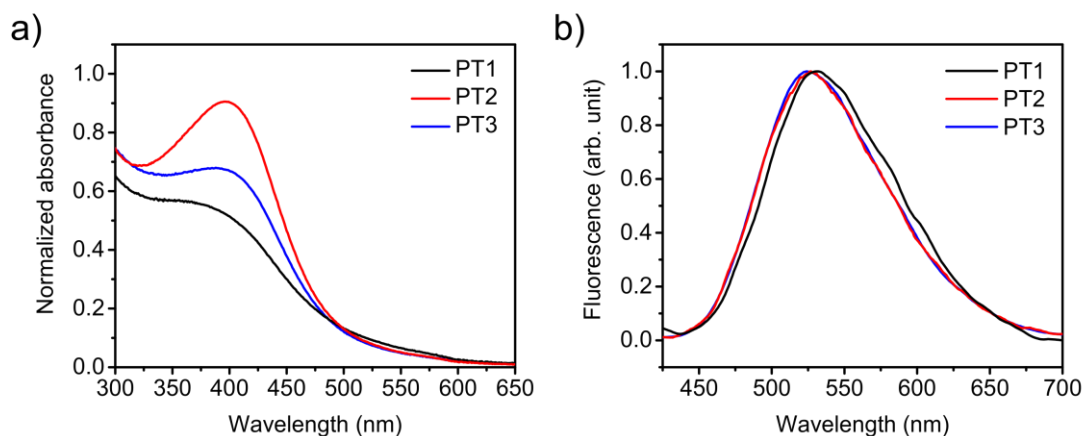


Figure 2.18. a) Absorption and b) fluorescence spectra of polythiophene (PT) derivatives dissolved in water.

In polyelectrolyte theory, solvation is the primary parameter effecting the interaction of polyelectrolytes which is directly related to chain conformation of polyelectrolyte in solution state. To understand the spectral features of cationic conjugated polyelectrolyte in several solvents was investigated in absorption and fluorescence spectroscopy. Twelve solvents with a relative polarity ranging from 0.2 to 1.0 were utilized to dissolve the polyelectrolyte for initial photophysical characterization. The absorbance spectra of cationic polythiophene derivative dissolved in the twelve solvents is represented in Figure 2.19. Low-polarity solvents show light absorption at around 360 nm whereas the solvents causing bathochromic shift in absorbance spectra, at the 400 nm and above absorption maxima, are highly polar solvents except for DMSO. The $\pi\text{-}\pi^*$ transition occurs at around 360 nm in low polarity solvents, however methanol which is contrarily a high-polarity solvent causes hypsochromic shift to 360 nm and surprisingly, DMSO, low-polarity solvent, expresses two absorption peaks at 340 and 470 nm. On the other hand, water, TE buffer, glycerol and ethylene glycol as expected have absorption peaks at 400, 435, 420, and 370 nm with a shoulder at 415 nm, respectively.

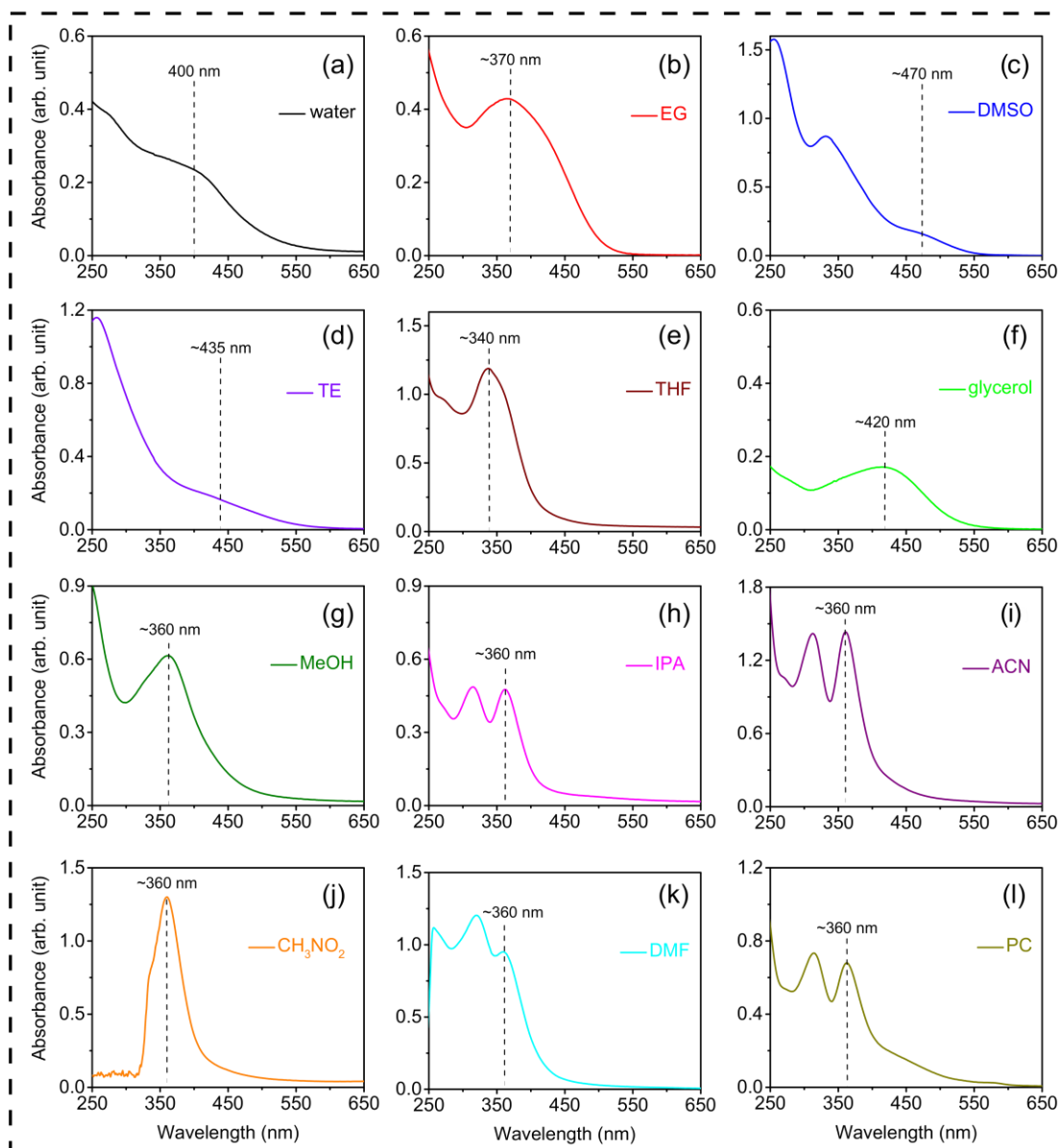


Figure 2.19. Absorption spectra of cationic polyelectrolyte derivative (PT3) dissolved in a) water, b) ethylene glycol, c) DMSO, d) Tris-EDTA buffer, e) THF, f) glycerol, g) methanol, h) 2-propanol, i) acetonitrile, j) nitromethane, k) DMF, and l) propylene carbonate.

To understand the emissive characteristic of polyelectrolyte in these solvent, steady-state fluorescence spectroscopy was conducted demonstrated in Figure 2.20. In the solvents causing bathochromic shift in absorption spectra below 400 nm, no radiative emission was observed with the exception of THF which has fluorescence emission at 460 nm with a high intensity. Cationic polyelectrolyte dissolved in water and TE buffer have fluorescence emission at 535 nm with a relatively low intensity. As further examples of polar solvents, ethylene glycol and glycerol were utilized to dissolve the

polyelectrolyte for spectroscopic characterization. It was also observed that solubility of cationic polythiophene was quite fast in ethylene glycol compared to other eleven solvents. In glycerol, PT also has fluorescence emission at 535 nm with a decreased emission intensity compared to ethylene glycol. Seven out of twelve solvents have fluorescence emission maxima from 460 nm to 565 nm.

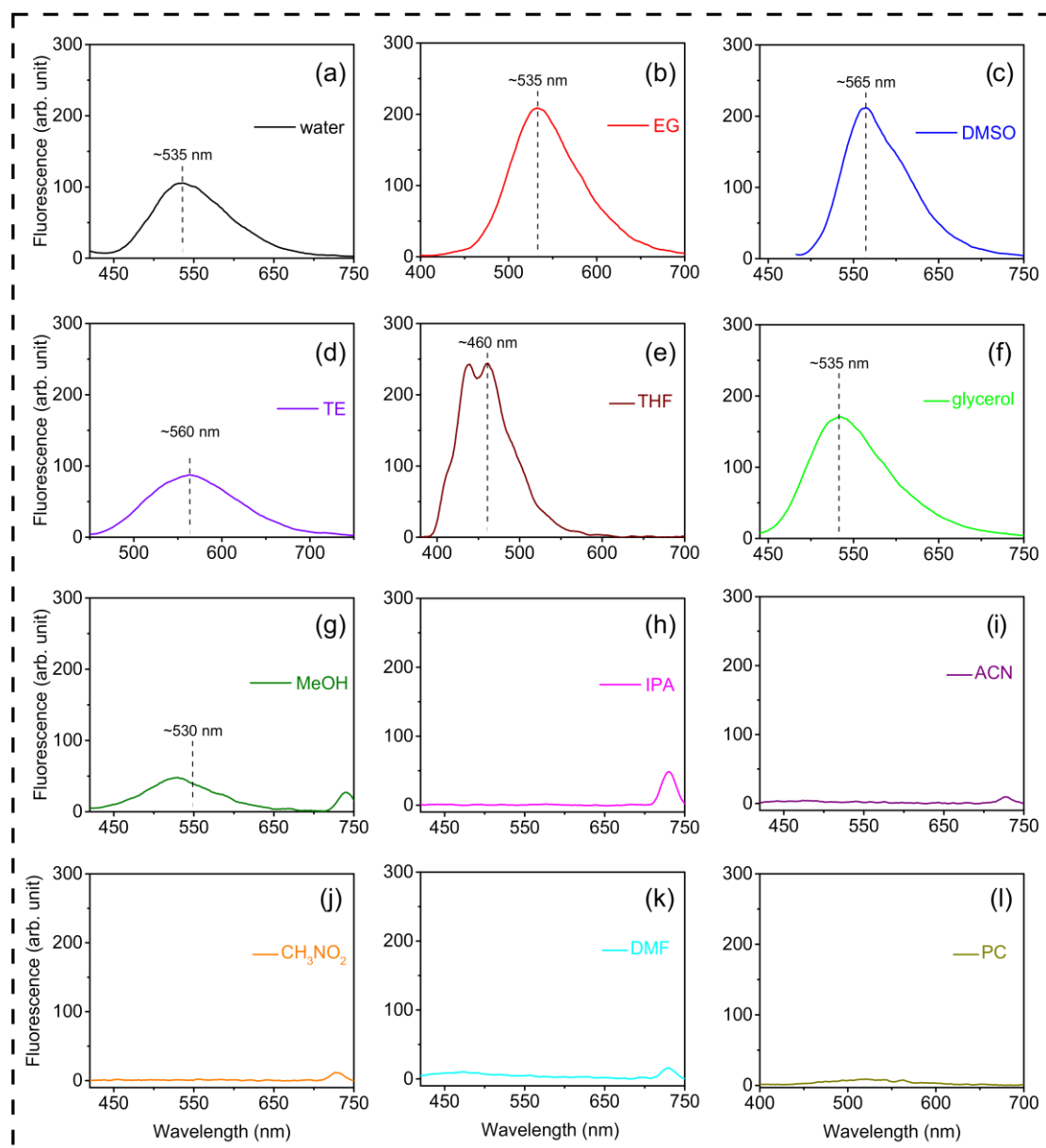


Figure 2.20. Steady-state fluorescence spectra of cationic polyelectrolyte derivative (PT3) dissolved in a) water, b) ethylene glycol, c) DMSO, d) Tris-EDTA buffer, e) THF, f) glycerol, g) methanol, h) 2-propanol, i) acetonitrile, j) nitromethane, k) DMF, and l) propylene carbonate (each solution was excited at corresponding absorption wavelengths).

Table 2.2. Fluorescence quantum yield of cationic polyelectrolyte (PT3) dissolved in selected solvents from Figure 2.19 and 20.

	excitation λ (nm)	emission λ (nm)	quantum yield (%)
Water	400	535	2.63
EG	415	535	11.2
DMSO	470	565	16.9
TE buffer	435	560	1.59
THF	340	460	-
Glycerol	420	535	3.71
MeOH	360	530	0.58

After steady-state fluorescence analysis of solvation characteristic of polyelectrolyte, fluorescence quantum yield was further analyzed for the seven solvents which does not have quenching effect of conjugated polythiophene backbone. The quantum yield values shown in Table 2.2, for polyelectrolyte solutions of water, TE buffer which is also an aqueous solution, glycerol, and methanol are found to be less than 4.0 while those of ethylene glycol and DMSO were obtained as 11.2 and 16.9, respectively.

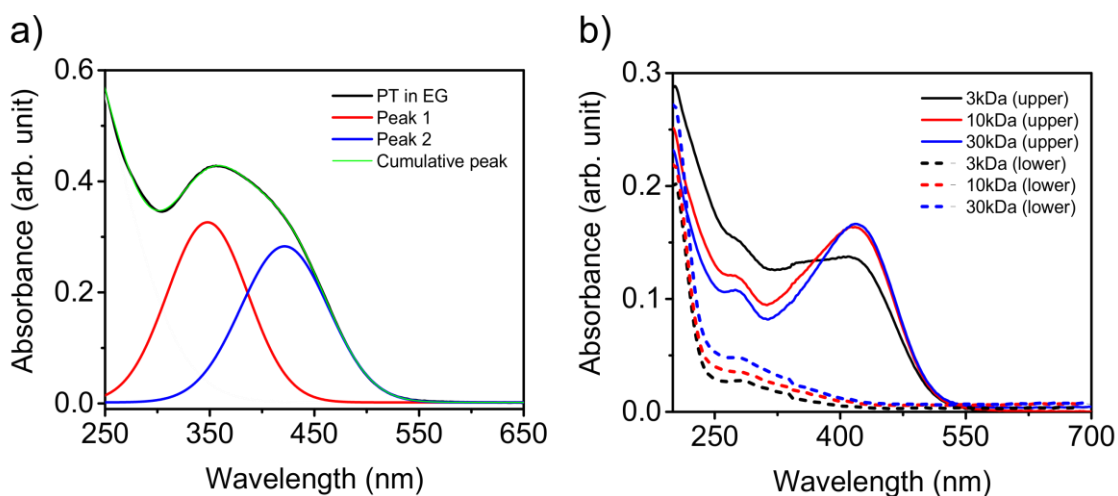


Figure 2.21. Absorbance spectra of PT3 dissolved in EG a) before and b) after filtration.

In Figure 2.21a deconvolution applied on fluorescence spectrum of polyelectrolyte dissolved in ethylene glycol. The two main peaks concealed in black and green spectrum were calculated as 350 and 420 nm by Origin software. These two wavelengths are referring two π - π^* transition associated with short and long conjugation length. To prove this statement, ethylene glycol solution of polyelectrolyte was filtered

through 3, 10, and 30kDa pore-sized centrifugal filter, upper and lower parts of the centrifugation products from each pore size were then analyzed by absorption spectroscopy. The similar multimodal spectrum was observed in upper solution collected from the 3kDa filter. However, the 10 and 30kDa allow short chains to pass through and a single absorption maximum was observed at around 415 nm. These findings prove that cationic polythiophene derivative synthesized via FeCl_3 polymerization have two dominant conjugation length profiles lying between 11 and 37 monomer units.

CHAPTER 3

PREPARATION AND CHARACTERIZATION OF CONJUGATED POLYMER DOTS

In this chapter, structural and optical characteristics of poly(1-(3-((4-methylthiophen-3-yl)oxy)propyl-1,4-diazabicyclo[2.2.2]octan-1-ium)) (PT1, thereafter named as PT in this chapter) and its Pdot formation are discussed. Optical properties were analyzed by absorption, steady-state fluorescence spectroscopies, and time-correlated single photon counting technique. The structural features of PT and Pdot were analyzed by dynamic and static light scattering.

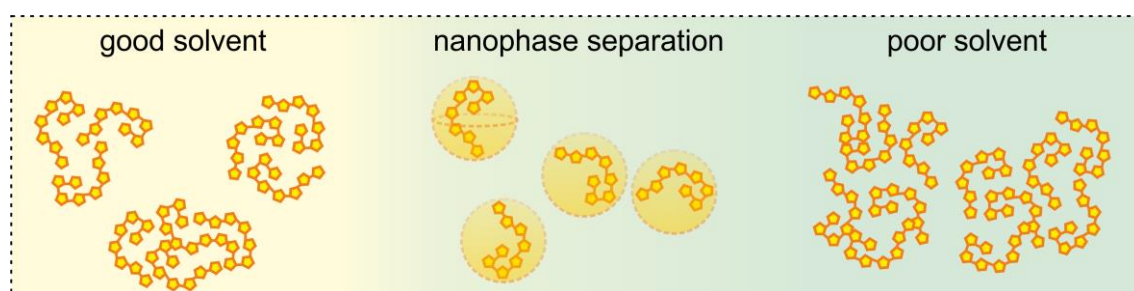


Figure 3.1. Schematic representation of Pdot formation by “nanophase separation” method between PT-rich ethylene glycol phase and PT-poor water phase.

Figure 3.1 represents a schematic for Pdot preparation via “nanophase separation” method. The cationic polyelectrolyte derivative of poly(1-(3-((4-methylthiophen-3-yl)oxy)propyl-1,4-diazabicyclo[2.2.2]octan-1-ium)) is firstly dissolved in ethylene glycol then added to water for formation of “nanophase separation”. The particle formation is relying on the thermodynamically driven mixing process of polymer and solvent molecules in a ternary mixture composed of its good and bad solvent system. The particle formation is relying on the thermodynamically driven mixing process of polymer and solvent molecules. The conformations of a real chain in good solvent are determined by entropic and enthalpic contributions of free energy of mixing. The excluded volume repulsive energy causes a polymer chain to expand in its good solvent which results in entropy loss due to such deformation on chain backbone. In the enthalpic contribution, the pairwise interaction energy characterizes the mixing process. As Flory suggested,

enthalpy change can be calculated by Flory interaction parameter (χ) defining the strength of pairwise energy between monomer and solvent molecules (equation 3.1).

$$\Delta U_{mix} = \chi \Phi_A \Phi_B kT \quad (3.1)$$

where χ is the Flory interaction parameter, Φ_A and Φ_B are the volume fractions of polymer and solvent. The smaller interaction parameter significantly drives the dissolution of polymer in good solvent to form a homogenous mixture. Therefore, nanophase separation method promotes phase separation between polymer rich good solvent and poor solvent in a ternary mixture. Mixing interaction parameter (B) is therefore declined in ethylene glycol solution of the polyelectrolyte than aqueous solution of it which indicates that ethylene glycol is good solvent for cationic polythiophene.

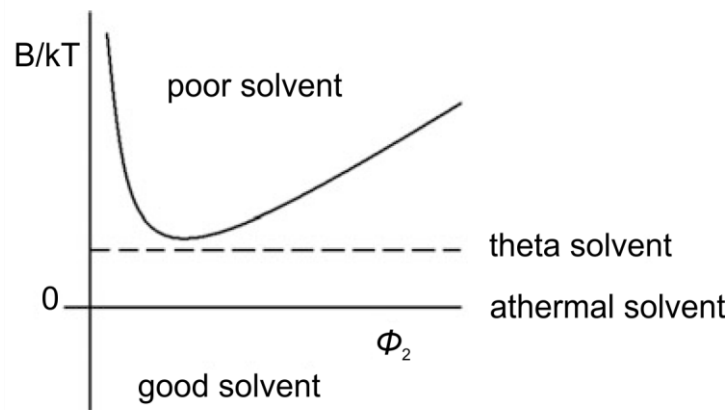


Figure 3.2. Illustration of the phase diagrams in polymer solutions showing the good and poor solvent regions and the demarcations for athermal ($B=0$) and theta solvents.⁶¹

The strong interaction occurring between EG and CPE sites reduces the excluded volume in chain and the possible ways that each adjacent monomer can randomly follow in a lattice space with a volume N stated in entropy of mixing (equation 3.2).

$$\Delta S_{mix} = -k \left[\frac{\Phi_A}{N_A} \ln \Phi_A + \frac{\Phi_B}{N_B} \ln \Phi_B \right] \quad (3.2)$$

Combination of mixing entropy and mixing heat (equations 3.1 and 3.2) into the mixing free energy, reveals the Flory-Huggins equation expressed in 3.3.

$$\Delta G_m = \Phi_A \ln \Phi_A + \frac{\Phi_B}{r} \ln \Phi_B + \chi \Phi_A \Phi_B$$

3.1. Materials and Methods

3-bromo-4-methylthiophene, 3-bromo-1-propanol, 1,4-dimethylpiperazine, 1-methyl-2-pyrrolidinone (NMP), copper bromide (CuBr), sodium bromide (NaBr), magnesium sulfate (MgSO₄), sodium hydrogen sulfate (NaHSO₄), iron(III) chloride (FeCl₃), diethyl ether, toluene, tetrahydrofuran (THF) and chloroform (CHCl₃), ethylene glycol, dimethyl sulfoxide (DMSO), 1,4-butanediol (BDO) were purchased from Sigma-Aldrich and MilliQ water with resistivity of 18.2 MΩ.cm was used in this chapter. The synthesis protocol of PT is given in Chapter 2.

For the optical and structural characterization, polyelectrolytes were dissolved in ethylene glycol with a solution concentration of 1.85x10⁻³ M. 50 μL of stock solution was then added to 1.5 mL MilliQ water while sonicated for 30 min to yield a Pdot solution of 6.0x10⁻⁵ M. After the simple preparation, Pdots formation was accomplished by the force of phase separation between ethylene glycol and water. The final solution is filtered with 0.2 μm hydrophilic PTFE (Millipore) filters: hydrophilic filter for aqueous solutions and hydrophobic filter for organic solvents before light scattering experiments.

Optical characterization of polyelectrolytes and Pdots was performed by UV-Visible absorbance spectroscopy, steady-state fluorescence spectroscopy and time-correlated single photon counting techniques. Absorption spectra of PT1 were recorded by Shimadzu UV 1800 spectrophotometer with a quartz cuvette of 0.1 cm optical path length and 1 cm width (Hellma). Fluorescence spectra were recorded by FluoroMax-3 (Horiba Jobin Yvon) with excitation at maximum absorption wavelengths of polyelectrolytes (400 nm for aqueous solution and 340 & 350 nm for ethylene glycol and DMSO, respectively). Time-correlated single photon counting (TCSPC) experiments were carried out with a FluoroLog-3 (Horiba Jobin Yvon) lifetime spectrofluorometer with integrated TCSPC software combined with a Fluoro3PS Precision Photomultiplier Power Supply and a FluoroHub Single Photon Counting Controller. The samples were analyzed using 10 x 10 mm quartz cuvette (Hellma) with the excitation wavelength at 405 nm.

Dynamic and static light scattering analyses were performed by an ALV CGS 3 goniometer with an ALV 5000 correlator (ALV Germany) equipped with a HeNe laser with a wavelength of $\lambda = 632.8$ nm and 20 mW output power. All the angular dependent light scattering analysis were covered in the range of $30 \leq \theta \leq 150^\circ$. Data analysis was performed by converting the measured intensity autocorrelation function into the electric field autocorrelation function using the Siegert relation. The electric field autocorrelation functions were then analyzed by regularized inverse Laplace transformation using the program CONTIN by S. Provencher to acquire the distribution of relaxation times. To determine the hydrodynamic radius R_H of the polyelectrolyte coils, the apparent diffusion coefficient D_{app} was extrapolated to zero scattering angle and then converted into R_H via the Stokes–Einstein relationship.⁵¹

3.2. Results and Discussion

For the preparation of conjugated polymer dots (Pdots), a new method called as “nanophase separation” has been introduced into literature by this thesis. Nanophase separation, as the name implies, is based on separation of two phases which are good and poor solvents of cationic conjugated polyelectrolyte (CPE). Detailed optical and colloidal characterization of polyelectrolyte in water, ethylene glycol, dimethyl sulfoxide (DMSO), and 1,4-butanediol (BDO) and Pdot form by nanophase separation of organic phases in aqueous environment will be discussed by spectroscopic and scattering techniques in this chapter.

3.2.1. Optical Characterization of CPE and Pdot

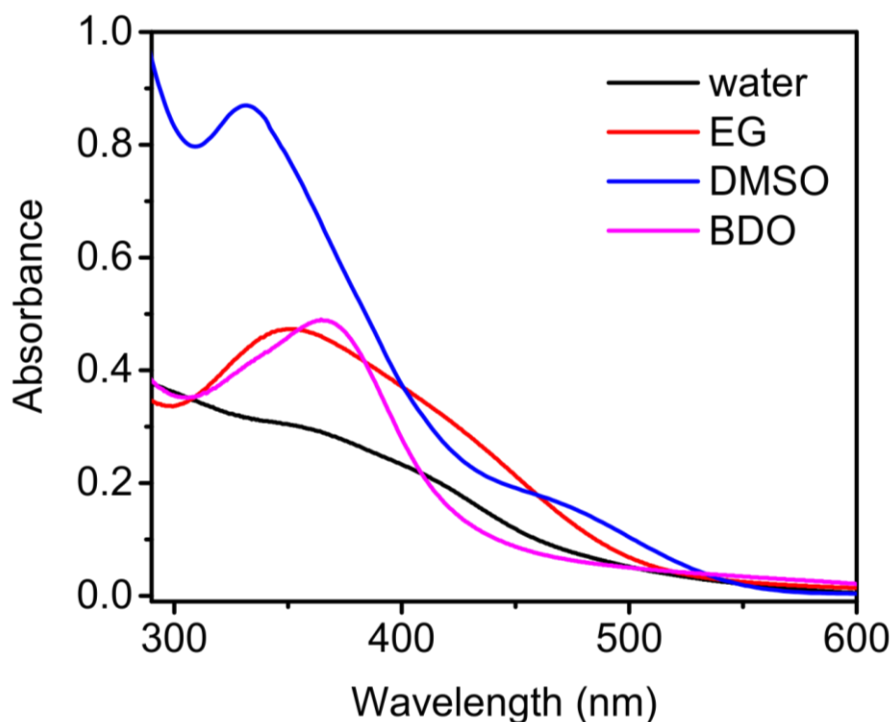


Figure 3.3. UV-Vis absorbance spectra of 1.85×10^{-3} M polyelectrolyte solutions of water, ethylene glycol, DMSO and BDO.

Figure 3.3 represents the absorbance spectra of polyelectrolyte dissolved in water, ethylene glycol, DMSO and BDO. Polyelectrolyte dissolved in water has absorbance maxima at 360 nm and 410 nm which are corresponding to π - π^* transitions of short and long chains of CPE, respectively. The electronic transitions in polyelectrolyte backbone dissolved in ethylene glycol are recorded as 350 nm and 415 nm as the detailed analysis for conjugation length can be seen in Figure 2.21. Since the polarities of water (1.00) and ethylene glycol (0.790) are similar, molecular orbitals are affected almost equivalently from the polarity of these solvents yielding analogous absorbance maxima for CPE in both water and ethylene glycol.⁶³ However, there are other parameters which must be considered by interpreting the absorbance spectrum of polyelectrolytes that will be discussed in this chapter. Due to the lower polarity of dimethyl sulfoxide (0.444), the π - π^* transitions of polyelectrolyte in DMSO environment were found to be 330 nm and 470 nm due to agglomeration behavior of CPE in DMSO with a longer conjugation length.

Maximum absorbance wavelength at 370 nm was observed for polyelectrolyte in 1,4 butanediol with a shoulder at around 330 nm.

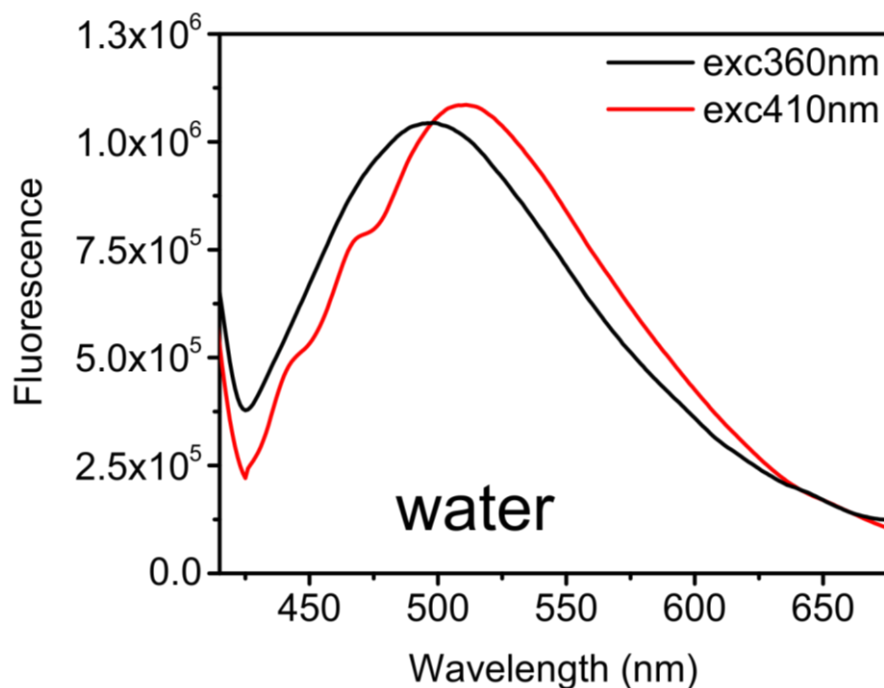


Figure 3.4. Fluorescence spectra of PT3 in water with excitation wavelengths 360 nm (black trace) and 410 nm (red trace).

Solvation characteristics of polyelectrolyte was further investigated by fluorescence spectroscopy. Figure 3.4 illustrates the emission spectra of polyelectrolyte dissolved in water with the excitation wavelengths 360 and 410 nm. Maximum emission wavelengths were found to be 500 nm and 510 nm, respectively. The fluorescence emission intensities of the spectra are around 1.0×10^6 and FWHM of the spectra excited at 360 and 410 nm were calculated by Gaussian fitting in OriginPro software as 108 and 116 nm.

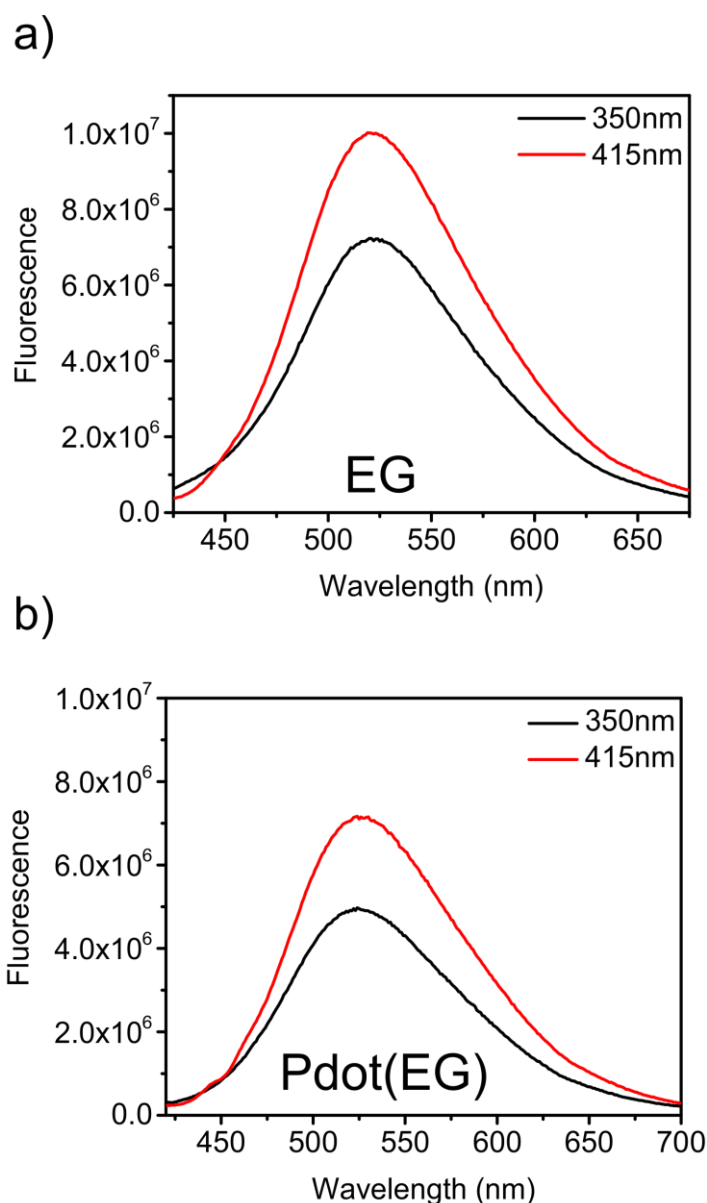


Figure 3.5. Fluorescence spectra of a) PT3 in ethylene glycol and b) Pdot with excitation wavelengths 350 nm (black trace) and 415 nm (red trace).

Figure 3.5 displays the emission characteristics of polyelectrolyte dissolved in EG and Pdot prepared by “nanophase separation” between water and ethylene glycol. The maximum fluorescence emissions of polyelectrolyte in EG and Pdot(EG) were recorded at 520 nm and 525 nm, respectively and no distinct difference was observed in both maximum emission wavelength and FWHM for excitation of 350 nm and 415 nm. Fluorescence intensity of polyelectrolyte in EG was observed as around 1.0×10^7 which is 10 fold greater than that of polyelectrolyte in water. Since ethylene glycol is good solvent for polyelectrolyte, it can reduce the interchain interaction therefore fluorescence

emission would enhance. However, in the water case, nonradiative emission more dominant because of the aggregation behavior causing the π - π stacking in the polyelectrolyte chain. The colloidal features of polyelectrolyte in solvents will be discussed in detail in Chapter 3.2.2. Additionally, the fluorescence emission intensity of Pdot(EG) is observed at around 7.0×10^6 which is also higher than that of water.

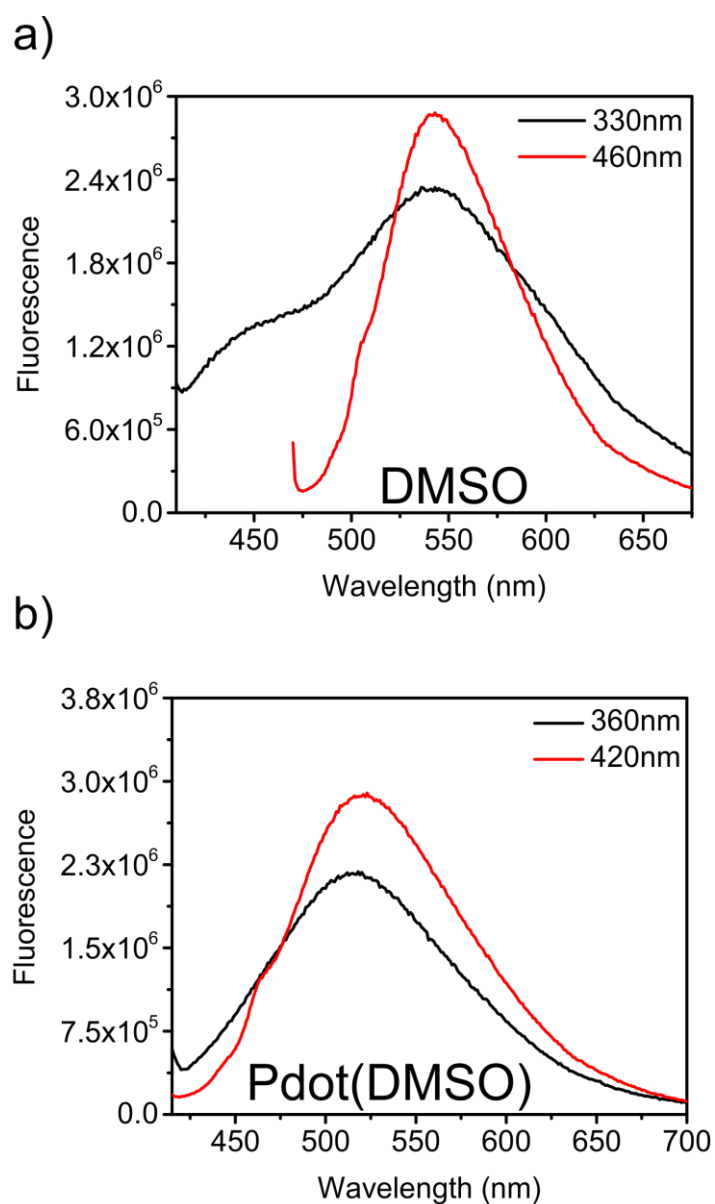


Figure 3.6. Fluorescence spectra of a) PT1 in DMSO and b) Pdot with excitation wavelengths 330/360 nm (black trace) and 460/420 nm (red trace) for DMSO and Pdot(DMSO), respectively.

The fluorescence emission spectra of polyelectrolyte in dimethyl sulfoxide and Pdot prepared by nanophase separation of water and DMSO were demonstrated in Figure 3.6. Excitation of polyelectrolyte in DMSO at 330 nm yielded a maximum fluorescence emission at 540 nm with a shoulder at around 445 nm. The broadness of emission spectrum with the excitation at 330 nm indicates numerous vibronic transitions which mostly disappear in the spectrum of excitation at 460 nm giving a concrete fluorescence maximum at 540 nm. The fluorescence emissions were observed at 520 nm in Pdot(DMSO). The 20 nm hypsochromic shift in Pdot could be attributed to alteration in chain conformation in DMSO-water mixture because in general, increasing polarity causes bathochromic shift due to the lowered energy bandgap.

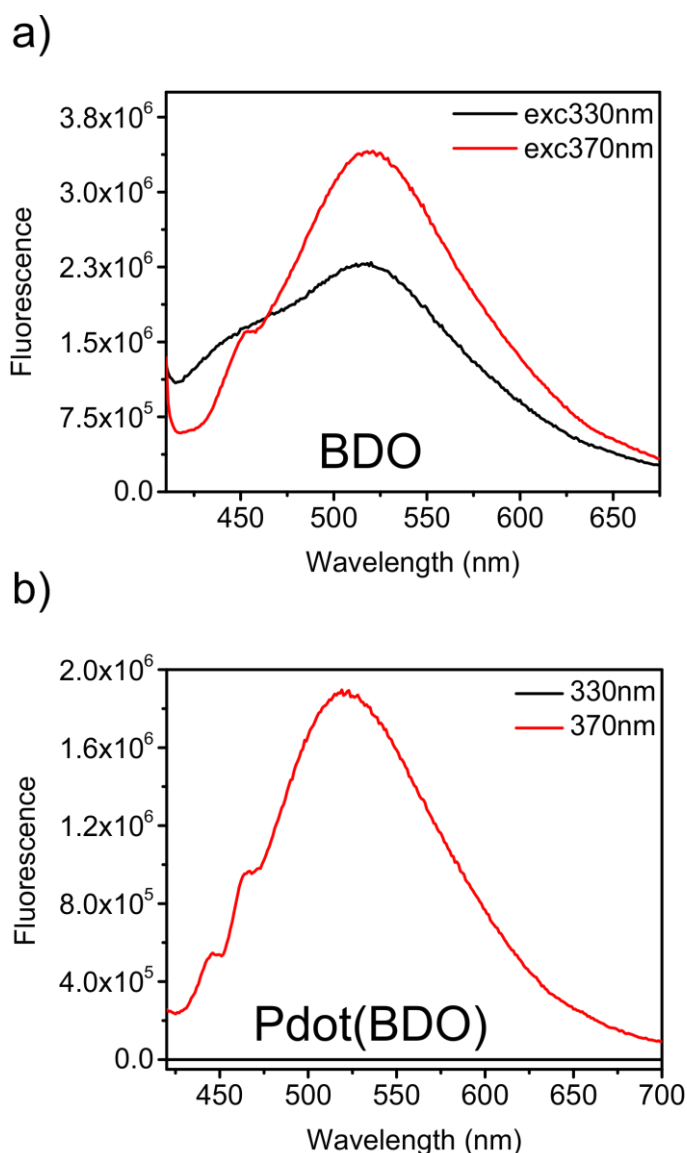


Figure 3.7. Fluorescence spectra of a) PT1 in BDO and b) Pdot with excitation wavelengths 330 nm (black trace) and 370 nm (red trace).

Figure 3.7 presents the fluorescence emission spectra of polyelectrolyte in 1,4 butanediol and Pdot(BDO) prepared by nanophase separation between water and BDO. The dominant fluorescence peaks are recorded at 450 and 515 nm for excitation at 330 nm whereas π - π^* transition at 370 nm for CPE in BDO has reduced the contribution of high energy emissive characteristic and enhanced the fluorescence emission at 515 nm. On the other hand, Pdot(BDO) does not show fluorescence emission when it is excited at 330 nm due to intermolecular non-radiative emission like in fluorescent molecular rotors.⁶⁴ However, fluorescence emission of Pdot(BDO) was found to be at 520 nm with an intensity of around 2.0×10^6 .

Table 3.1. Photophysical data of PT1 dissolved in water, ethylene glycol, DMSO, 1,4-BDO and Pdot forms of polyelectrolyte in each solvent.

	Excitation (nm)	Emission (nm)	Stokes Shift (nm)	FL Intensity ($\times 10^6$)	FWHM (nm)
Water	360	500	140	1.04	108
	410	510	100	1.08	116
EG	350	520	170	7.23	86
	415	520	105	10.1	85
Pdot(EG)	350	525	175	4.93	91
	415	525	110	7.17	92
DMSO	330	445-540	115-210	2.36	59-113
	470	540	70	2.89	68
Pdot(DMSO)	360	515	155	2.19	104
	420	520	100	2.88	97
BDO	330	450-515	120-185	2.30	55-114
	370	520	150	3.40	106
Pdot(BDO)	330	-	-	-	-
	370	520	150	1.89	101

Further optical characterization was carried out by time-correlated single photon counting (TCSPC) to understand the fluorescence decay phenomena of cationic polythiophene and its Pdot form in the 4-solvent system. Figure 3.8 illustrates the fluorescence decay of polyelectrolyte in water with respect to time. Polyelectrolyte has a bimodal relaxation behavior which are found to be 180 ps and 1.7 ns. The lifetime values may be associated to the emissive species with short- and long-chain polyelectrolytes. Moreover, their abundance was evaluated by Horiba Scientific DAS6 software as 76.25 and 23.75% for shorter and longer fluorescence decays, respectively.

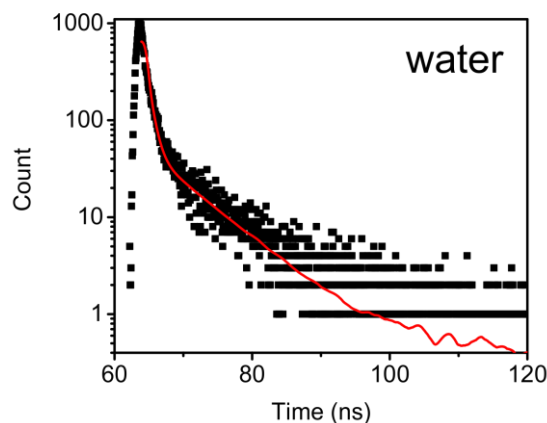


Figure 3.8. Fluorescence lifetime decay of PT1 dissolved in water.

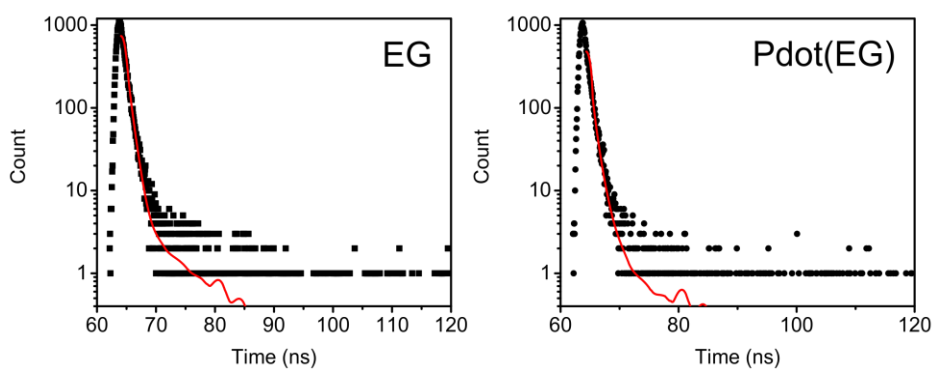


Figure 3.9. Fluorescence lifetime decay of PT1 dissolved in ethylene glycol (left) and Pdot (right).

Fluorescence emission decays of polyelectrolyte dissolved in ethylene glycol and its Pdot form are demonstrated in Figure 3.9. The lifetimes were calculated by two-exponential decay fitting on OriginPro software as 185 ps and 1.72 ns for polyelectrolyte in EG. 150 ps and 1.08 ns lifetime decays were observed for Pdot prepared by nanophase separation between water and ethylene glycol. The percent abundance of short- and long-chain polyelectrolytes was found to be 97.49 and 2.51% for CPE(inEG), 87.27 and 12.73% for Pdot(EG). It was observed that the abundance of long-chain CPE in EG is lower than that in water and can be attributed conformation of polyelectrolyte in ethylene glycol which more twisted with a shorter conjugation length. The π - π stacking in polyelectrolyte backbone in water enhances the interchain interaction, increasing the population of longer lifetime specie whereas the polyelectrolyte chains are well separated by ethylene glycol molecules as it is mentioned earlier that EG is the good solvent of cationic conjugated polythiophene derivatives, therefore short lifetime specie was

dominantly observed in TCSPC experiments.^{65,66} This separation also induces the increase in fluorescence emission intensity of ethylene glycol solution of polyelectrolyte. On the other hand, Pdot(EG) exhibits interchain interaction due to the bulk aqueous environment in 2-phase system, yielding rise in long lifetime specie in time domain fluorescence analysis but still allowing the radiative emission with a higher intensity (see Chapter 3.2.1).

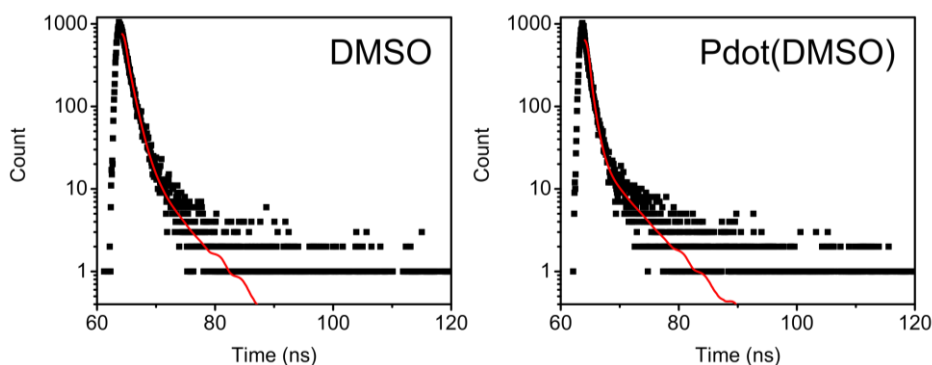


Figure 3.10. Fluorescence lifetime decay of PT1 dissolved in DMSO (left) and Pdot (right).

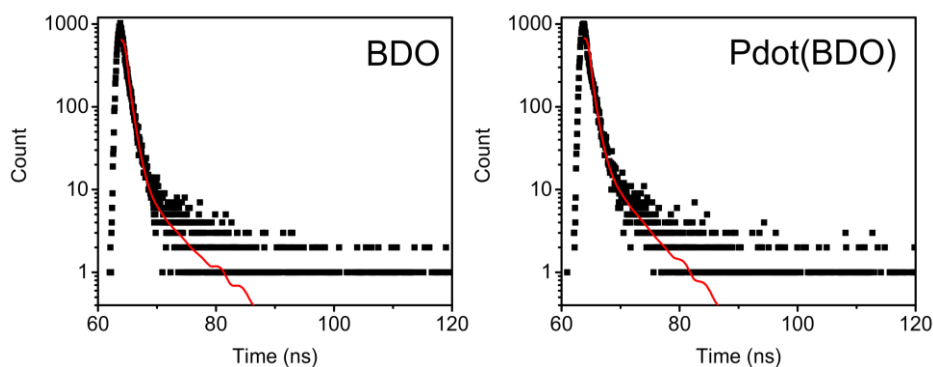


Figure 3.11. Fluorescence lifetime decay of PT1 dissolved in BDO (left) and Pdot (right).

Lifetime decays of polyelectrolyte dissolved in DMSO were found to be 265 ps and 1.16 ns and those of Pdot formed from water - DMSO separation were 185 ps and 1.23 ns shown in Figure 3.10. Similar feature with ethylene glycol solutions was also observed for more planarized conformation of polyelectrolyte in DMSO. Instead of π - π stacking, interaction between polyelectrolyte backbone and DMSO molecules drives a more planar conformation, not dominating the long lifetime structure but promoting the higher radiative emission in steady-state fluorescence of DMSO solution of

polyelectrolyte than CPE in water. Moreover, lifetimes of CPE dissolved and BDO and its Pdot form was also fitted by biexponential decay and very similar τ values were found as 0.198 ns and around 1.2 ns with a dominance of short-lived fluorescent specie. Overall, the data (lifetimes, τ_1 - τ_2 and corresponding abundance) obtained from TCSPC experiment of polyelectrolytes in different solvation characteristics are listed in Table 3.2.

Table 3.2. Fluorescence lifetime relaxation times and their relative abundance of polyelectrolyte dissolved in water, ethylene glycol, DMSO, BDO and Pdot forms of polyelectrolyte in each solvent.

	τ_1 (ns)	A ₁ (%)	τ_2 (ns)	A ₂ (%)
water	0.180	76.25	1.700	23.75
EG	0.185	97.49	1.720	2.51
Pdot(EG)	0.150	87.27	1.080	12.73
DMSO	0.265	91.01	1.160	8.99
Pdot(DMSO)	0.185	88.45	1.230	11.55
BDO	0.198	93.54	1.260	6.46
Pdot(BDO)	0.198	90.20	1.150	9.80

3.2.2. Colloidal characterization of CPE and Pdot

3.2.2.1. Polyelectrolyte - Water System

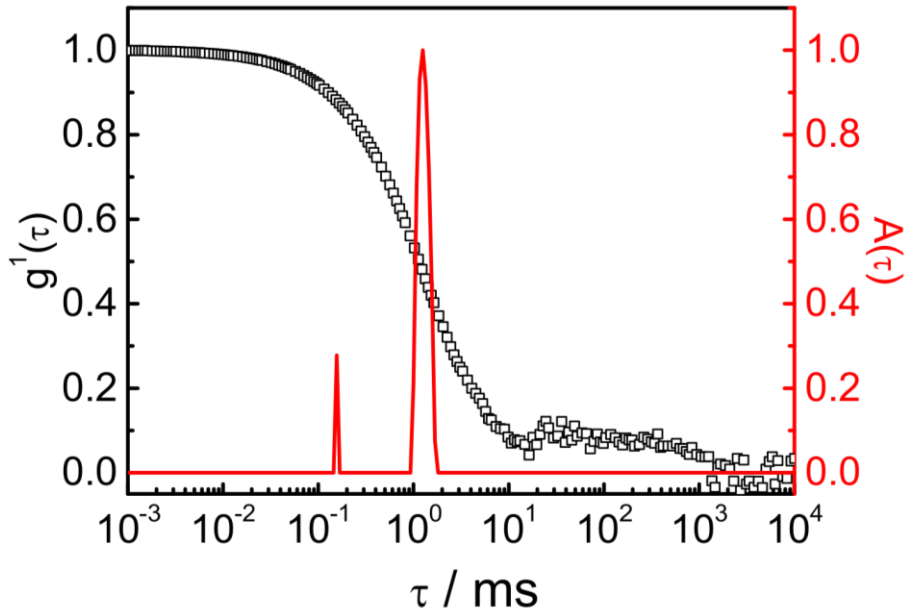


Figure 3.12. Autocorrelation function $g_1(\tau)$ and distribution of scattering relaxation times $A(\tau)$ of PT1 in water at a scattering angle of $\Theta = 90^\circ$.

Figure 3.12 shows electric field autocorrelation function $g_1(\tau)$ at 90°C and relaxation time distribution $A(\tau)$ of conjugated polyelectrolyte dissolved in water by multi angle light scattering. Autocorrelation function has a bimodal decay with relaxation times (τ) at 0.16 and 1.2 ms at 90° , moreover; the peak weight and the relative peak width values are calculated as 5.3% and 1.63×10^{-3} for fast decay and 94.7% and 0.13 by CONTIN software for slow decay, respectively. Hydrodynamic radius (R_H) of polyelectrolyte in water was then calculated from Stokes-Einstein equation (1.4) as 181 nm by using the extrapolated diffusion coefficient plot in Figure 3.13a. Diffusion coefficients of polymer particles in water has a linear trend as a function of scattering angle with R^2 : 0.91. The linear regression was applied for determining the extrapolated diffusion coefficient in angular dependent light scattering results.

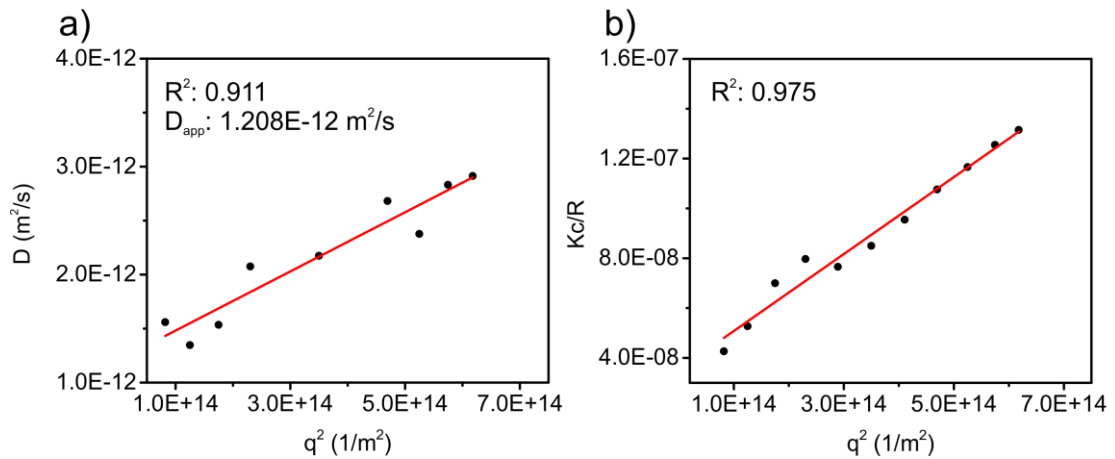


Figure 3.13. a) Diffusion coefficient from dynamic light scattering (DLS) and b) Zimm plot from SLS of PT1 in water obtained.

Scattering intensity (Kc/R) with respect to scattering wave vector (q^2) which is hereafter called as Zimm plot, is given in Figure 3.13b. Scattering intensities have linear dependency to the scattering angles ($30 \leq \theta \leq 150^\circ$, 10° intervals) with $R^2: 0.98$. Zimm plot provides the evaluation of radius of gyration in equations 1.7 and 1.8. Extrapolation from the linear regression function and the slope were deducted from the Zimm plot. Radius of gyration (R_g) and ρ -ratio (R_g/R_H) were then found to be 114 nm and 0.64 which indicates a homogenous sphere.⁵¹ From the relation of where R is the geometric radius of sphere, 0.63 ρ -ratio fits with homogenous sphere geometry.

3.2.2.2. Polyelectrolyte / Pdot - Ethylene Glycol System

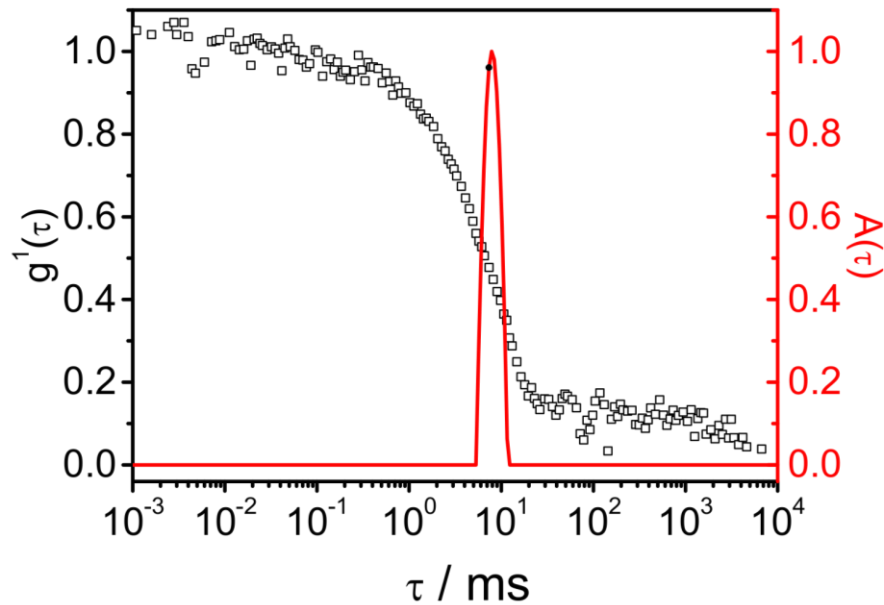


Figure 3.14. Autocorrelation function $g_1(\tau)$ and distribution of scattering relaxation times $A(\tau)$ of PT1 in ethylene glycol (EG) at a scattering angle of $\Theta = 90^\circ$.

Figure 3.14 demonstrates the electric field autocorrelation function $g^1(\tau)$ at 90°C and relaxation time distribution $A(t)$ of light scattering data of 1.85×10^{-3} M CPE dissolved in ethylene glycol solution. Filtration through $0.2 \mu\text{m}$ of hydrophilic and hydrophobic PTFE filters was applied to the solution before light scattering analysis of aqueous and organic solutions of polyelectrolyte, respectively. A monomodal relaxation behavior was characterized for ethylene glycol solution of polyelectrolyte from $g^1(\tau)$ autocorrelation function which indicates that polymer particles have single size distribution in ethylene glycol medium. The relaxation times (τ) were found to be 7.09 ms via regularized fitting of correlation function decay. The relative peak width was calculated as 0.17. The linear regression was utilized for determining the extrapolated diffusion coefficients from angular dependent light scattering to calculate the hydrodynamic radius in Figure 3.15a. Diffusion coefficients of polyelectrolyte particles are slightly deviated from linearity in the angles $30^\circ - 40^\circ$ and $140^\circ - 150^\circ$, therefore linear regression reveals R^2 value as 0.865 in diffusion coefficient plot of CPE particles in ethylene glycol. This could be attributed to aggregate-like structures that are easily detected at both higher and lower angles. Excluding those angles, diffusion coefficients have a linear trend as a function of

scattering angle. From the extrapolated diffusion coefficient, hydrodynamic radius (R_H) of polyelectrolyte in ethylene glycol was calculated as 45 nm. Since ethylene glycol is good solvent for cationic polythiophene, polymer chains are well separated due to the dipole-dipole interaction between CPE and ethylene glycol rather than water. This phenomenon not only to enhance the photophysical properties of CPE in ethylene glycol but also to decrease the particle size. In Pdot form, the interaction energy between polyelectrolyte and ethylene glycol overcoming the thermal energy and drives particle formation surrounded by ethylene glycol medium and these PT-ethylene glycol droplets also stabilized by water molecules in which occurrence of polymer coil is not thermodynamically favorable.

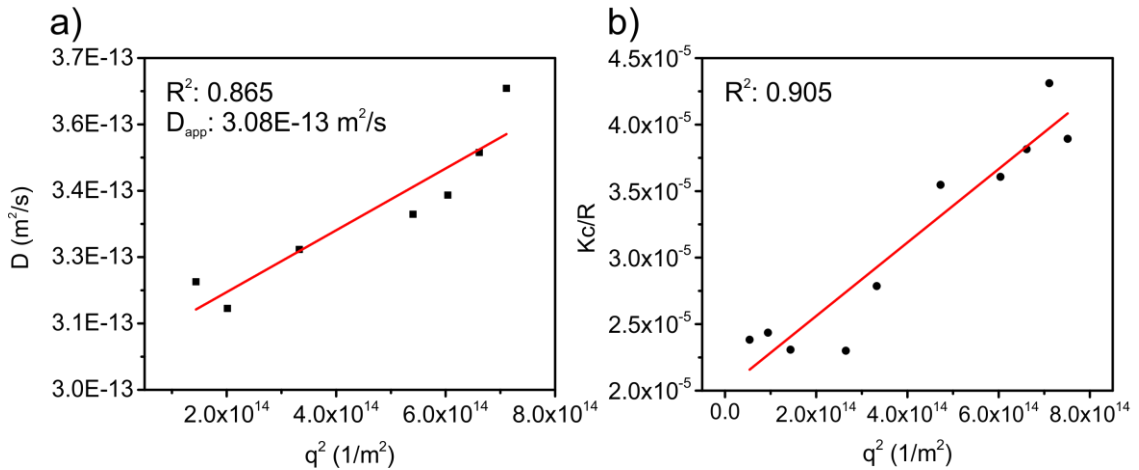


Figure 3.15. a) Diffusion coefficient from DLS and b) Zimm plot from SLS of PT1 in ethylene glycol (EG).

Zimm plot of polyelectrolyte in ethylene glycol is given in Figure 3.15b and scattering intensities have linear dependency to the scattering angles ($30 \leq \theta \leq 150^\circ$, 10° intervals) with $R^2: 0.905$. Moreover, the radius of gyration (R_g) was evaluated as 66 nm which then results in R_g/R_H (ρ -ratio) as 1.46 indicating a random coil polyelectrolyte conformation.

$g^1(\tau)$ autocorrelation function and distribution of dynamic light scattering analysis of Pdot formed by the separation between ethylene glycol with a volume fraction of 3.3 and water phases - Pdot(EG) at $90^\circ C$ is represented in Figure 3.16. A monomodal relaxation was observed for Pdots which indicates single size distribution, therefore, the relaxation time (τ) distribution peak was found to be 0.77 ms via regularized fitting of autocorrelation function with a peak with of 0.16. Diffusion coefficients of Pdot collected

from angular dependent light scattering has a linear distribution as a function of scattering angle with $R^2 : 0.73$ as demonstrated in Figure 3.17. The linear regression was applied for determining the extrapolated diffusion coefficients to zero by which hydrodynamic radius (R_H) of Pdot was directly calculated from Stokes-Einstein equation (1.4) as 4.7 nm. Since ethylene glycol is good solvent for cationic conjugated polyelectrolyte, the interaction between ethylene glycol and CPE is entropically more favorable than that between water and polyelectrolyte. Thus, nanophase separation takes place between ethylene glycol phase which is rich in polyelectrolyte and aqueous phase to yield small sized polymer dots. These findings prove the small sized fluorescent polymer dot preparation. In the previous section, the fluorescence emission characteristic of conjugated polyelectrolyte dissolved in EG and its Pdot form was discussed that polyelectrolyte in ethylene glycol system, both CPE(inEG) and Pdot(EG), possesses the most fluorescent conformation among the solvents with an ultra-small particle size.

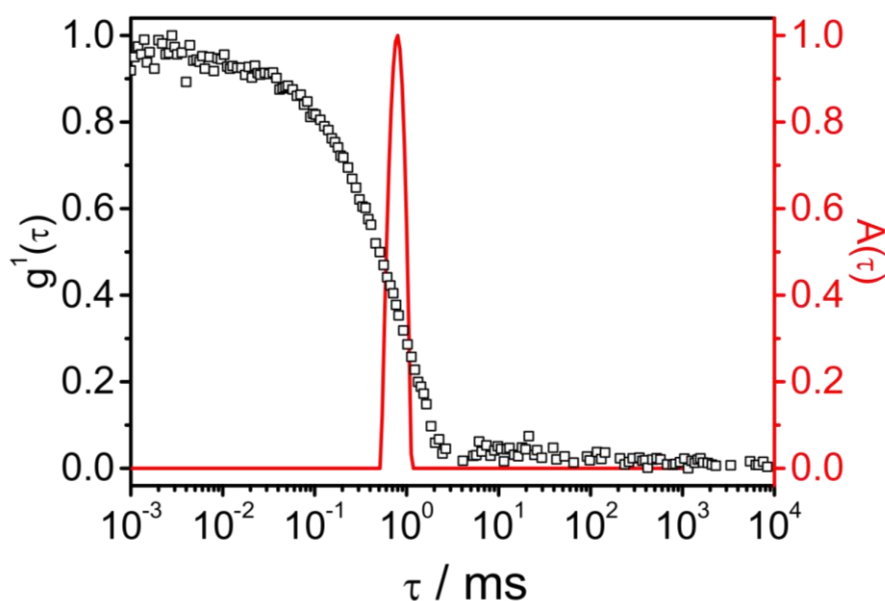


Figure 3.16. Autocorrelation function $g^1(\tau)$ and distribution of scattering relaxation times $A(\tau)$ of Pdot(EG) at a scattering angle of $\Theta = 90^\circ$.

Zimm plot of the static light scattering analysis of Pdot(EG) is shown in Figure 3.17b. Linearity of scattering intensities to the scattering angles was found to be slightly deviated with $R^2: 0.8346$. The radius of gyration (R_g) was surprisingly found to be 60 nm and ρ -ratio was calculated as 10.6 which is not a realistic value of the ratio of R_g to R_H for indication of a conformation which is expected between $\sim 0.6 - \sim 4$.⁵¹

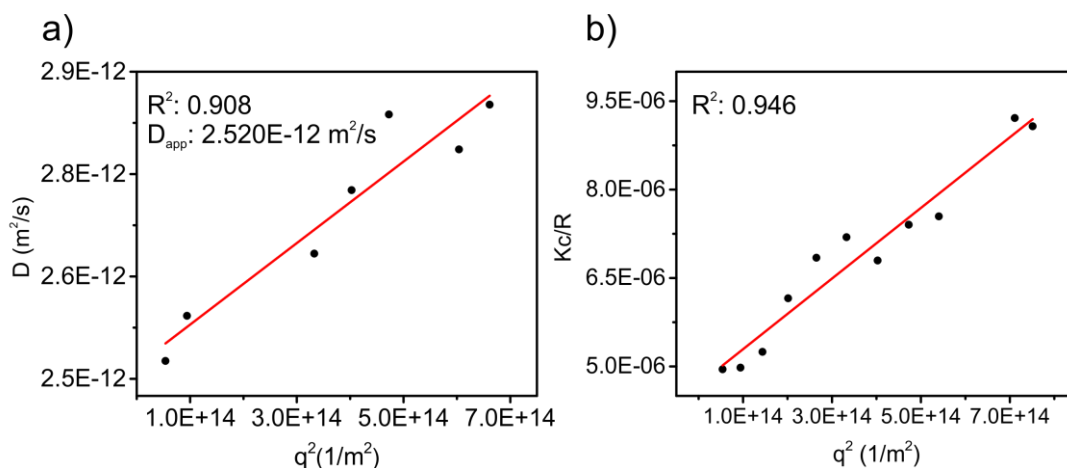


Figure 3.17. a) Diffusion coefficient plot from DLS and b) Zimm plot from SLS of Pdot(EG).

In the next step, light scattering analysis whose structural data given in Table 3.3, was conducted for Pdot(EG) solutions prepared by nanophase separation protocol with increasing ethylene glycol fractions. Increasing volume fraction of ethylene glycol causes hydrodynamic radius to be larger, approaching to 45 nm which is the R_H of CPE(inEG) which is correlated to the autocorrelation function $g_1(t)$ and the distribution of Pdot(EG) with increasing volume fraction of EG demonstrated in Figure 3.18.

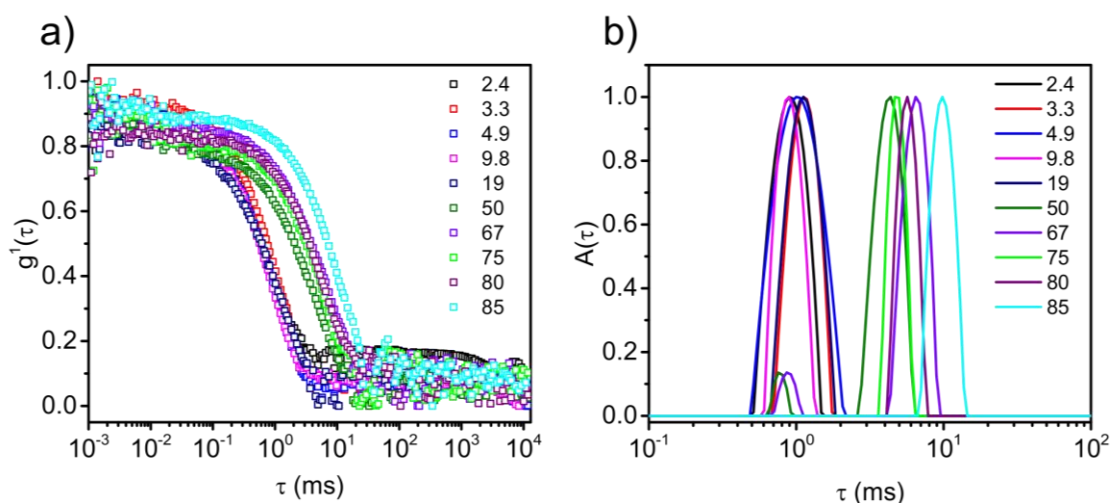


Figure 3.18. Autocorrelation function $g_1(\tau)$ and distribution of scattering relaxation times $A(\tau)$ of Pdot(EG) at a scattering angle of $\Theta = 90^\circ$ with increasing volume fraction ranging from 2.4 to 85.

Table 3.3. Dynamic and static light scattering data of Pdot(EG) with increasing volume fraction of EG ranging from 0 to 100 volume fraction.

Volume fraction of EG	R_H/nm	R_g/nm	ρ-ratio
0	180	115	0.64
2.4	4.0	71	17
3.3	5.2	62	11
4.9	4.5	64	14
9.8	4.8	74	13
19	6.4	68	11
50	14	81	5
67	22	70	2.5
75	26	86	2.7
80	35	45	1.2
85	43	146	2.7
100	44	66	1.52

Up to 50% volume fraction of ethylene glycol, CPE exhibits similar hydrodynamic radius within the range of 4.0 and 6.4 nm while increasing R_H values are observed in ethylene glycol-dominant characteristic of solvent system. The radius of gyration values calculated from static light scattering are found to be fluctuated from linearity with approximately 20 nm deviation at the higher ethylene glycol volume fraction. although ethylene glycol is a water-miscible solvent, 3-component system of Pdot; CPE, ethylene glycol, and water, causes phase separation between EG and water due to relatively strong interaction of EG molecules to side groups in CPE chain, creating heterogenous two-phase solvent system. Regarding of the heterogeneity in CPE environment, static light scattering analysis is less convenient techniques for such systems.

Figure 3.19 illustrates the Pdot concentration study with 3.3 volume fraction of ethylene glycol by light scattering analysis. In these polyelectrolyte concentration range, R_H values are slightly increasing from 5.1 nm to 8.4 nm. However, after around 2 mM polyelectrolyte concentration in 3.3 ethylene glycol volume fraction of Pdot addresses the increase polydispersity shown in Figure 3.19 c-f as the g₁(τ) is not decaying to zero. This can be attributed the aggregation formation of polyelectrolyte chains in a single ethylene glycol droplet. On the other hand, radius of gyration is getting larger with an increasing CPE concentration as the scattering intensities are deviated from linearity after ~7.5 mM of CPE. The overall light scattering data is represented in Table 3.4.

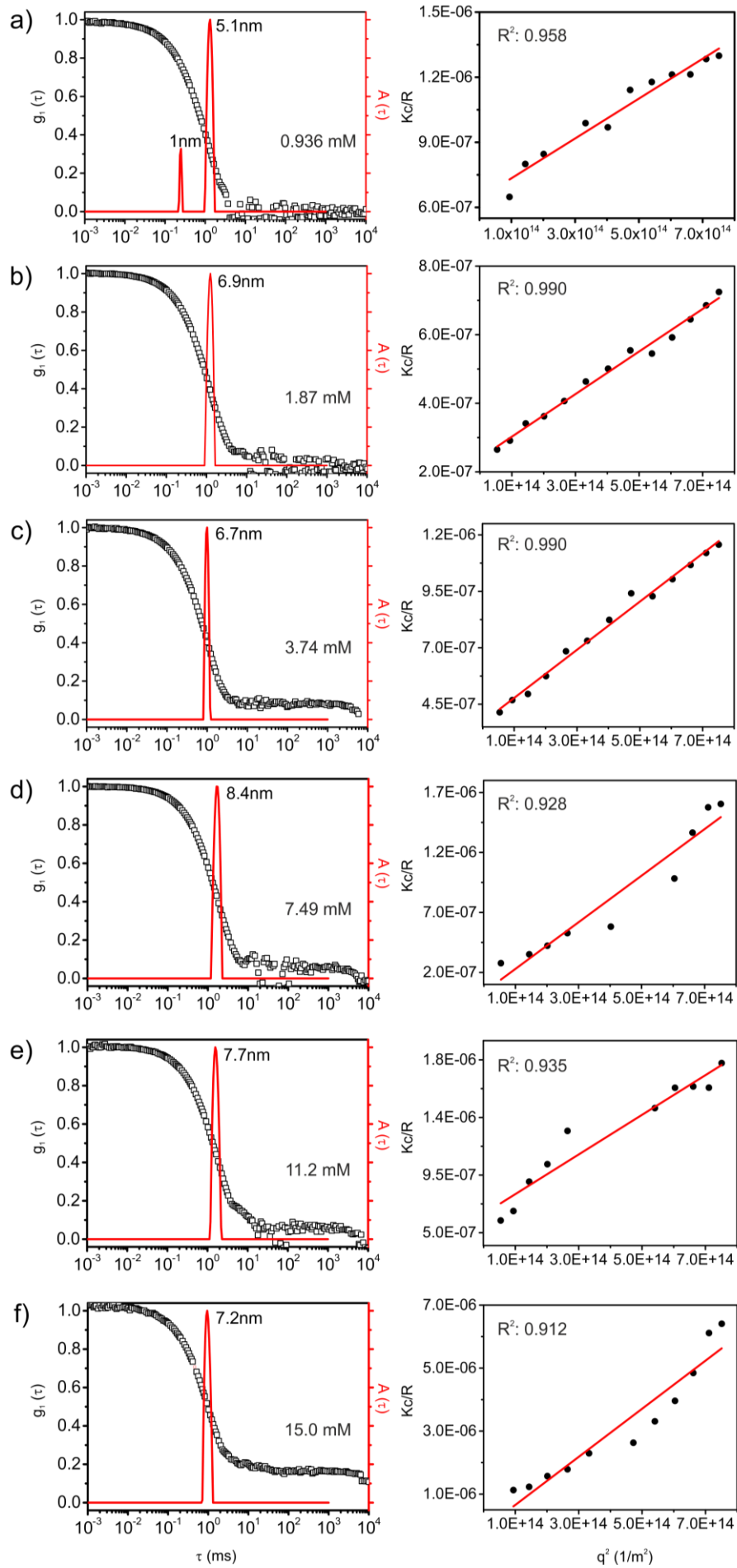


Figure 3.19. Light scattering analysis of Pdot(EG) with concentrations a) 0.94, b) 1.87, c) 3.74, d) 7.49, e) 11.2, and f) 15.0 mM. $g_1(\tau)$ autocorrelation functions and scattering intensity plot demonstrated at the left and right, respectively.

Table 3.4. Structural data of Pdot(EG) concentration study from light scattering analysis.

Pdot(EG) concentration (M)	R_H/nm	R_g/nm	K_c/R
1.11×10^{-3}	2.4	87	7.55×10^{-6}
1.48×10^{-3}	3.3	85	1.59×10^{-5}
1.87×10^{-3}	3.4	53	1.69×10^{-5}
2.78×10^{-3}	4.2	82	3.63×10^{-6}
3.74×10^{-3}	4.8	71	3.39×10^{-6}
5.57×10^{-3}	4.6	65	2.33×10^{-6}
7.49×10^{-3}	4.6	66	1.96×10^{-6}
1.12×10^{-2}	4.8	64	1.34×10^{-6}

Overall, polyelectrolyte conformation changes from homogeneous sphere to random coil in water and ethylene glycol, respectively. The clear transformation in geometry of polymer particles is attributed to the solvent-polymer interactions in which EG-CPE interaction is favorable whereas water-CPE is not favorable. The complexity of ethylene glycol – water mixture makes static light scattering analysis difficult to obtain a rational radius of gyration value for Pdot. Therefore, DMSO and 1,4-butanediol have been chosen with respect to refractive index and viscosity, for Pdot characterization after nanophase separation was applied.

3.2.2.3. Polyelectrolyte / Pdot - Dimethyl Sulfoxide System

For the comparison of R_H and R_g values of polyelectrolyte in Pdot form, aqueous mixtures of DMSO and BDO were utilized to dissolve CPE prior to nanophase separation and colloidal characterization was conducted by multi angle light scattering. Figure 3.20 demonstrates $g_1(\tau)$ autocorrelation function and relaxation time distribution of dynamic light scattering at 90°C of 1.87 mM polyelectrolyte dissolved in DMSO. Correlation function has a monomodal decay with relaxation time (τ) at 0.85 ms and relative peak width is calculated as 0.27. Hydrodynamic radius (R_H) of polyelectrolyte in DMSO was

found to be 113 nm. Diffusion coefficients of polymer particles in DMSO has a nearly linear trend as a function of scattering angle with R^2 : 0.826 in Figure 3.21a.

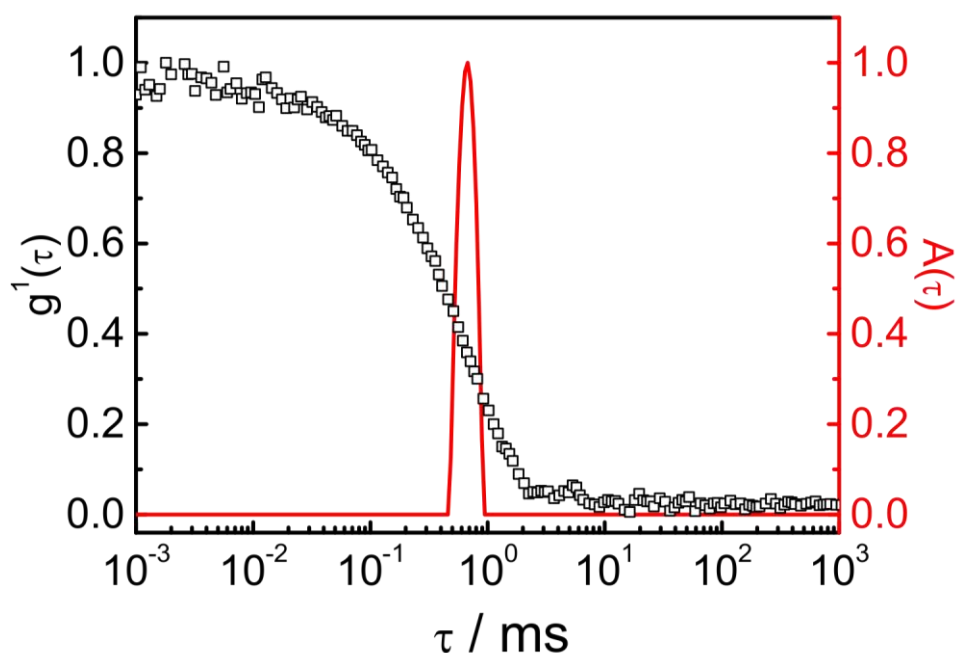


Figure 3.20. Autocorrelation function $g_1(\tau)$ and distribution of relaxation times $A(\tau)$ of PT1 in DMSO at a scattering angle of $\Theta = 90^\circ$.

Scattering intensity (Kc/R) with respect to scattering angles (q^2), Zimm plot of CPE(DMSO) is given in Figure 3.21b. Scattering intensities have linear dependency to the scattering angles ($30 \leq \theta \leq 150^\circ$, 10° intervals) with R^2 : 0.98. The radius of gyration (R_g) was calculated from Zimm equation as 120 nm thus R_g/R_H (ρ -ratio) was acquired as 1.06 which indicates a hollow sphere geometry (Table 1.1). The hydrophobic nature of polyelectrolyte backbone and the hydrophilicity of pendant groups drives a hollow sphere geometry in polythiophene chain. The backbone forms bagel-like structure interacting mostly with dimethyl sulfoxide due to relatively lower polarity of DMSO and having a sulfinyl group.

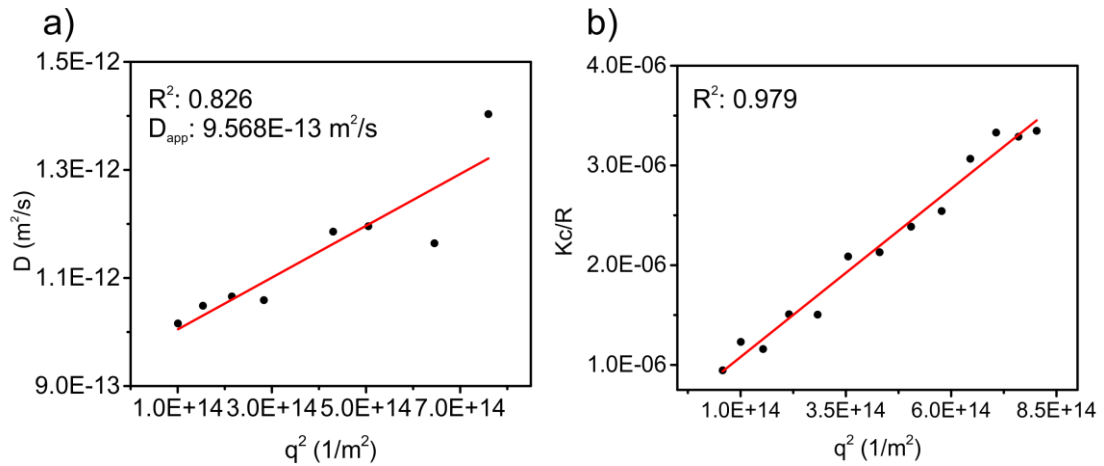


Figure 3.21. a) Diffusion coefficient from DLS and b) Zimm plot from SLS of PT1 in DMSO.

$g_1(\tau)$ correlation function and distribution of dynamic light scattering of Pdot solution of DMSO with a 3.3 volume fraction at 90°C is illustrated in Figure 3.22. A monomodal relaxation and broadened distribution similar to CPE(DMSO) solution were observed for Pdot(DMSO) prepared by nanophase separation method. The relaxation time (τ) were found to be 0.79 ms via regularized fitting of correlation function decay and the relative peak width was found as 0.22. Diffusion coefficients of Pdot has a linear distribution as a function of scattering angle with $R^2: 0.90$. By extrapolating diffusion coefficients to the zero angle, hydrodynamic radius (R_H) of Pdot (DMSO) was calculated as 48 nm from Stokes-Einstein relation which is nearly 2 fold smaller than that of CPE(DMSO) particles.

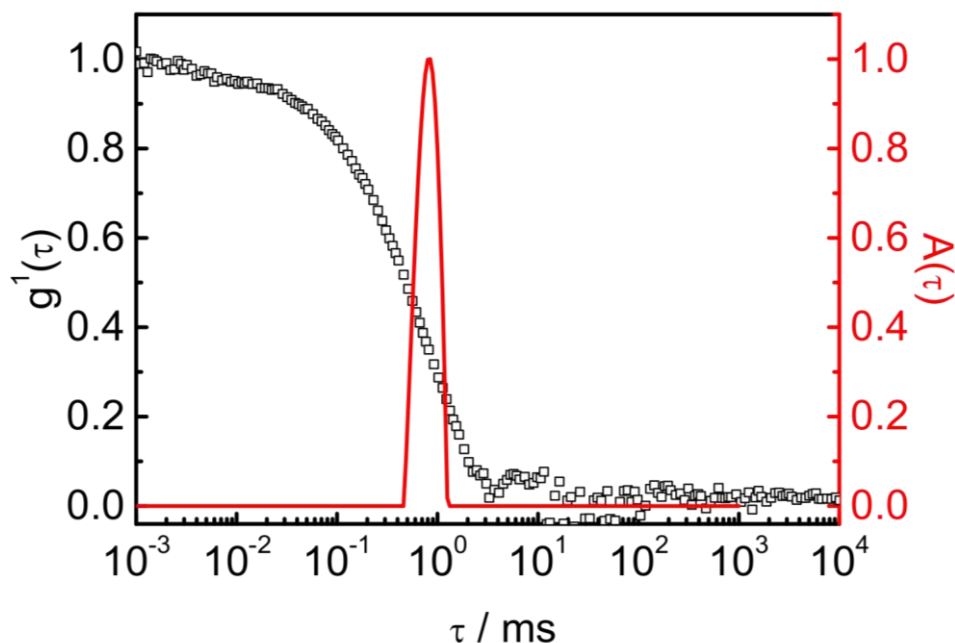


Figure 3.22. Autocorrelation function $g_1(\tau)$ and distribution of relaxation times $A(\tau)$ of Pdot(DMSO) at a scattering angle of $\Theta = 90^\circ$.

Zimm plot from the static light scattering analysis of Pdot is illustrated in Figure 3.23b. Scattering intensities have linear dependency to the scattering angles ($30 \leq \theta \leq 150^\circ$, 10° intervals) with R^2 : 1.00. The radius of gyration (R_g) was calculated as 62 nm and R_g/R_H (ρ -ratio) was further found to be 1.31. The ρ -ratio indicates a polyelectrolyte conformation in between sphere and random coil geometry.

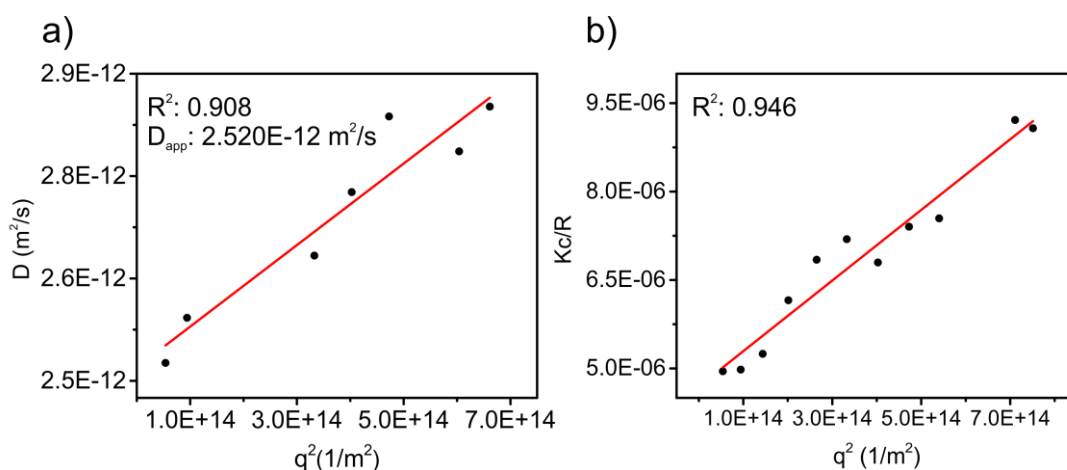


Figure 3.23. a) Diffusion coefficient from DLS and b) Zimm plot from SLS of Pdot(DMSO).

Table 3.5. Dynamic and static light scattering data for Pdot(DMSO) having DMSO volume fraction (ϕ) ranging from 0 to 67.

Volume fraction of DMSO	R_H (nm)	R_g (nm)	ρ-ratio
0	180	114	0.64
2.4	53	80	1.53
3.3	35	48	1.39
4.9	39	47	1.21
9.8	46	49	1.06
19	46	56	1.16
50	80	49	0.61
67	106	62	0.58

Table 3.5 and Figure 3.24 represent the structural characterization of Pdot(DMSO) prepared with DMSO volume fractions ranging from 0 to 67. Autocorrelation function $g_1(\tau)$ and relaxation time distribution $A(\tau)$ are given in Figure 3.43a and b, respectively. Autocorrelation function of Pdot(DMSO) indicates that scattering intensities from 2.4 to 19 percentage are fluctuating and the intensity of 50% DMSO volume fraction drops suddenly which is the indication of a sharp decrease in diffusion of agglomerated particles with a slight sedimentation. The relatively larger particles are stabilized after 50% (v:v) DMSO content. Hydrodynamic radii of polymer dots prepared by altering DMSO volume fraction is within the almost equivalent range between 35 to 53 nm. However, the volume fractions 50 and 67 show an increasing trend in R_H value calculated as 80 and 106 nm, respectively. Static light scattering analysis reveals that radius of gyration value for the polyelectrolyte in the each DMSO volume fraction are ranging from 47 to 62 except than the volume fraction, ϕ : 2.4 which is found to be 80 nm. From the Zimm plot, the ρ -ratios are calculated in between 1.53 and 0.58 with a decreasing trend from low to high DMSO content CPE solutions (ϕ : from 2.4 to 67). This finding proves that a conformational change from random coil to homogenous sphere geometry occurs. The difference between the relative polarity of DMSO (0.444) and polarity of water (1.00) is significantly distinguishable than that between ethylene glycol (0.789) and water.

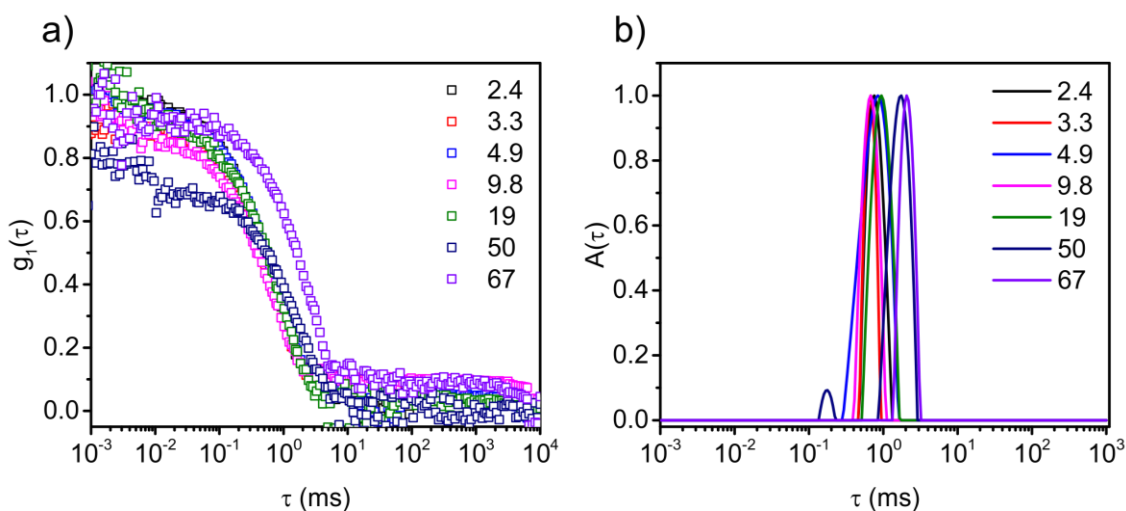


Figure 3.24. Autocorrelation function $g_1(\tau)$ and b) relaxation time distribution $A(\tau)$ for Pdot(DMSO) with DMSO volume fraction from 2.4 to 67.

3.2.2.4. Polyelectrolyte /Pdot - 1,4-Butanediol System

As a complementary characterization of conjugated polymer dots prepared by phase separation between ethylene glycol and water, 1,4-butanediol (BDO) was utilized as organic phase in “nanophase separation” regarding its refractive index (1.446) and viscosity (84.9 mPa.s) which are more comparable with those of ethylene glycol (1.429 and 16.1 mPa.s). Figure 3.25 demonstrates $g_1(\tau)$ autocorrelation function and relaxation time distribution of polyelectrolyte dissolved in 1,4-butanediol, CPE(BDO), at 90°C. Correlation function was observed as a monomodal decay with relaxation time (τ) at 46 ms due to high viscosity of BDO. High viscosity reduces the Brownian motion of polyelectrolyte particles in BDO and finally resulting in relatively slow scattering relaxation time. Relative peak width is found to be 0.17 and hydrodynamic radius (R_H) of polyelectrolyte in BDO was calculated as 65 nm.

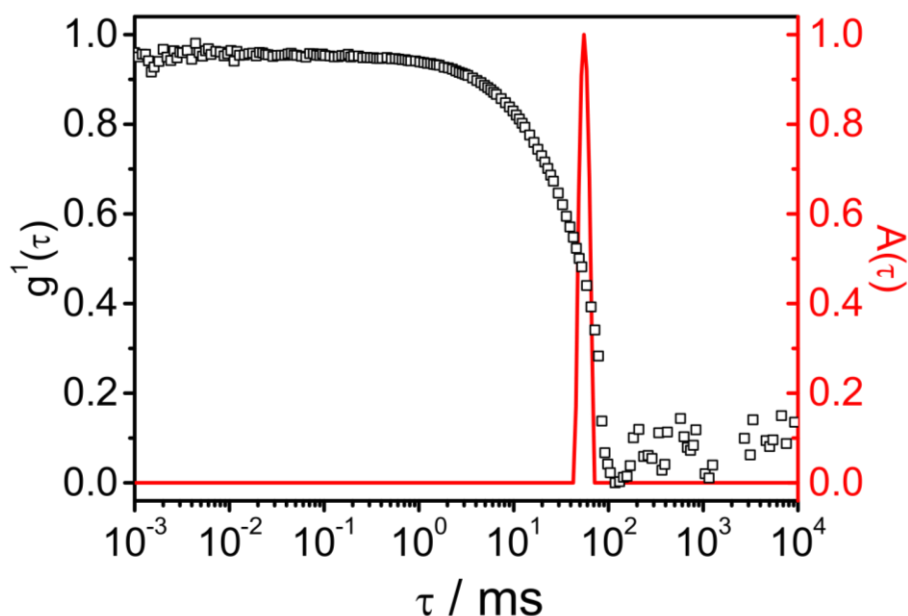


Figure 3.25. Autocorrelation function $g_1(\tau)$ and relaxation time distributions $A(\tau)$ of PT1 in 1,4-BDO at a scattering angle of $\Theta = 90^\circ$.

Zimm plot of CPE(BDO) is given in Figure 3.26b as scattering intensities have nearly a linear dependency to the scattering angles ($30 \leq \theta \leq 150^\circ$, 10° intervals) with R^2 : 0.82. The radius of gyration (R_g) of CPE(BDO) was found to be 97 nm from Zimm equation and ρ -ratio was calculated as 1.49 which is directly defining a random polymer coil (Table 1.1). These structural findings prove that BDO is good solvent for polyelectrolyte and provide an environment to reduce the backbone planarization for an entropically favorable chain conformation.

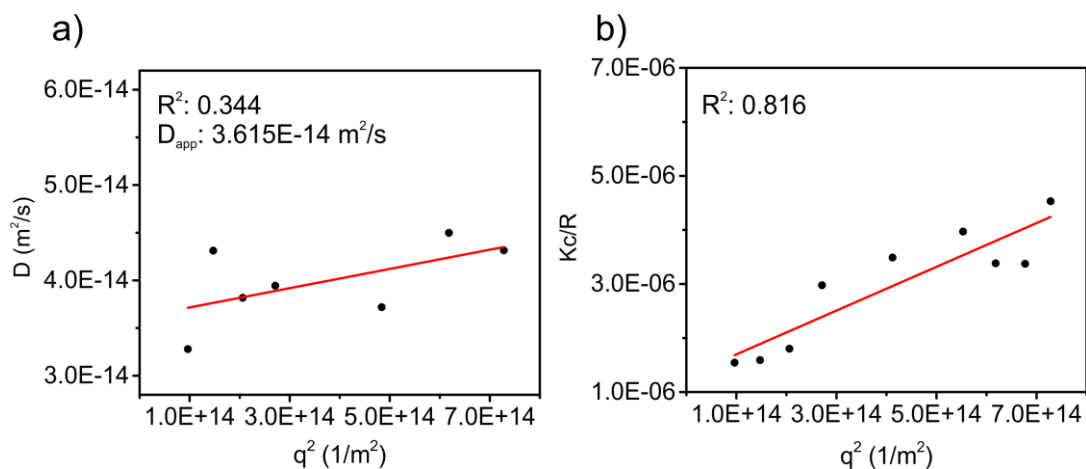


Figure 3.26. a) Diffusion coefficient from DLS and b) Zimm plot from SLS of PT1 dissolved in BDO.

$g^1(\tau)$ electric autocorrelation function and relaxation time distribution of Pdot form of PT4 in BDO with a volume fraction of 3.3 at 90°C is illustrated in Figure 3.27. A monomodal relaxation distribution was observed for Pdots prepared by nanophase separation between BDO and water. The relaxation time (τ) was found to be 1 ms via regularized fitting of correlation function decay which is quite faster than that in absolute BDO system. The water system surrounding the BDO droplets which have polyelectrolyte particles can reduce the high viscosity effect of BDO system in nanophase separation. The relative peak width was then found as 0.20 and also diffusion coefficients of Pdot has a linear distribution as a function of scattering angle with R^2 : 0.81 in Figure 3.28a. By extrapolating diffusion coefficients to the zero angle, hydrodynamic radius (R_H) of Pdot(BDO) was calculated as ~ 1.1 nm. As BDO is good solvent of polyelectrolyte, the PT particles thermodynamically tend to be in 1,4-butanediol droplets rather than water then the water environment can separate polyelectrolyte particle containing droplets as small as a single chain polymer similar to ethylene glycol case.

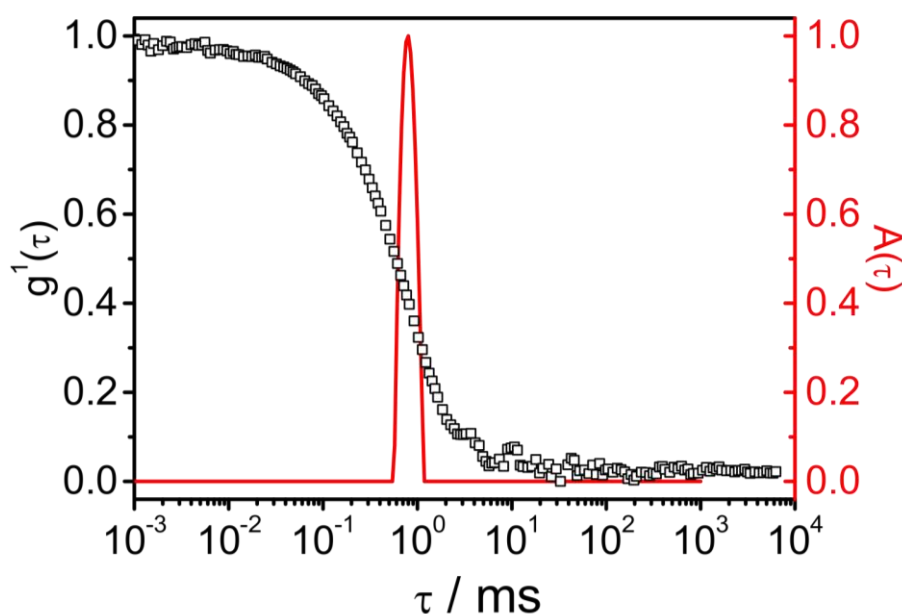


Figure 3.27. Autocorrelation function $g_1(\tau)$ and relaxation time distribution $A(\tau)$ of Pdot(BDO) at a scattering angle of $\Theta = 90^\circ$.

Zimm plot from the static light scattering analysis of Pdot(BDO) is shown in Figure 3.28b. Scattering intensities have linear dependency to the scattering angles ($30 \leq \theta \leq 150^\circ$, 10° intervals) with R^2 : 0.95. The radius of gyration (R_g) was found to be 65 nm

and R_g/R_H (ρ -ratio) was calculated as 58. The ρ -ratio calculated for Pdots prepared with BDO is not rational similar to that of Pdot(EG) (see Table 3.6).

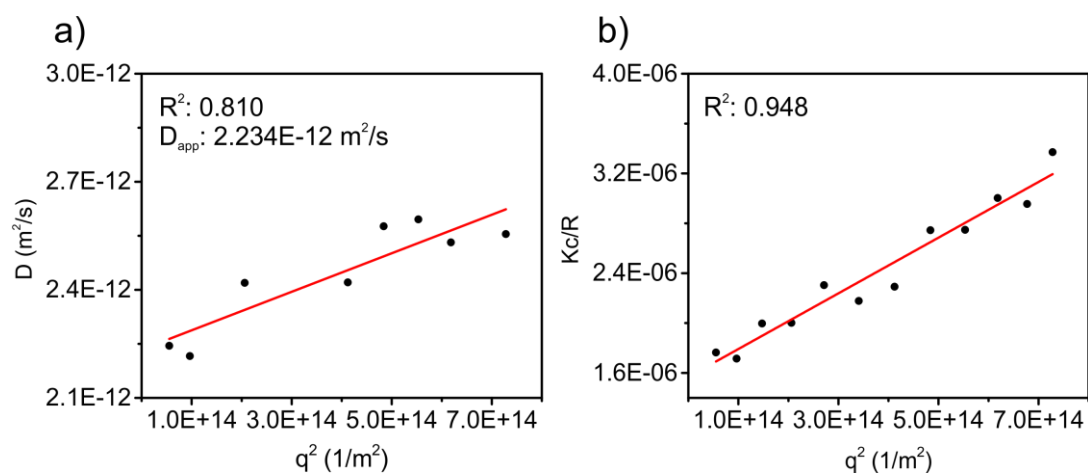


Figure 3.28. a) Diffusion coefficient from DLS and b) Zimm plot from SLS of Pdot(BDO).

Table 3.6. Overall structural data from dynamic and static light scattering of polyelectrolyte in water, ethylene glycol, DMSO, BDO and their corresponding Pdot forms.

	R_H (nm)	R_g (nm)	ρ -ratio
water	180	114	0.64
EG	44	66	1.52
Pdot(EG)	5.3	68	ND
DMSO	114	119	1.05
Pdot(DMSO)	35	41	1.18
BDO	65	97	1.49
Pdot(BDO)	1.1	65	ND

3.3. Polyelectrolyte - DNA Complexation

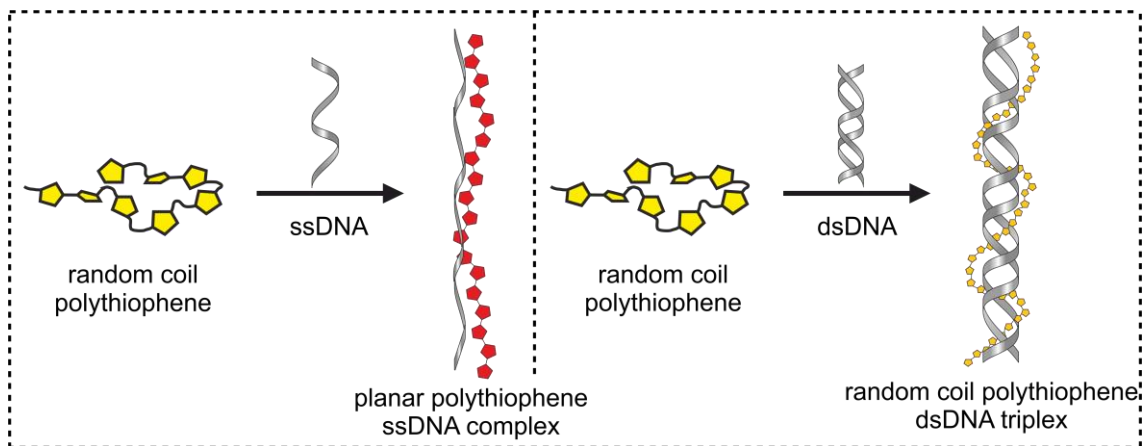


Figure 3.29. Schematic for cationic conjugated polythiophene (PT) and DNA complexation.

The interaction between cationic conjugated polyelectrolyte and single-stranded DNA (ssDNA)/double-stranded DNA (dsDNA) is shown in Figure 3.29. The interaction is relying on the electrostatic interactions between the positive charges on the polyelectrolyte pendant group, quaternary ammonium, and the negative phosphate groups on DNA strand which is resulting in a planar PT-ssDNA duplex. The planarized polyelectrolyte backbone causes the overlap in the π orbitals on the backbone, increasing the effective conjugation length and causing changes in the optical properties. The augmentation in effective conjugation length of the backbone reduces the HOMO and LUMO energy level difference, and the absorbance spectroscopy shifts towards the red region in visible spectrum. In addition, quenching occurs in fluorescence spectroscopy. In contrast to single-chain DNA, polyelectrolyte conformation is preserved when dsDNA is complexed with the polyelectrolyte because of the stable helical structure of double stranded DNA. In this case, the polyelectrolyte sustains its photophysical characteristics like absorbance maximum, fluorescence emission, etc.

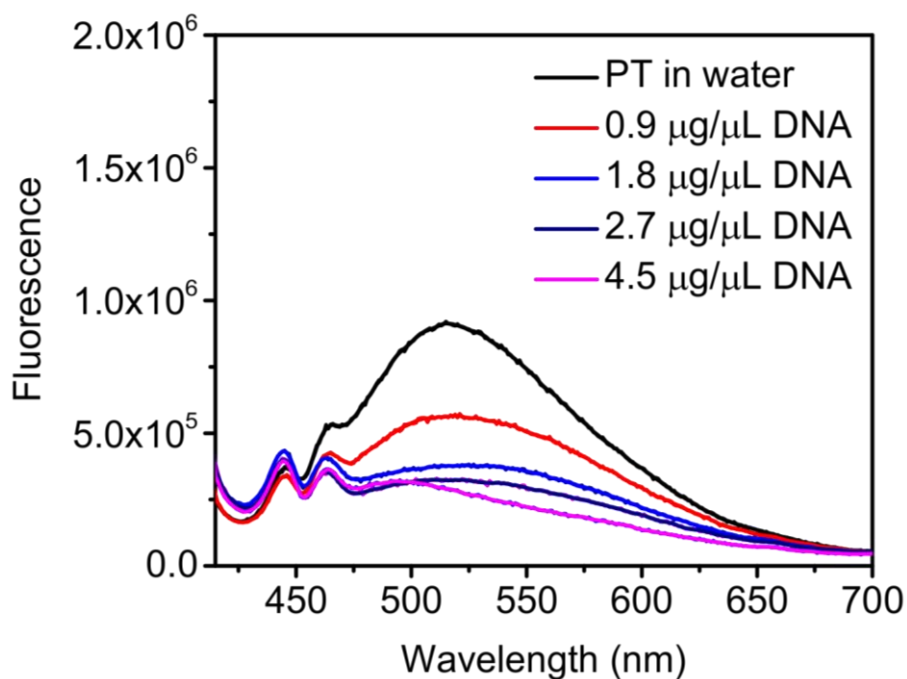


Figure 3.30. Fluorescence titration spectra of PT1 dissolved in water with ssDNA.

Figure 3.30 demonstrates the fluorescence titration analysis of cationic polythiophene derivative with increasing amount of single-stranded DNA in aqueous media. The fluorescence maximum at around 520 nm was swiftly quenched with the addition of ssDNA due to the backbone planarization caused by the electrostatic interaction between positively charged quaternary ammonium side on polythiophene and negatively charged phosphate group on DNA backbones. As a consequence of the backbone planarization, π - π stacking occurs in polythiophene chains which results in non-radiative dissipation from excited electronic state.

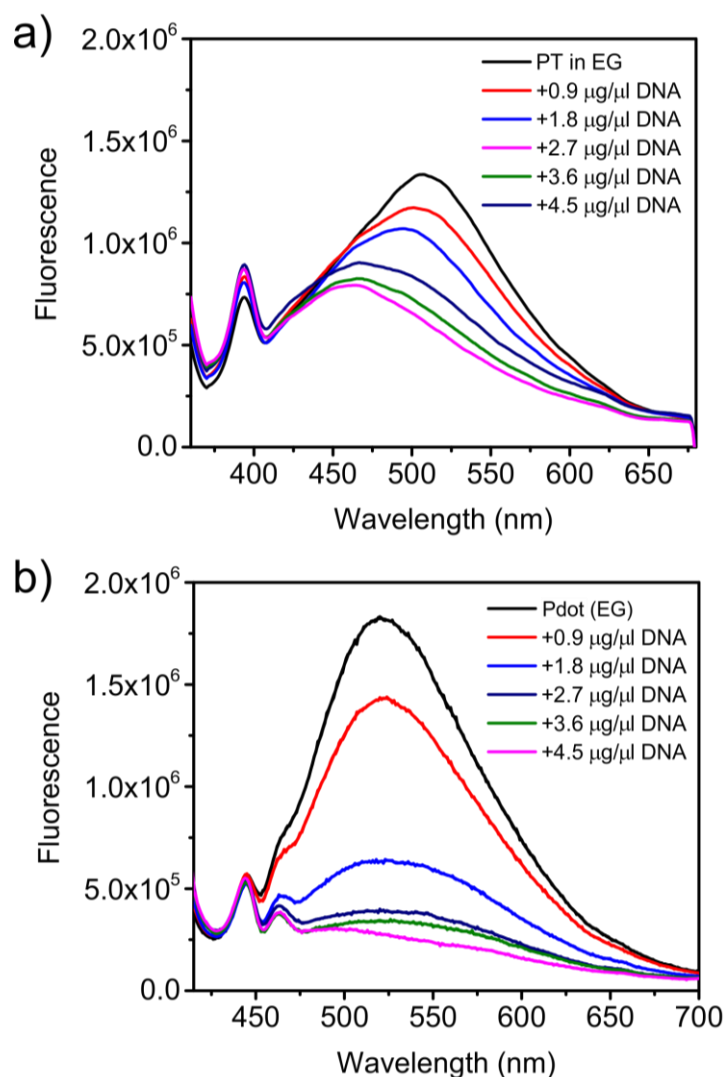


Figure 3.31. Fluorescence titration spectra of a) PT1 dissolved in EG and b) Pdot (EG) with ssDNA.

Fluorescence titration spectra of the polyelectrolyte dissolved in ethylene glycol, CPE(EG), and its Pdot form by the phase separation between ethylene glycol and water is shown in Figure 3.31 a and b, respectively. With the addition of ssDNA into the ethylene glycol solution of CPE, fluorescence maximum at around 510 nm is shifting to the higher energy (approximately 465 nm) in the visible region. The gradual decrease but not complete quenching in fluorescence intensity is attributed to that fluorescent emissive characteristic of polythiophene coil can be still preserved with the strong ion-dipole interaction between CPE and ethylene glycol molecules even presence of anionic DNA structure in the medium. On the other hand, blue shift in the fluorescence maximum can be associated with dominance of the short-length polyelectrolyte chain in ethylene glycol resulted from diminishment of ion-dipole interaction between CPE and EG by

electrostatic interaction between CPE and DNA. This may lead to enhancement of excluded volume in single coil which, therefore, transform more fluorescent specie by eliminating the intra-chain non-radiative decay. However, Pdot solution prepared by nanophase separation behaves like polyelectrolyte chain in aqueous solution and a steep decrease is observed in fluorescence intensity with the addition of counter ion into the Pdot(EG) solution that prove the potential of Pdot as a fluorescent probe for nucleic acid detection.

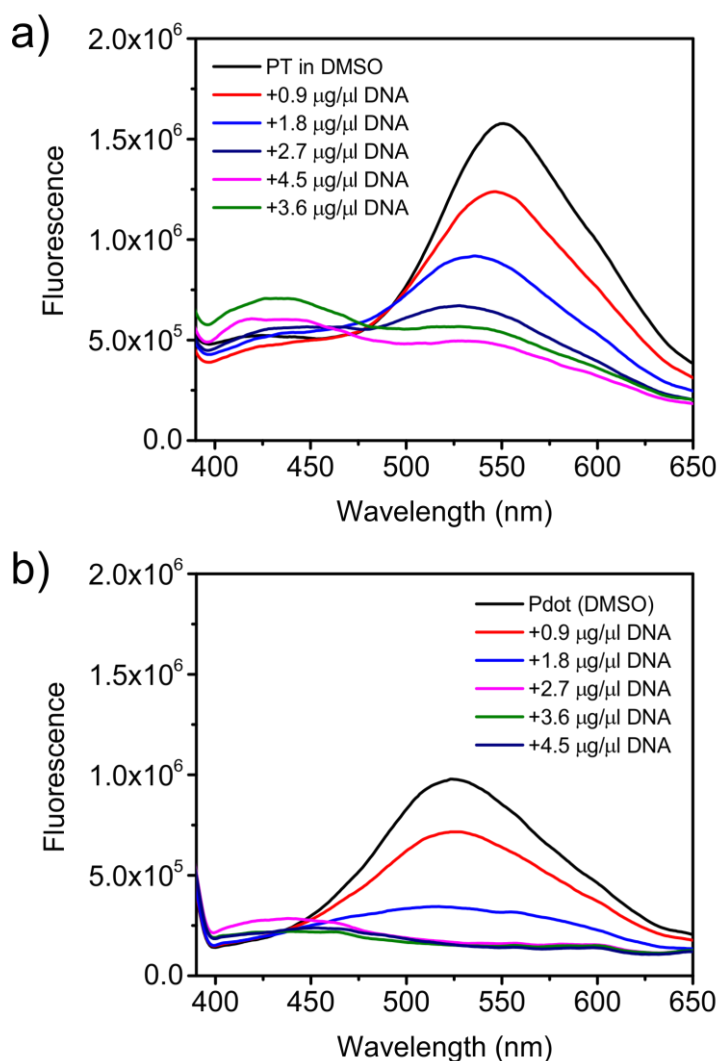


Figure 3.32. Fluorescence titration spectra of a) PT1 dissolved in DMSO and b) Pdot(DMSO) with ssDNA.

The typical fluorescence titration analysis of the polyelectrolyte dissolved in DMSO is represented in Figure 3.32a. Similar to aqueous solution, fluorescence emission of polyelectrolyte is quenched by addition of ssDNA. Dominant characteristic of

electrostatic interaction between counter ions in the solution is observed by quenching the fluorescence emission at 550 nm with a remaining emissive feature at around 430 nm which is corresponding to the short conjugation length of the polyelectrolyte chain. Pdot formed by the phase separation between DMSO and water exhibits similar quenching behavior by DNA addition. A steep and complete quenching in fluorescence emission of Pdot(DMSO) was recorded by fluorescence titration analysis in Figure 3.32b.

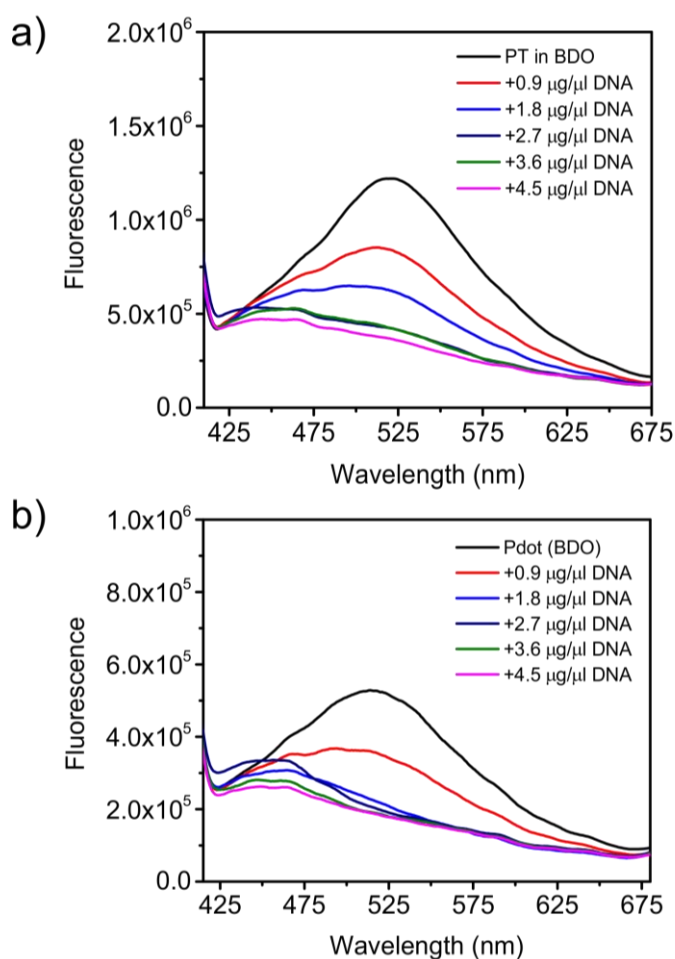


Figure 3.33. Fluorescence titration spectra of a) PT1 dissolved in BDO and b) Pdot(BDO) with ssDNA.

Fluorescence titration spectra of the polyelectrolyte dissolved in 1,4-BDO, CPE(BDO), and its Pdot form by the phase separation between 1,4-butanediol and water is shown in Figure 3.33a and b, respectively. The typical fluorescence quenching at 520 nm with the addition of ssDNA is observed. Beside the fluorescence intensity at around 440 nm is equivalently recorded for both 1,4-BDO solution of CPE and its Pdot form by phase separation Pdot(BDO).

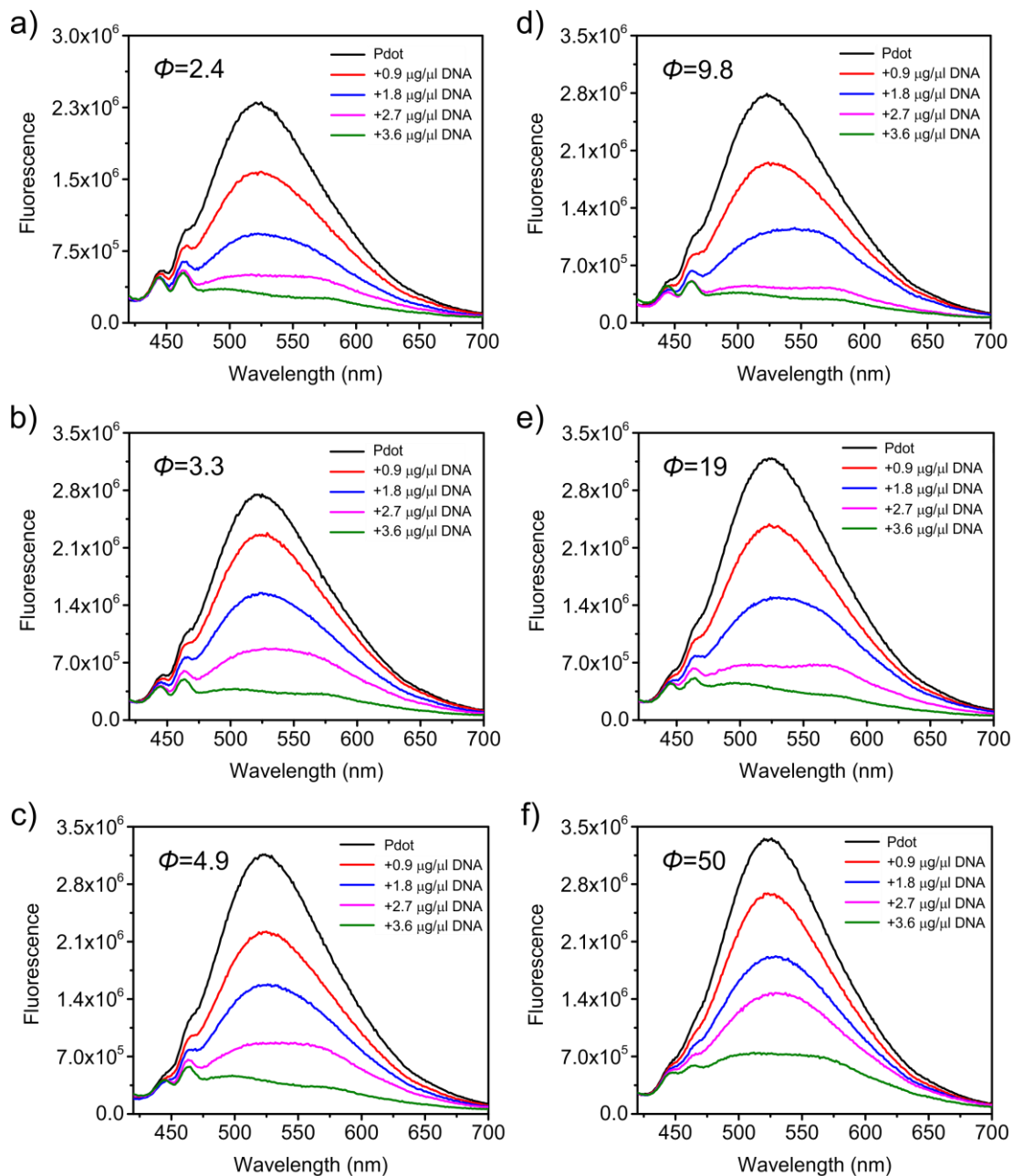


Figure 3.34. Fluorescence titration spectra of Pdot(EG) with increasing ethylene glycol volume fraction (Φ) a) 2.4, b) 3.3, c) 4.9, d) 9.8, e) 19, and f) 50 with ssDNA.

With the addition of single-stranded DNA, Fluorescence titration spectra of Pdot(EG) prepared by nanophase separation between ethylene glycol whose volume fraction is ranging from 2.4 to 50 and water is demonstrated in Figure 3.34. The typical fluorescence quenching is observed in volume fraction ethylene glycol from 2.4 to 19 %. However, significantly noticeable fluorescence conservation of Pdot(EG) with Φ :50 can be seen in Figure 3.34f. Therefore, this ratio indicates the beginning of inverse transition in polyelectrolyte conformation in the medium of ethylene glycol ascendancy.

CHAPTER 4

SELECTIVE DETERMINATION OF HEPATOCELLULAR CARCINOMA CELLS BY POLYMER DOTS

In this chapter, a sub-group of conjugated polyelectrolytes, cationic polythiophene poly(1,4-dimethyl-1-(3-((2,4,5-trimethylthiophen-3-yl)oxy)propyl)piperazin-1-ium bromide) was utilized in the polymer dot (Pdot) form for selective determination of hepatocellular carcinoma (HCC).⁶² The Pdot formation is achieved by nanophase separation method which relies on phase separation between CPE-rich ethylene glycol and CPE-poor water phases. The detailed photophysical, colloidal, and solvation characterization of Pdot prepared by “nanophase separation” was given in Chapter 3. The ultra-small sized Pdots allows a translocation through cellular compartments with a size between 5-10 nm and fluorescence emission provides tracking them in cellular environment.⁶⁷⁻⁷¹ These features make Pdots from cationic polythiophene prepared by nanophase separation able to penetrate nucleus of HCC while accumulating around nucleus in healthy liver cells. Selective labeling of cancer cells in the co-culture medium was also achieved by Pdot. This labelling has a great promise for precise differentiation of cancerous tissue from healthy environment in surgical operations.

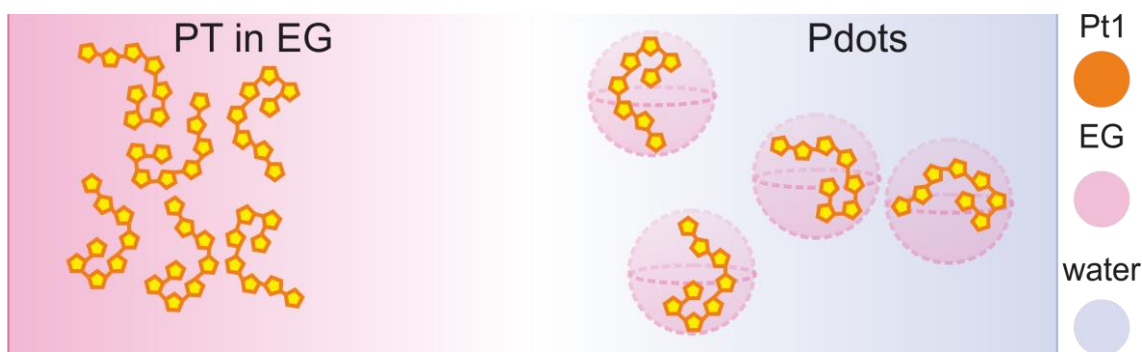


Figure 4.1. Schematic illustration of Pdot formation by “nanophase separation” method based on separation between ethylene glycol (EG) and water.

4.1. Materials and Methods

3-bromo-4-methylthiophene, 3-bromo-1-propanol, 1,4-dimethylpiperazine, 1-methyl-2-pyrrolidinone (NMP), copper bromide (CuBr), sodium bromide (NaBr), magnesium sulfate (MgSO₄), sodium hydrogen sulfate (NaHSO₄), iron(III) chloride (FeCl₃), diethyl ether, toluene, tetrahydrofuran (THF) and chloroform (CHCl₃) were purchased from Sigma-Aldrich. Absorption spectra of polyelectrolyte and Pdot solutions were recorded by Shimadzu UV 2550 spectrophotometer with a quartz cuvette with 0.1 cm optical path length and 1 cm width (Hellma). Steady-state fluorescence spectra of the solutions were recorded with Varian Cary Eclipse spectrophotometer. Fluorescence emission spectra were conducted with excitation at maximum absorption wavelengths. Size analysis was conducted by Malvern Zetasizer Nano ZS instrument. 4.6×10^{-3} mM of the solutions were prepared for size analysis. After size distribution by number was collected, Gauss fitting with $R^2=0.986$ was applied. 4.6×10^{-3} mM of the solutions were utilized for AFM sample preparation. 5 μ L of the solution was dropped onto a freshly cleaned mica (V1 grade) surface then incubated for 45 min. After that the samples were carefully washed with 100 μ L Milli-Q water and dried with steady N₂ flow. AFM analysis was performed with dynamic mode by Nanosurf CoreAFM. Dyn190 Al cantilever with force constant: 48 N/m and resonance frequency: 190 kHz was used for the AFM imaging.

Cell culture: Liver cancer cell line (HuH-7) and primary normal liver cells (THLE-2) were used to evaluate the polymer compartmentalization into the cells. HuH-7 and THLE-2 cell lines were kindly provided Izmir Biomedicine and Genome Center (IBG), Izmir (Turkey). HuH-7 cells were maintained in Dulbecco's modified Eagle's medium (DMEM) containing 10% fetal bovine serum (FBS), 2 mM L-Glutamine, 100 U/ml penicillin, 0.1 mg/ml streptomycin and 1% (v/v) non-essential amino acids solution in a humidified 5% CO₂ incubator at 37°C.⁷² THLE-2 cells were cultured by using BEpiCM (ScienCell) according to manufacturer's instructions.⁷³

Co-culture of HuH-7 and THLE-2 cells: THLE-2 cells were spread at a density of 10×10^4 cells onto each well of an 8-well chamber slide coated with collagen/BSA/fibronectin mixture. After 1-day culture in BEpiCM, the medium was discarded and 10×10^4 HuH-7 cells were spread onto each well. The cells were cultured in DMEM supplemented with 10% FBS.⁷⁴

Confocal Imaging: HuH-7 and THLE-2 cells were plated on glass bottom petri dishes and 8-well chamber slides (Ibidi® plates) for concentration dependent Pdot localization studies. The cells were imaged by spinning disc confocal microscope, Andor Revolution system equipped with Olympus IX71 and Okolab stage incubator system. Both types of the cells were treated with Pdots up to 100 μ M concentration. Coherent Innova diode lasers operating at 488 nm and emission filters of 530/50 nm and 560/30 nm were utilized to obtain emissions of Pdots. Co-cultured cells were stained by using DAPI (4',6-diamidino-2-phenylindole) to visualize the nuclei and observe the co-localization of the Pdots with DAPI. Live-cell imaging studies were performed by imaging of 10 μ M Pdot treated cells. Pdot localized regions were scored by Particle Tracker plug-in on Image-J and the trajectories were graphed by time (80 s).

Image Analysis: The images were analyzed by using Image J program developed by NIH (National Institute of Health). The cellular borders and edges of the nuclei part of the cells were sketched as ROIs (Region of Interests). All ROIs were sketched and saved manually. The fluorescence counts collected from all of the ROIs to assess the Pdot localization of the cancer and normal cells. The histograms of all ROIs were transferred into Microsoft Excel. The total fluorescence counts were the sum of the counts from each pixel. Multiplication of the bins and count/bin values yields the counts value for each ROI. The differences in the fluorescence counts were graphed for HuH-7 and THLE-2 cells as fold changes.

4.2. Results and Discussion

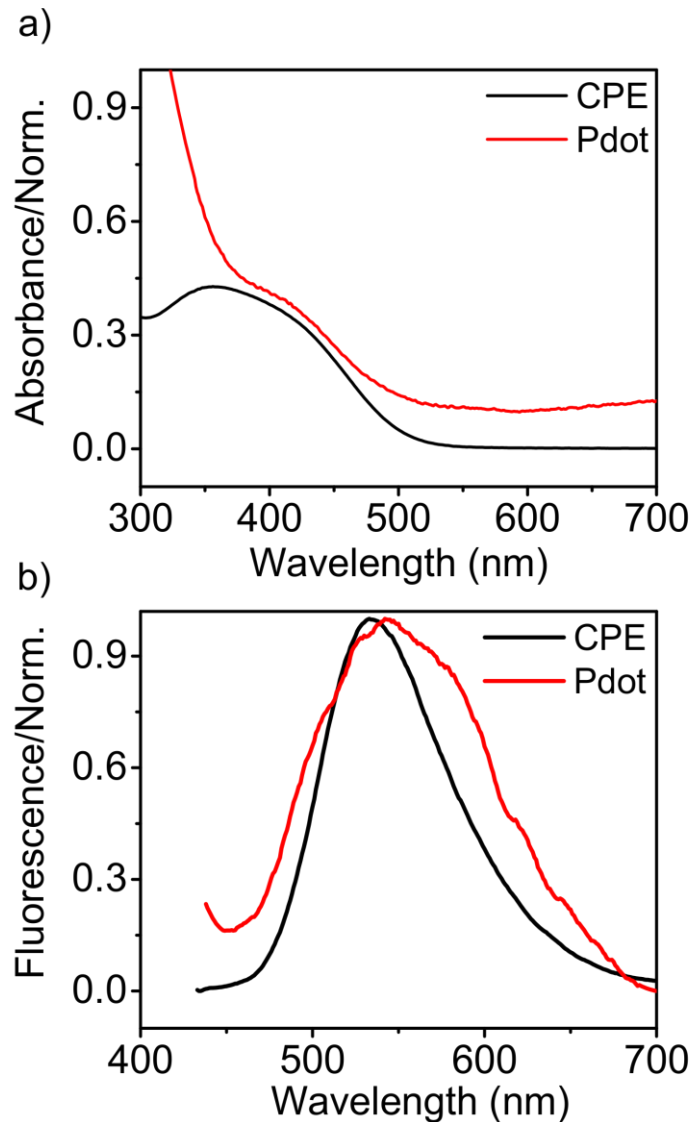


Figure 4.2. a) UV-Vis and b) fluorescence spectra of conjugated PT1 dissolved in ethylene glycol (black trace) and Pdot (red trace).

Figure 4.2 demonstrates the absorption and fluorescence spectra of conjugated polyelectrolyte dissolved in ethylene glycol phase and its Pdot form. The two dominant absorption peaks of CPE found to be 365 nm 415 nm which can be associated to shorter and longer conjugation length in backbone, respectively are shown in Figure 4.2a (black). On the other hand, the absorption spectrum of Pdot in Figure 4.2a (red) exhibits increased level of single chain of random coil characteristic according to the higher energy region of the spectrum. Fluorescence spectra of CPE dissolved in EG and Pdot are shown in Figure 4.2b with maxima at 540 and 550 nm, respectively. (For the further fluorescence

analysis of CPE and Pdot, see Chapter 3). The 10 nm shift in fluorescence maximum and the shoulder at 570 nm in Pdot spectrum can be attributed to increased intrachain π - π interaction. This finding can be also considered as a key that hydrophobic backbone is faced to ethylene glycol phase, therefore the hydrophilic charged group tends to verge through aqueous phase.

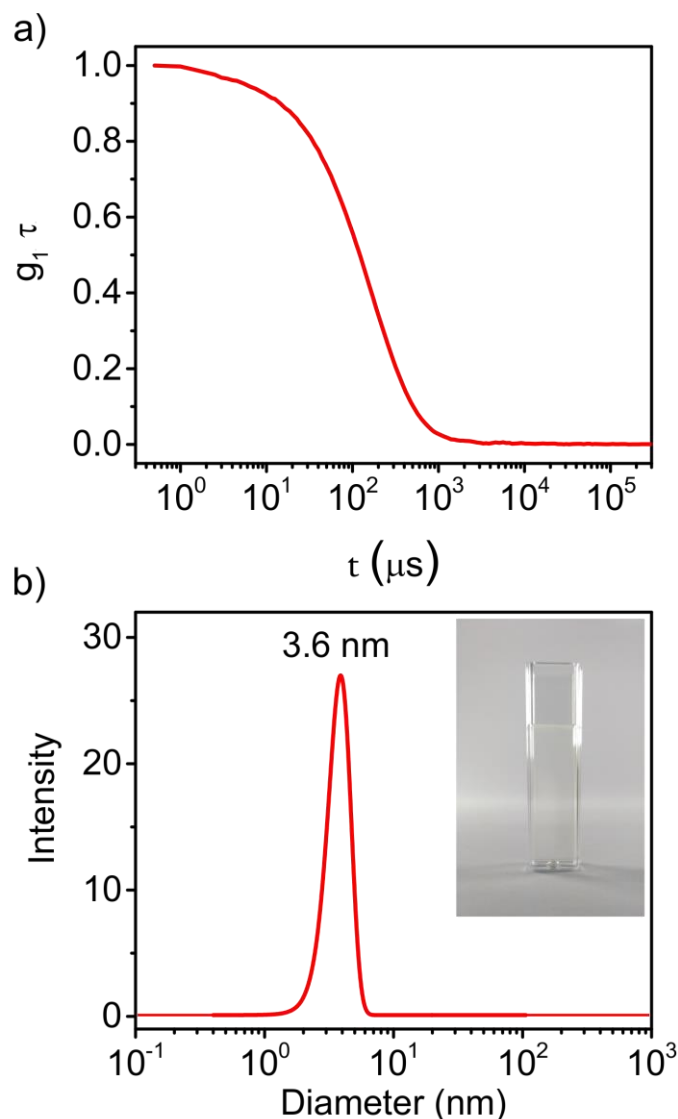


Figure 4.3. a) Autocorrelation function $g_1(\tau)$ and b) size distribution of Pdots (inset photograph shows 60 μM Pdot solution).

Dynamic light scattering (DLS) autocorrelation function $g_1(\tau)$ and size distribution obtained from Zetasizer software were given in Figure 4.3. Diffusion coefficient of Pdots was found to be 4.17 $\mu\text{m}^2/\text{s}$ via Diffusion Coefficient plug-in in the software, therefore, the hydrodynamic diameter of Pdot was calculated as 3.6 nm which is 10 fold smaller than that of CPE dissolved in EG.

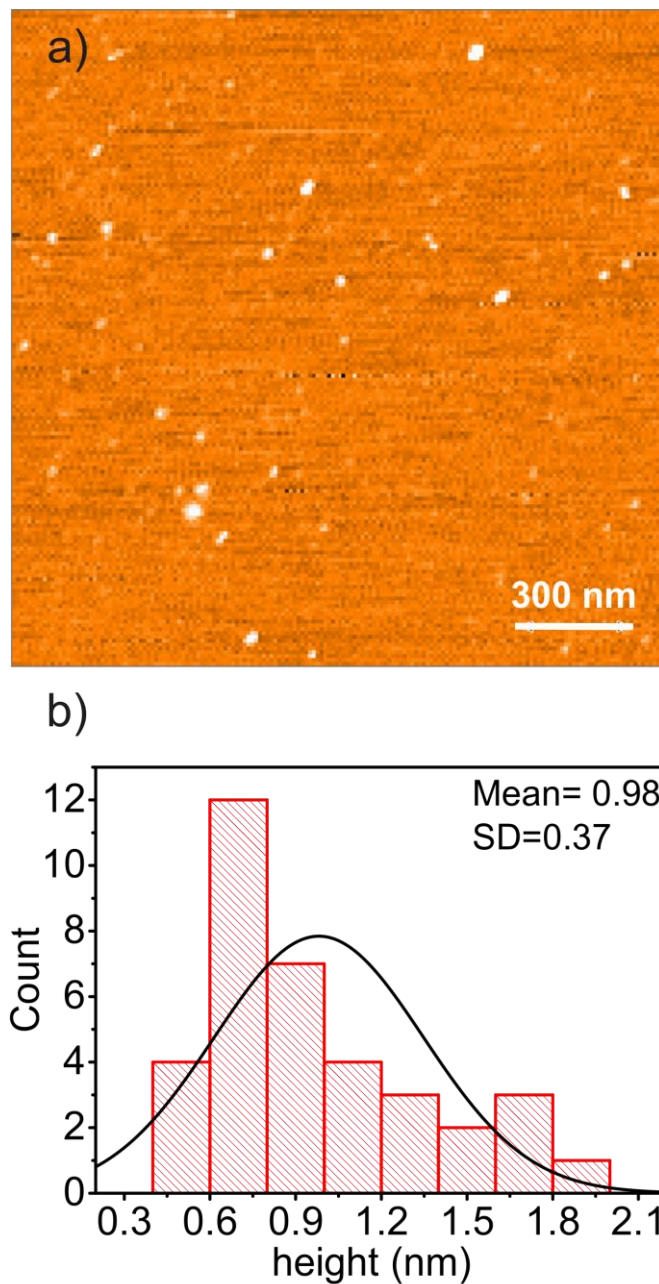


Figure 4.4. a) AFM image of Pdots on mica surface. b) Histogram height distribution of Pdots measured by AFM topography.

For the atomic force microscopy (AFM) analysis in Figure 4.4, 60 μM Pdots, which is the concentration of Pdot in individual well during cell culture experiments, were incubated on freshly cleaved mica surface scanned by dynamic mode. Monodispersed particles were observed in height analysis of Pdots and average height distribution was found to be around 1 nm. The particle size of Pdot acquired from AFM analysis is correlated with a single polyelectrolyte chain. The radius of gyration (R_g) of

a single 20-unit polythiophene chain was theoretically calculated as 2.2 nm. Additionally, the hydrodynamic diameter of Pdot obtained from DLS is slightly larger than that of AFM because of the contribution of solvent molecules to the R_H of polymer chain. Therefore, particle size analysis conducted by DLS and AFM techniques are consistent with each other.⁴³

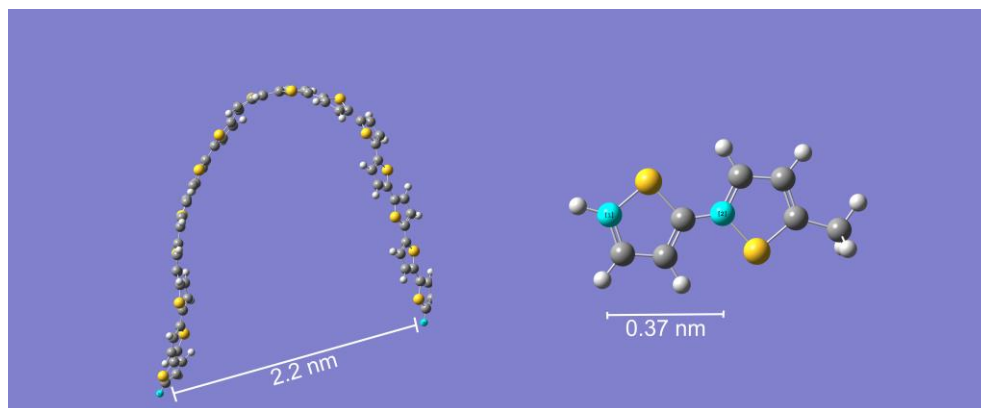


Figure 4.5. Theoretical calculation of end-to-end distance and length of a step.

Chem3D for simple force field and MM2 energy minimization and molecular dynamics were applied to determine the optimum geometry of 20-mer polymer. End-to-end distance and length of step of the optimum geometry were calculated by Gaussian 09 software.

$$\langle R_F \rangle = N^{\nu} \ell$$

where R_F : Flory radius N : The number of linear steps in a random polymer chain, ν : Flory exponent and ℓ : length of a step. For a real single chain containing only the volume exclusion, the proper analogy becomes a self-avoiding walk and Flory exponent $\nu = 3/5$ of a typical excluded volume chain.^{61,75,76}

$$\langle R_F \rangle = (20)^{3/5} 0.37$$

$$\langle R_F \rangle = 2.2 \text{ nm}$$

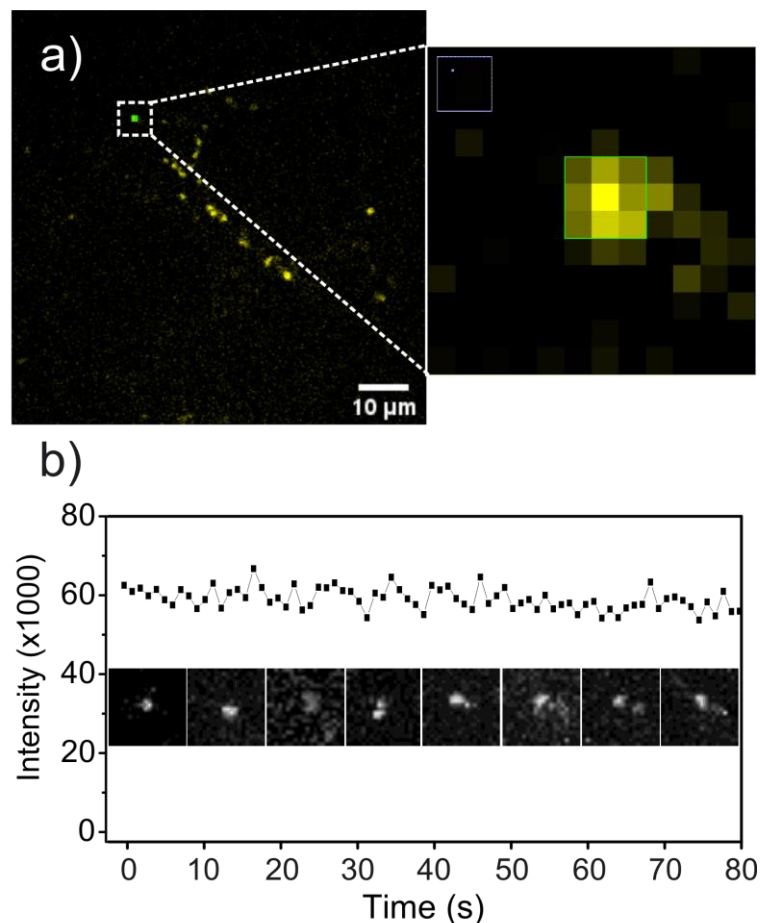


Figure 4.6. a) Confocal microscope image of Pd dots in culture medium (inset image is the 100x magnification of the selected Pd dot). b) Fluorescence intensity variation of single Pd dot tracked in 80 seconds.

In Figure 4.6a, confocal fluorescence microscope image of Pd dots in the cell culture media with the excitation at 488 nm is displayed as an indication that Pd dots preserve their shape and integrity. The fluorescence spotting of Pd dot was illustrated in the inset image of Figure 4.6a and it is observed that the center of Pd dot has a greater fluorescence intensity and the peripheral is faded. These findings show that individual Pd dots have measurable fluorescence intensity and maintain colloidal and optical stability in the cell culture environment without aggregation or quenching. Figure 4.6b demonstrates the fluorescence intensity tracking of single Pd dot within the 80s time period and the average fluorescence intensity during the observation was calculated as 53×10^3 (std. dev. = 2.7×10^3).

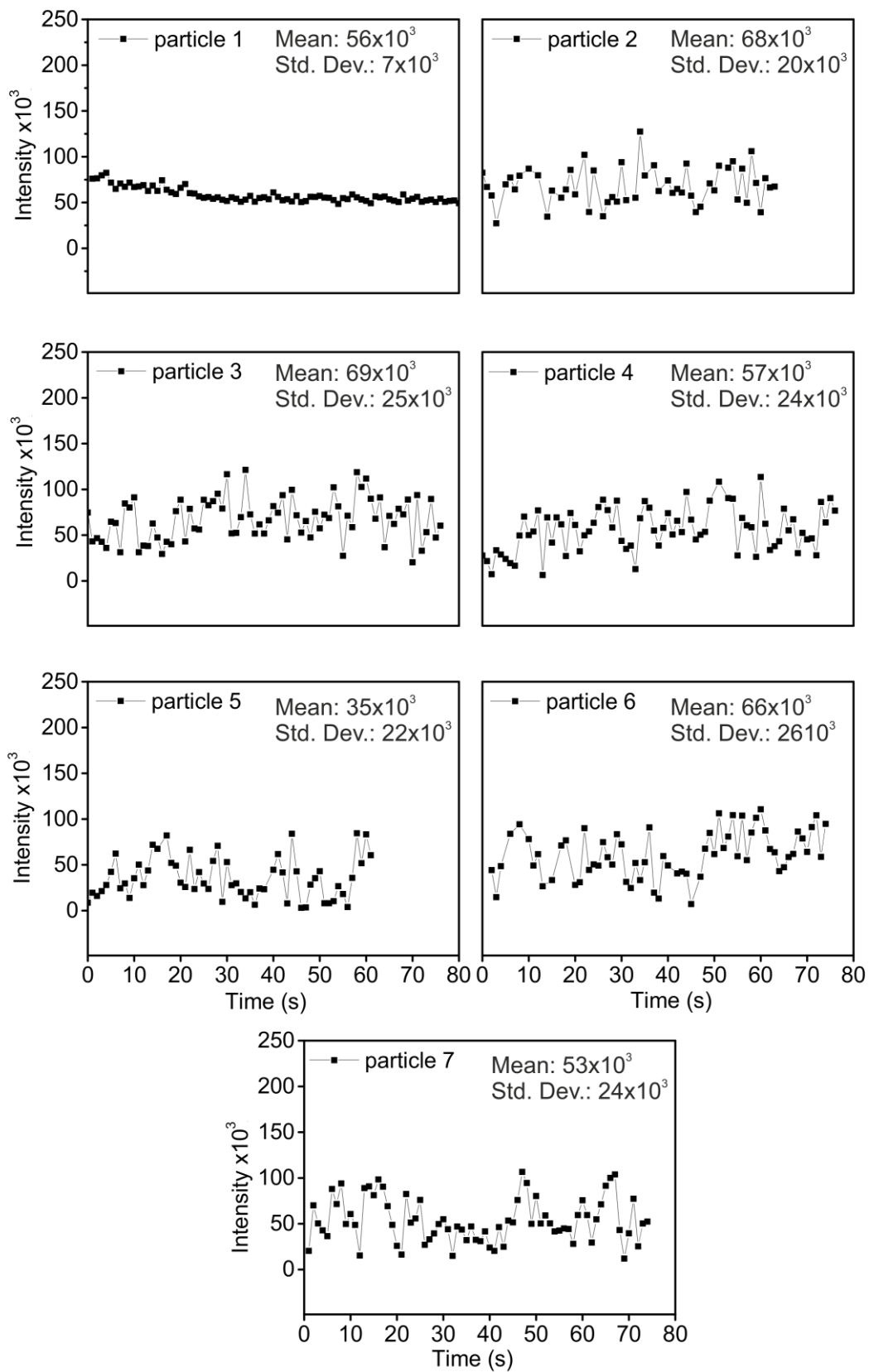


Figure 4.7. Fluorescence intensity variations of 7 individual Pdots.

Figure 4.7 is the fluorescence intensity tracking analysis performed for 7 different Pdots (at 488 nm and 1mW of power at the spot) that exhibits fluorescence mean intensities from 35×10^3 to 69×10^3 and deviations from 7×10^3 to 26×10^3 over the 80s observation period. From the tracking of Pdot, no diminishing fluorescence intensity was observed and the excellent photostability of Pdot under the continuous illumination was assured for utilization of Pdot as a fluorescent probe in cell culture media.

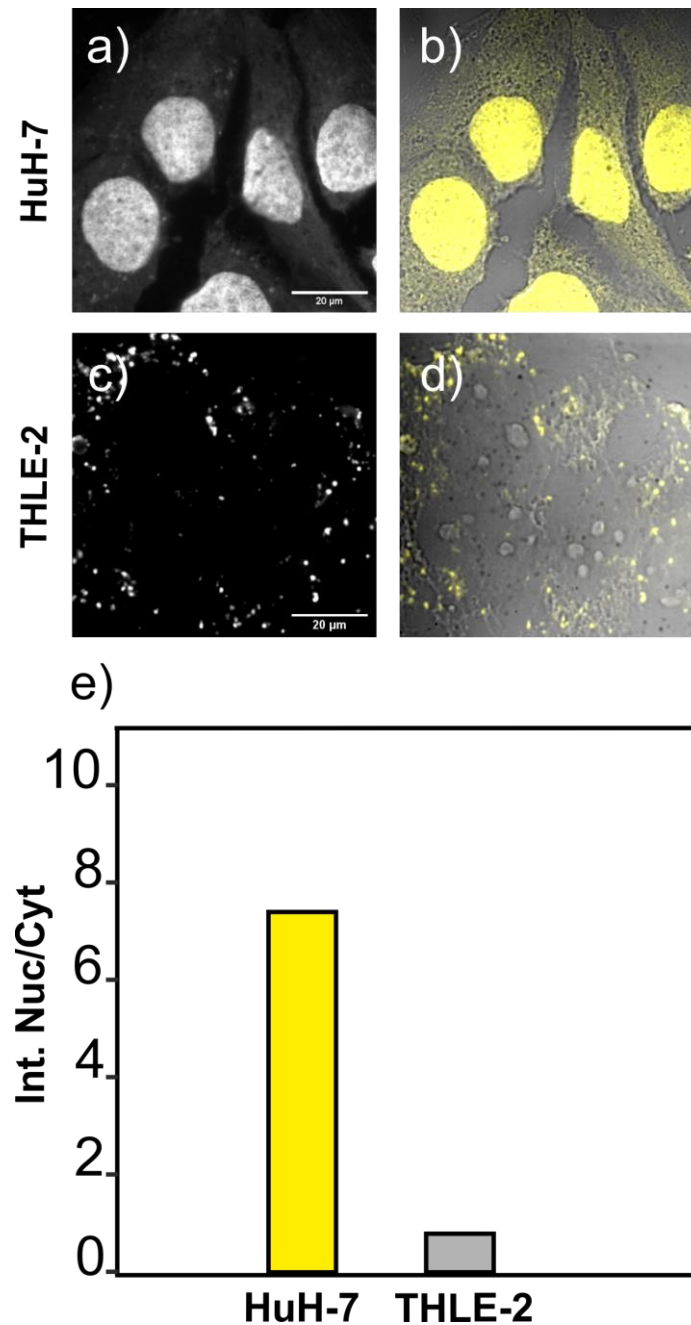


Figure 4.8. a, c) Bright field and b, d) fluorescence confocal images of HuH-7 and THLE-2 cells, respectively. e) Fluorescence intensity ratio of nucleus to cytoplasm from the images shown in Figure 2a-d).

Ultra-small sized Pdots were utilized as a fluorescent probe for cellular imaging of hepatocellular carcinoma (HuH-7) and healthy adult liver epithelial cells (THLE-2). It is revealed that Pdots penetrates into the nucleus of HuH-7 cells (Figure 4.8 a and b) and located in cytoplasm, mostly around nucleus of THLE-2 cells (Figure 4.8 c and d). Moreover, a comparison of fluorescence intensity ratio of nucleus to cytoplasm was demonstrated in Figure 4.8e with a seven folds increase in HuH-7 cells. The selective accumulation of Pdot in the cell nucleus of HuH-7 explicitly ascertains the dependency of Pdot penetration relies on the cell type.

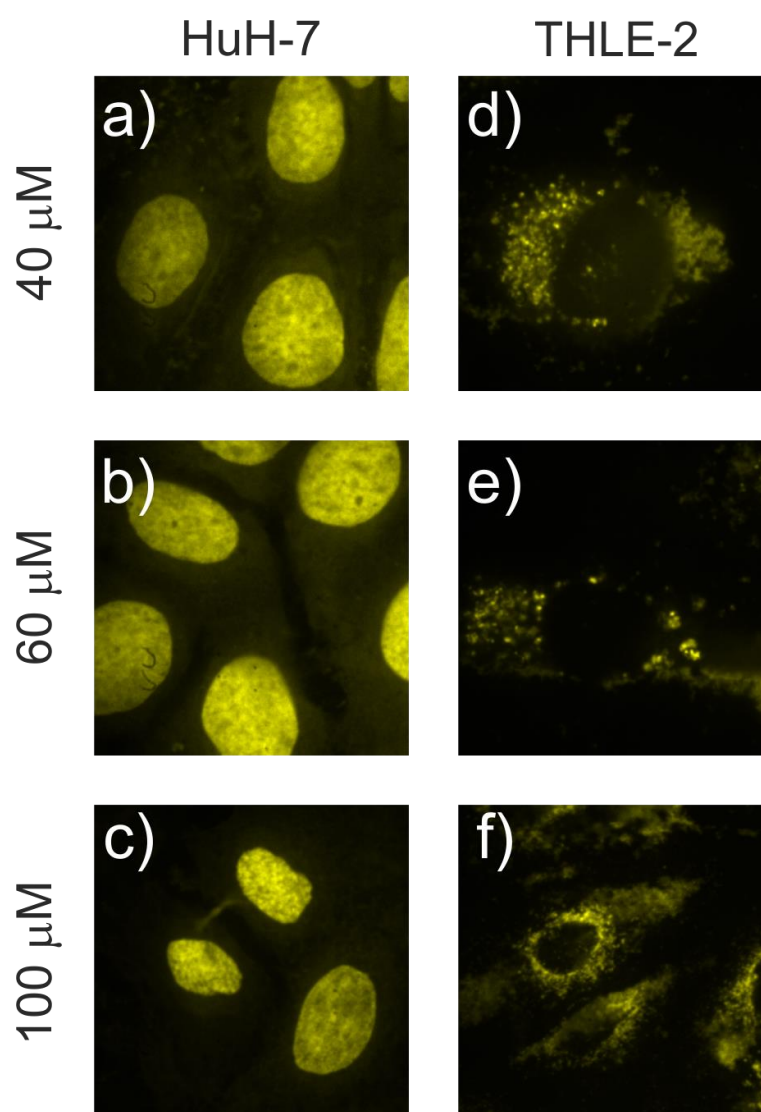


Figure 4.9. Concentration dependent cell imaging study of the 40, 60, and 100 μM Pdots.

A concentration dependent study of Pdots with the extend of 40, 60, and 100 μM was further performed for subcellular imaging of HuH-7 cancer and THLE-2 healthy liver

cells in Figure 4.9. Regardless of the concentration, Pdots was and selectively monitored in nucleus of HuH-7 cells while fluorescence emission of Pdot was collected in cytoplasm, mostly located around cell nucleus of THLE-2. The size of nuclear pore complexes (NPC) which are previously mentioned as to be 5-10 nm provides nuclear penetration of Pdot. the NPC-mediated transformations between cytoplasm and nucleus and nuclear export factor are associated to cancers.^{67,68} Furthermore, the increased and decreased expression of specific proteins can be linked to emerging of cancer that resulting in increased nuclear pore size and distortion of nuclear envelope.^{77,78} Thus, selective nuclear penetration of Pdot to HuH-7 cell is indeed related to the alteration and deformation in cellular structures of cancerous cells.

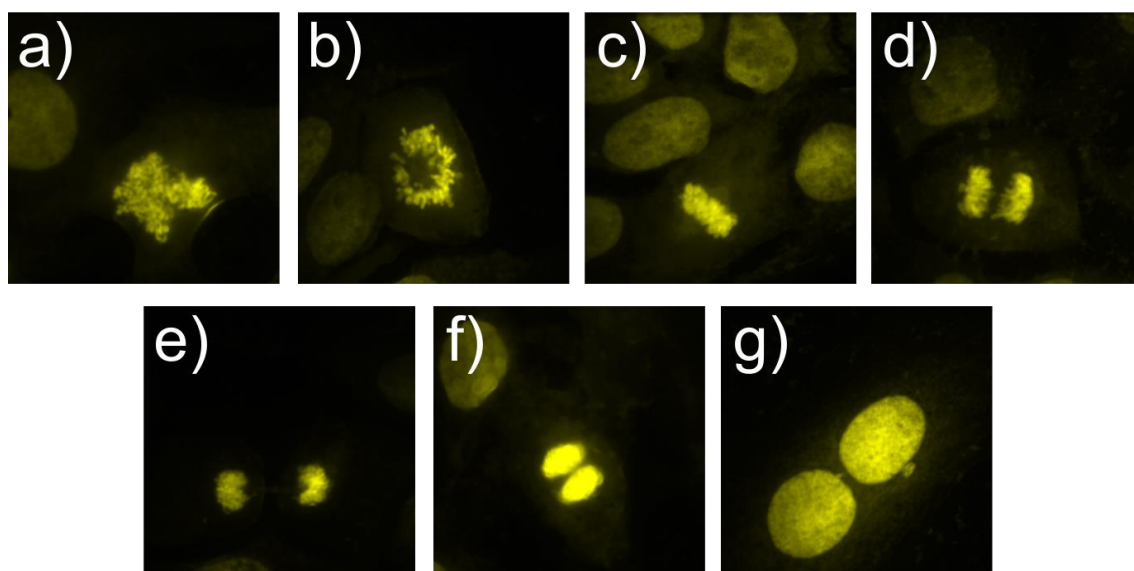


Figure 4.10. The localization of Pdot in the nucleus of HuH-7 with phases of mitotic divisions in the cell cycle; a) prophase, b) pro-metaphase, c) metaphase, d) anaphase, e) telophase, f) cytokinesis, and g) newly divided cells.

Apart from selective penetration of Pdot in cancerous cells, it emits detectable fluorescence signal of nuclei chromosomal staining which resulted from electrostatic interaction between negatively charged DNA and positively charged Pdots. Confocal microscope images of HuH-7 staining by Pdot in sequentially captured mitotic division phases; interphase, metaphase, anaphase, and telophase were given in Figure 4.10. These observations assure utilization of Pdot as a chromosomal or nucleus probe, as well.

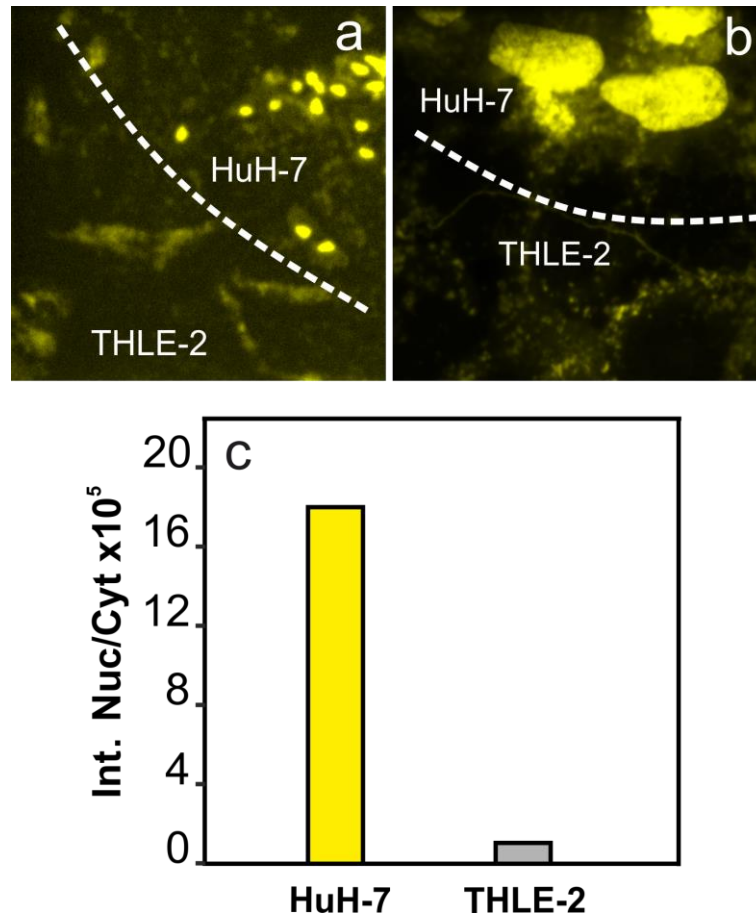


Figure 4.11. Confocal micrographs of co-cultured THLE-2 and HuH-7 cells a) 20X magnification and b) 100X magnification. c) Fluorescence intensity ratio of nucleus to cytoplasm.

Selective nuclear translocation of Pdot in cancerous cells is beneficial for differentiation of cancer cells from the healthy one. Therefore, co-culture study of HuH-7 and THLE-2 cells was performed to further reveal the potential of Pdot prepared by nanophase separation method. Resembling to individual in vitro cell culture experiments of HuH-7 and THLE-2, Pdots were observed to penetrate into nucleus of HuH-7 cells, whereas accumulated in cytoplasm of THLE-2 cells mostly around nucleus in co-culture study. Fluorescence intensity ratios of nucleus to cytoplasm in co-culture staining of Pdot, shown in Figure 4.11c, were found to 18x10⁵ and 1.0x10⁵. The 18 fold greater fluorescence intensity ratio was acquired from the HuH-7 cell nucleus and the lower intensity ratio is belonged to THLE-2 healthy cells in which Pdots mostly located around cell nucleus in cytoplasm. The potential of Pdot for selective staining of hepatocarcinoma cell nucleus in co-culture medium which mimics the tumor microenvironment. Thus, the determination of tumor borders in the liver tissue can be enabled by Pdot. The dotted lines

in Figures 4.11 and 4.12 were drawn as a simulation of the border between cancerous and healthy areas.

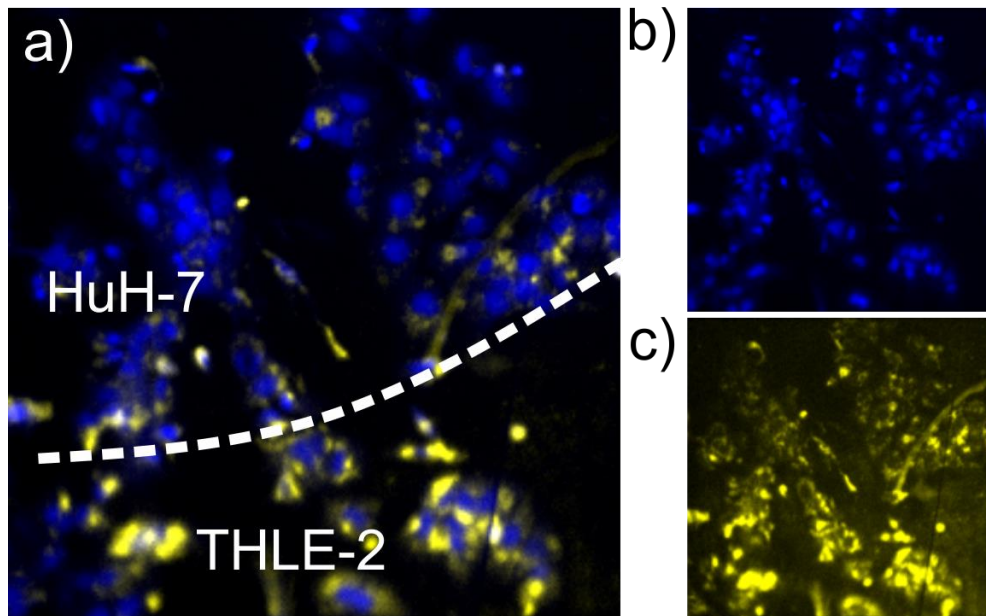


Figure 4.12. a) The images of merged DAPI and Pdot staining co-culture medium. b) only DAPI, and c) only Pdot staining of co-culture.

DAPI staining was also applied to HuH-7 and THLE-2 cells to label the nucleus of the cells. the characteristic of Pdot in HuH-7 cells was observed in confocal images of co-culture medium illustrated in Figure 4.12a (above the dotted line) as it mostly matching with DAPI staining while the below part the image corresponds to the Pdot localization in THLE-2 cells in which yellow emission accumulates in cytoplasm around the nucleus stained by DAPI (blue).

CHAPTER 5

PCR-FREE PROTOCOL FOR NUCLEIC ACID DETECTION BY CONJUGATED POLYELECTROLYTE

5.1. Introduction

The methodology is inspired from the PCR protocol in a much simpler and cost effective way. The PCR-free protocol has first two step of conventional PCR protocol without any requirement of enzyme, deoxyribonucleotide triphosphates (dNTPs). With this method, detection of genetic disease even single nucleotide polymorphism (SNP) was aimed through a simple 4-step protocol and a spectrophotometry.

SNP detection is critical for disease diagnosis, particularly genetic diseases responsible for alteration in single nucleotide. As a result, numerous methods have been developed for identifying SNPs. SNP detection relies on allele discrimination, which can be accomplished through primer extension, hybridization, ligation, and enzymatic cleavage approaches.⁷⁹ These approaches, on the other hand, involve the utilization of a specific enzymes involved-PCR protocol which is labor-intensive, time-consuming, and high cost. As a result of these limitations, PCR-free SNP detection methods have been developed as an alternative.⁸⁰⁻⁸⁶ Despite the fact that these investigations have overcome the PCR methodology, they still require sophisticated steps such as enzymatic reactions,^{81,84} magnetic particle production,^{80,86} and complexed chemical modifications.^{82,83}

For the validation of PCR-free protocol to detect single nucleotide polymorphisms, FMF was chosen as a model genetic disease with SNP. Familial Mediterranean fever (FMF) is an autosomal recessive genetic disease that affects people of Turkish, Jewish, Armenian, and Arab.⁸⁷ Periodic fever, joint and muscular discomfort, a high erythrocyte sedimentation rate, and elevated acute phase reactants such as C-reactive protein and fibrinogen are the most typical symptoms of the condition.⁸⁸ Because comparable symptoms are seen in a variety of other disorders, conventional hospital checks are unlikely to reveal FMF. As a result, the only way to diagnose FMF is through genetic testing.

FMF is currently diagnosed basis of clinical symptoms, ethnicity, family history, and the patient's response to colchicine.⁸⁹ For high or low clinical suspicion and confirmed diagnosis of FMF, the Tel Hashomer criterion, which uses a classification of major and minor criteria, is often utilized.⁹⁰ Periodic fever with peritonitis, synovitis, or pleuritis, as well as amyloidosis, is the major criterion. The minor Tel Hashomer criteria include FMF in first-degree relatives, erythema, and recurring febrile episodes.^{90,91} Molecular genetic testing validates the diagnosis by identifying biallelic pathogenic mutations of the MEFV gene. Even though genetic testing can accurately diagnose FMF, it is prohibitively expensive for all patients. FMF has been linked to more than 70 mutations, the majority of which are found in exon 10. M694V (32%), E148Q (20.6%), V726A (17%), and M680I (14.5%) are the most common mutations.⁹² A study discovered that 8.41 percent of individuals awaiting kidney transplantation had FMF.⁹³ Because kidney transplantation requires proper donor and is a costly procedure, it is critical to lower this rate by detecting FMF early. As a result, using a PCR-free technology based on conjugated polyelectrolyte for population screening, particularly for phenotypic 2 FMF cases, will minimize renal failure rates and the need for transplantation. The suggested methodology has the potential to simplify sample screening before to analysis and to allow rapid separation of healthy individuals prior to the PCR analysis procedure, reducing FMF detection expenses.

The polymerase chain reaction (PCR) is a simple method for amplification of DNA sequences in vitro that has found widespread use in many fields of molecular biology. Dr. Kary Mullis invented and demonstrated PCR as a feasible technology for altering nucleic acid fragments in 1983.⁹⁴⁻⁹⁷ PCR protocol has three main steps for synthesize new DNA strands which are denaturation, annealing, and extension.⁹⁸

Denaturation: It is the temperature-induced separation of the two strands of DNA. The first period takes place at a temperature of 94°C, which is known as the denaturation temperature. Double-stranded DNA (dsDNA) denatures into single-stranded DNA (ssDNA) at this temperature since hydrogen bonds cannot be preserved at temperatures above 80°C.⁹⁹

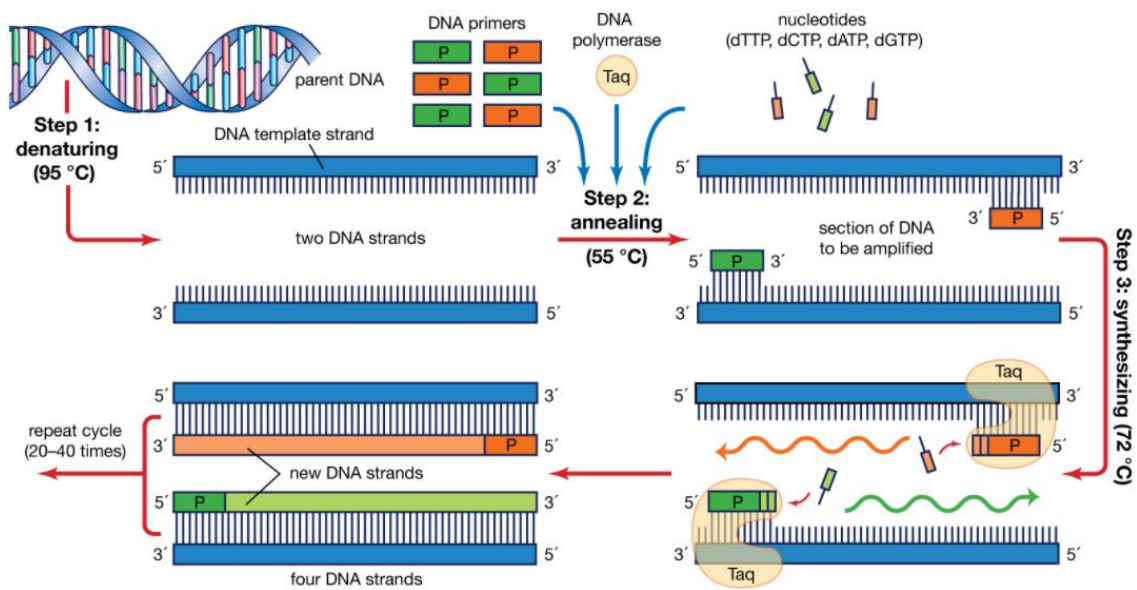


Figure 5.1. Schematic representation of steps involved in polymerase chain reaction (PCR) protocol.¹⁰⁰

Annealing: The second step is hybridization. It is carried out at a temperature generally between 40 and 70°C, called primer hybridization temperature. Decreasing the temperature allows the hydrogen bonds to reform and thus the complementary strands to hybridize. The primers, short single-strand sequences complementary to regions that flank the DNA to be amplified, hybridize more easily than long strand matrix DNA. The higher the hybridization temperature, the more selective the hybridization, the more specific it is.⁹⁹

Extension: The third step is performed at 72°C, often known as elongation temperature. It is the stage in which the complementary strand is synthesized. Heat-stable *Thermus aquaticus* (Taq) DNA polymerase allows for synthesizing and exponentially amplifying the target DNA strand.¹⁰¹

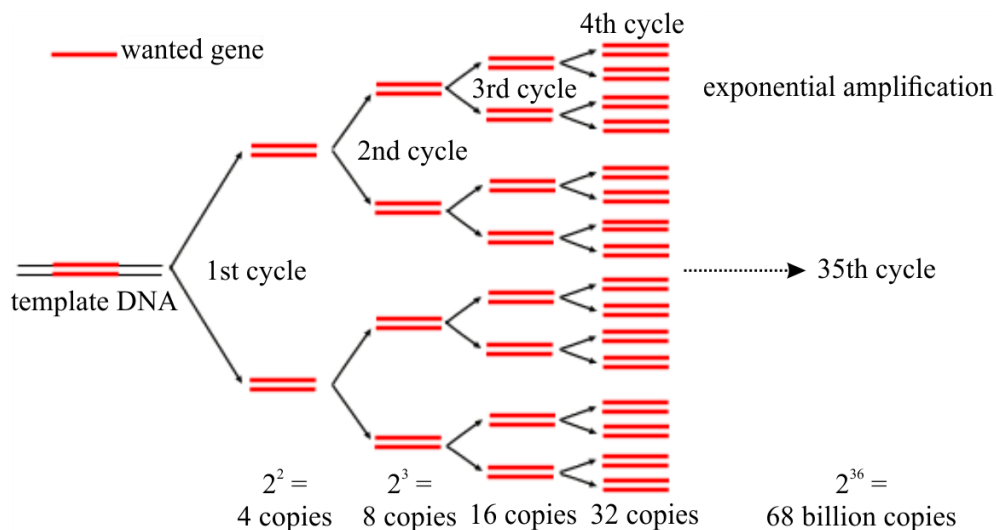


Figure 5.2. Exponential growth of template DNA in each PCR cycle. (Source: Andy Vierstraete, 1999)

Another function of PCR is to quantify DNA addition to amplifying it. Capabilities of conventional PCR have been extended by real-time PCR (qPCR). This approach is used to amplify and quantify a specific segment of a DNA molecule simultaneously. As previously stated, PCR multiplies certain sections of template DNA exponentially (Figure 5.2). However, if the mass of DNA template in the level of picogram or femtogram, the PCR result would not be detected by electrophoresis.¹⁰² qPCR overcomes this sensitivity issue by utilizing a fluorescent molecule called as SYBR Green in between each cycle. SYBR Green binds to double-stranded DNA (not to single-stranded DNA) and it then be fluorescent emitting at 520 nm. Moreover, fluorescence emission of SYBR Green enhances with the amplification of new double-stranded DNA. Therefore, qPCR can detect low amount of DNA template utilizing excellent sensitivity of fluorescence spectroscopy.^{102–104}

5.2. Materials and Method

Chemicals. Copper bromide (CuBr), 3-bromo-4-methylthiophene, 3-bromo-1-propanol, diallylmethylamine, 1-methyl-2-pyrrolidinone (NMP), sodium bromide (NaBr), magnesium sulfate (MgSO₄), sodium hydrogen sulfate (NaHSO₄), iron(III) chloride (FeCl₃), diethyl ether, toluene, tetrahydrofuran (THF) and chloroform (CHCl₃) were purchased from Sigma-Aldrich. Synthesis steps of the polyelectrolyte utilized in this

chapter “Poly(N-allyl-N-methyl-N-(3-((4-methylthiophen-3-yl)oxy)propyl)prop-2-en-1-aminium bromide)” were given in Chapter 2.

Isolation of Human Genome. Anonymized DNA samples from FMF patients, carriers, and healthy individuals were provided by Dokuz Eylul University, Faculty of Medicine, Department of Medical Genetics. The DNA samples were isolated with respect to the manual of High Pure PCR Template isolation (Roche, USA) kit, absorbance of samples at 260 and 280 nm were measured by Nanodrop (Thermo, USA) to ascertain the DNA concentration and its purity in which the concentration of samples was found to be between 10 ng/L and 70 ng/L (the listed concentrations can be found in Appendix A). The NCBI/Ensembl databases and Blast/UCSC in-silico-PCR softwares were used for determining the sequences of wild - mutant type primers and for calculating the specificity, respectively. All genomic DNAs were stored in a buffer system containing Tris-HCl and EDTA at 80°C.

Detection of M694V SNP with using Real Time PCR. The DNA samples were analyzed using the LightCycler FastStart DNA Master Hyb Probe (Roche, USA) kit specific to the LIGHTSNIP FMF M694V (rs61752717) gene and SNPs. The detailed experimental procedures can be found in Appendix A.

Primers and Probes Design. MEFV gene and rs61752717 (known as M694V which is a single nucleotide polymorphism in MEFV gene) sequences were obtained from NCBI (<http://www.ncbi.nlm.nih.gov/>) and the "dbSNP Short Genetic Variations" database, respectively. The primers and probe for the M694V were designed by Light-Cycler Probe Design Software 2.0 (Roche).

Sequences of primers and probe:⁹

F: 5'-TCATCATTATCACCACCCAGTAGCC-3'

R: 3'-GAGCCTGCAAGACATCC-5'

Sprob:5'-Fluorescein-SPC-GGCTACTGGGTGGTGATAATGATGA-
Phosphate-3'

Hybridization Protocol. Wild and mutant type sequences indicated below were added to the isolated genomic DNAs of FMF patients, carriers, and healthy individuals for hybridization.⁹

Wild type primer: TGATAATG**A**TGAAGGAAAATGAGTACCAG

Mutant type primer: TGATAATG**G**TGAAGGAAAATGAGTACCAG

Denaturation of the human genomes (HG) was performed heating the HG-primer mixture to 95°C for 1 hour. In the 2nd step, the mixtures were incubated for 2 hours at

61°C and 62°C which are melting temperatures of wild and mutant type primers, respectively in order to hybridize primers to the HG in separate micro centrifuge tubes. Following to hybridization step, the mixtures were centrifuged for 30 minutes at 10000 rpm for collecting human genome along with complementary primer in the pellet and for collecting non-complementary primer in the supernatants with respect to the nature of the HG sample.

Fluorescence Analysis of DNA Solutions. Varioskan Flash microplate reader (Thermo Scientific) with 384 black well plate was utilized in steady-state fluorescence spectroscopy analysis of DNA-primer mixtures (step 4). 10 μL of 1.85×10^{-3} M CPE solutions were diluted to 20 μL by the addition of Tris-EDTA buffer (TE, pH:8.0). The solutions acquired at the end of step 3 were added to CPE solution and gently pipetted before fluorescence analysis with an excitation at 400 nm, absorption maximum of cationic conjugated polythiophene.

5.3. Results and Discussion

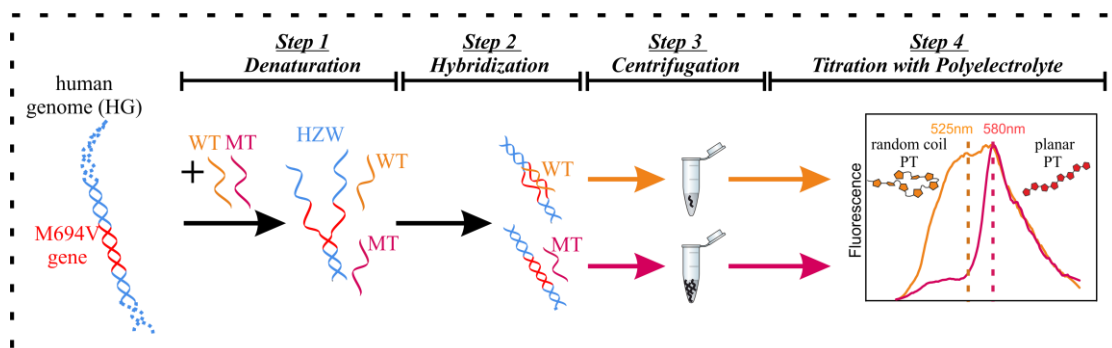


Figure 5.3. Schematic of four-stepped PCR-free assay based on conjugated polyelectrolyte. HG: human genome, WT: wild type primer, MT: mutant type primer, HZW: homozygous wild type human genome, HZM: homozygous mutant type human genome, HTZ: heterozygous human genome.⁹

Figure 5.3 illustrates the 4-stepped PCR-free protocol based on conjugated polythiophene. 30 μL isolated genomic DNA solution is split into two equal-volume solutions, Sol1 and Sol2, in which denaturation of DNA template, hybridization of wild (WT) and mutant type (MT) primers, respectively, and centrifugation steps of conjugated

polyelectrolyte based PCR-free protocol. The pseudo WT and MT primers are introduced to the Sol1 and Sol2, respectively, to be prior to denaturation and hybridization processes. After denaturation of genomic DNA at 95°C (step 1), the solutions are incubated at melting temperature of primers (step 2), then centrifugated for separation of unhybridized residual primers in supernatant (step 3). The unhybridized residual WT primer and unhybridized residual MT primers are hereafter called as rWT and rMT, respectively, and separated after centrifugation for the fluorescence titration of conjugated polyelectrolyte (step 4). The amount of rWT and rMT in supernatant solutions varies depending on whether they are complementary to target genomic DNA type which can be either homozygous wild (HZW, healthy individual), homozygous mutant (HZM, FMF patient), or heterozygous (HTZ, carrier). In titration step, CPE undergoes complexation with rWT or rMT single-stranded primers by the electrostatic interaction between cationic sides on CPE and negative sides on DNA, therefore transition in fluorescence emission maximum of CPE from 525 to 580 nm, as mentioned earlier in Chapter 1. The intensity of fluorescence transition is reported proportional to the quantity of unhybridized pseudo primers that allows for SNP identification without PCR amplification. In this chapter, a simple logic shown below is applied on the comparison of fluorescence intensities at 525 and 580 nm for differentiation of target gene by determining if unhybridized residual primer is wild (rWT) or mutant (rMT).

1- If $rWT I_{525/580} > rMT I_{525/580}$ then subject is healthy (HZW)

2- If $rWT I_{525/580} = rMT I_{525/580}$ then subject is unhealthy (HZM or HTZ).⁹

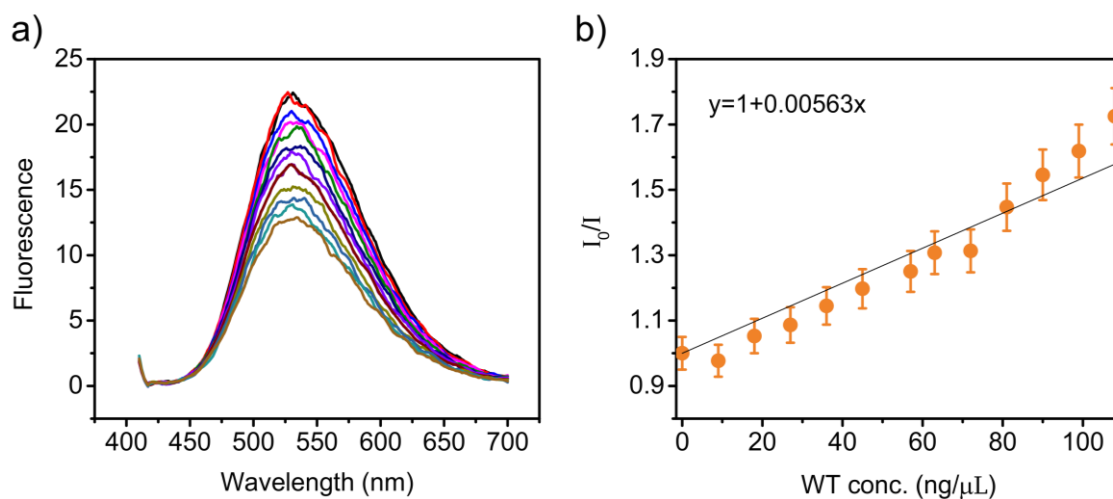


Figure 5.4. a) Fluorescence analysis of PT2 (1.8 mM of 200 μ L) quenched by wild type primer in the concentration between 0 (top) to 108 ng/ μ L. b) Stern-Volmer plot of Figure 5.4a.

Fluorescence titration analysis of CPE with the addition of WT primer in the concentration range from 0 to 108 ng/ μ L which covers the concentration of clinic samples, is shown in Figure 5.4. The Stern-Volmer plot (I_0/I) in Figure 5.4b was plotted using emission intensities at maximum wavelength from fluorescence titration curves in Figure 5.4a. As the amount of primer increases, fluorescence emission of CPE linearly decreases by quenching effect of WT primer. The linearity of Stern-Volmer plot was revealed by the linear least square regression between increasing WT concentrations and I_0/I using Origin 9 software and R^2 and slope of linear regression was found to be 0.997 and 0.00563, respectively. The R-square of the resulting linear line was found to be 0.997, with a slope of 0.00563. This linear correlation between emission intensity and the concentration of WT primer makes rWT and rMT primers detectable by monitoring fluorescence intensities of conjugated polyelectrolyte.

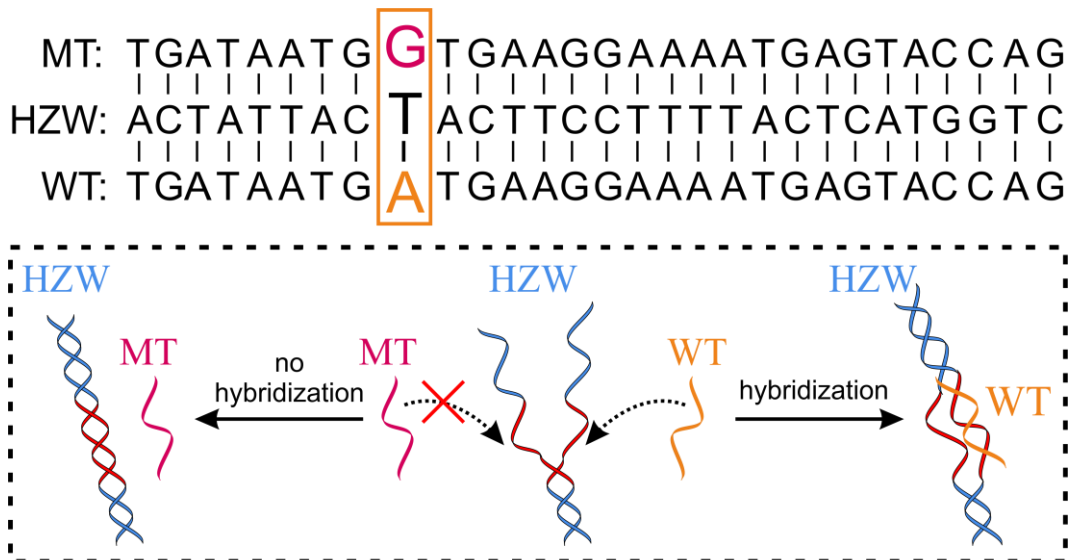


Figure 5.5. Schematic illustration of hybridization step for HZW samples.

Figure 5.5 depicts the WT and MT sequences as well as the possible hybridization process to homozygous wild (HZW) genomic DNA. A typical fluorescence intensity profile of CPE after the protocol was conducted on HZW samples is demonstrated in Figure 5.6 in which rWT-CPE and rMT-CPE complexes are indicated in orange and pink, respectively. Since the WT primer is complementary to MEFV gene region in HZW samples, it hybridizes to the genomic DNA of healthy individuals, therefore, the rWT solution does not have quenching effect on CPE fluorescence emission at 525 nm because of trace amount of unhybridized residual primer in supernatant. However, MT primer does not affectively bound to HZW sample, it is because non-complementary to MEFV gene region of healthy subjects, thus it will exist in supernatant solution as unhybridized residual MT primer (rMT) with as significant amount to quench the fluorescence of CPE at 525.

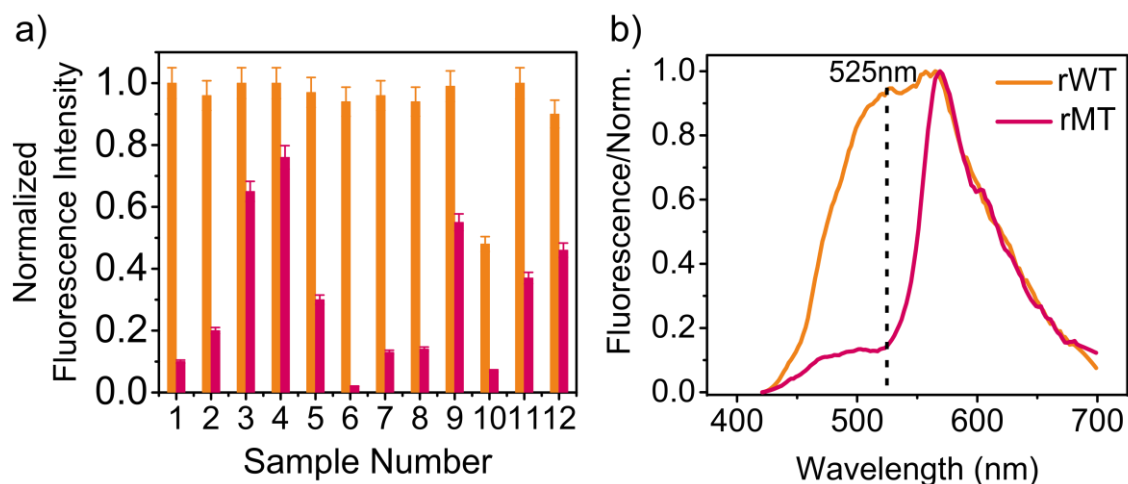


Figure 5.6. a) Fluorescence intensity profile at 525 nm of rWT-CPE (orange) and rMT-CPE (pink) complexes of 12 HZW healthy samples and b) typical fluorescence spectra of collected from sample 8 (0.9 mM of 20 μ L of CPE was used in fluorescence analyses).

The normalized fluorescence intensities of the CPE treated with rWT solutions is approximately three fold greater than those of the rMT solution as shown in Figure 5.6a. Twelve genomic DNA samples studied for the validation of CPE-based PCR-free protocol exhibits similar characteristic for each sample. These intensity profiles of rWT-CPE and rMT-CPE are described as healthy individuals by the proposed logic which identifies the twelve samples of the twenty six as homozygous wild type (HZW, healthy). The fluorescence spectra of rWT-CPE and rMT-CPE in the conformations of twisted (orange) and planar (pink) are respectively indicated in Figure 5.6b. The greater amount of single-stranded DNA fragment (which is rMT in this case of HZW analysis) shifts the absorption spectrum of CPE to lower energy because of planarized form of rMT-CPE complex thus, the fluorescence spectrum of the complex is also shifted to 580 nm. However, this concrete transition can be seen at lower CPE concentration (<1.2 mM) otherwise it is hidden in the spectrum of higher CPE concentration (Figure 5.4a).

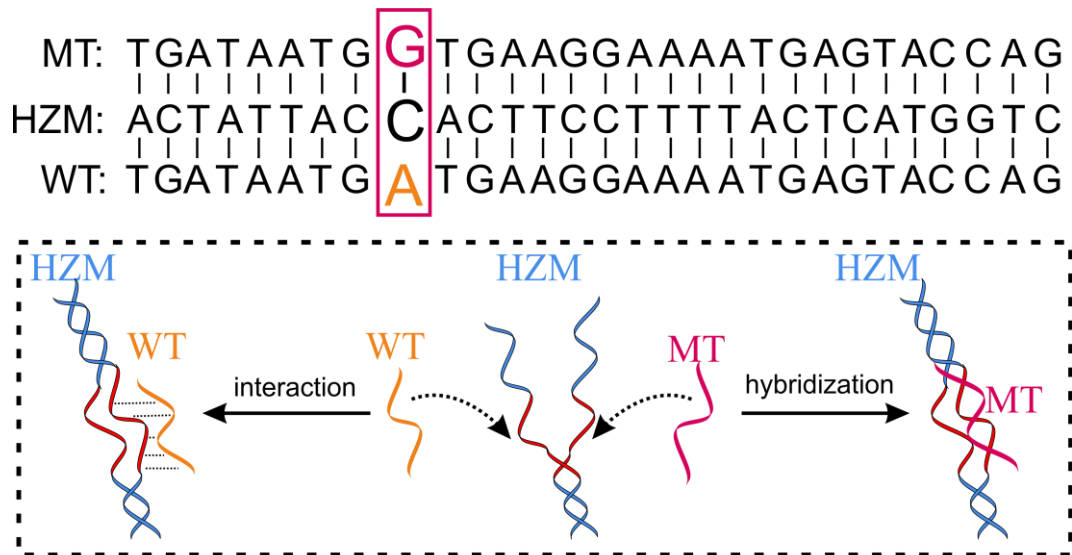


Figure 5.7. Schematic illustration of hybridization step for HZM samples.

Figure 5.7 demonstrates the WT and MT sequences acquired from “Genetic Variations” database as well as potential mechanisms can occur between HZM and primers (WT and MT). The fluorescence intensity profile of 14 HZM (FMF patients) and HTZ (FMF carriers) samples are illustrated in Figure 5.8. The fluorescence intensity of rMT-CPE complex at 525 nm for fluorescence analysis of HZM and HTZ samples is significantly greater than that of HZW samples which indicates hybridization of mutant type primer (complementary of homozygous mutant genomic DNA) to HZM.

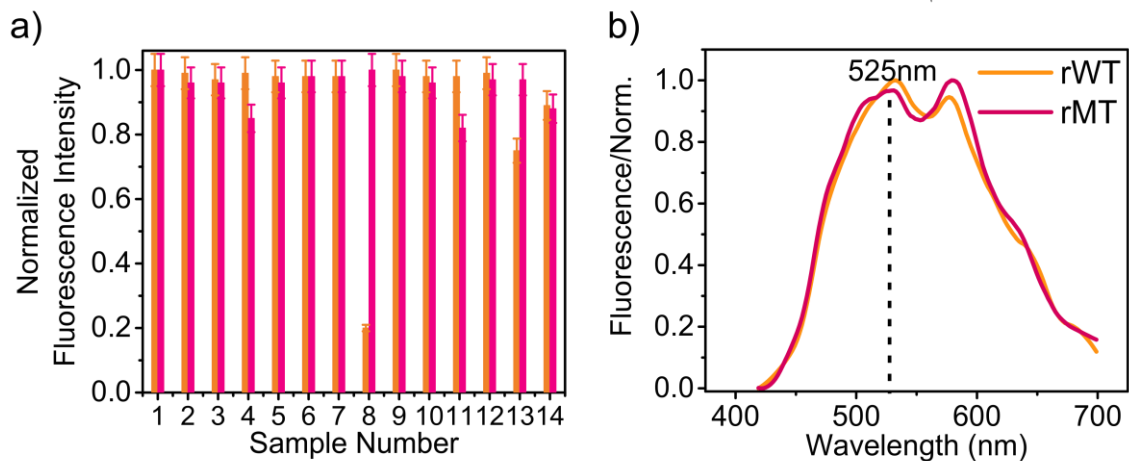


Figure 5.8. a) Fluorescence intensity profile at 525 nm of rWT-CPE (orange) and rMT-CPE (pink) complexes of 14 HZM and HTZ samples and b) typical fluorescence spectra of collected from sample 5 (0.9 mM of 20 μ L of PT2 was used in fluorescence analyses).

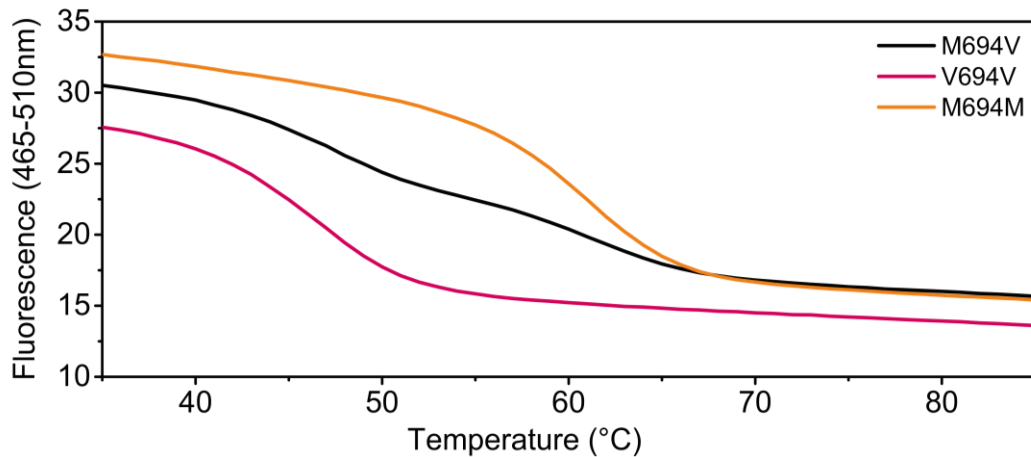


Figure 5.9. Melt curves from qPCR analysis of the MEFV gene variations; M694V-heterozygous, V694V-homozygous mutant and M694M-homozygous wild.

Figure 5.9 demonstrate the melting curve of each MEFV gene variation and fluorescence signal explicitly declines with an increasing temperature which indicates the quenching of the SimpleProbe signal. When compared to the other samples, the twelve homozygous wild samples out of 26 show a melting transition at a slightly higher temperature (orange curve). Figure 5.10 illustrates the first negative derivative of the fluorescence signal, which reveals a melting temperature of 61°C for M694M homozygous wild type mice (HZW). The remaining 14 samples have single step melting transitions at 55°C (7 patients, V694V) and double step transitions at 55°C and 61°C, respectively (7 carriers, M694V). When compared to homozygous mutant samples, homozygous wild samples had a greater melting temperature due to the perfect match between M694M sequence and probe (lower melting peak reflecting the mismatches in sequence between V694V sequence and probe). The qPCR results show that homozygous (12:HZW) and homozygous mutant + heterozygous (14:HZM+HZT) samples match precisely with the CPE-based PCR-free protocol. This finding confirms that the assay is capable of accurately distinguishing healthy people from patients and carriers. Furthermore, HZW (healthy) and HZM+HTZ (patients + carriers) distinction is found to be as accurate as PCR.

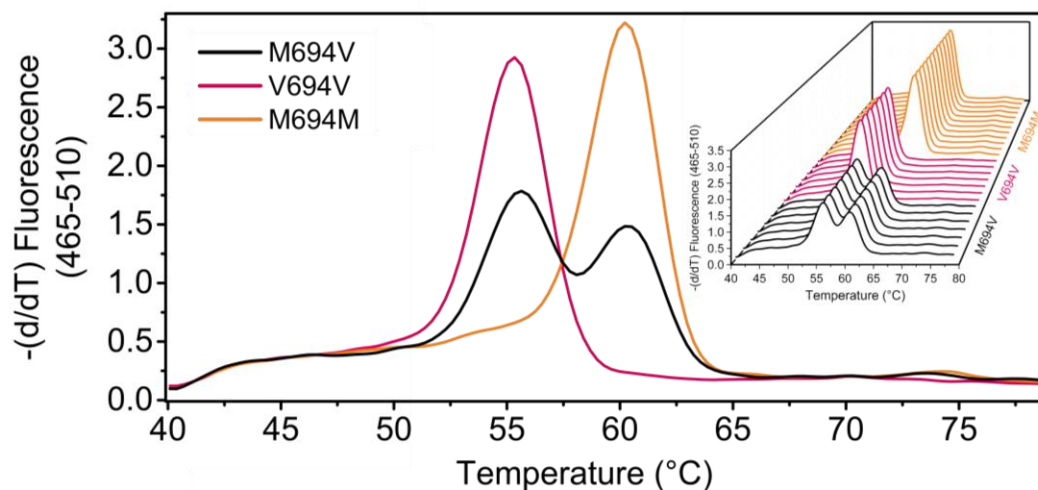
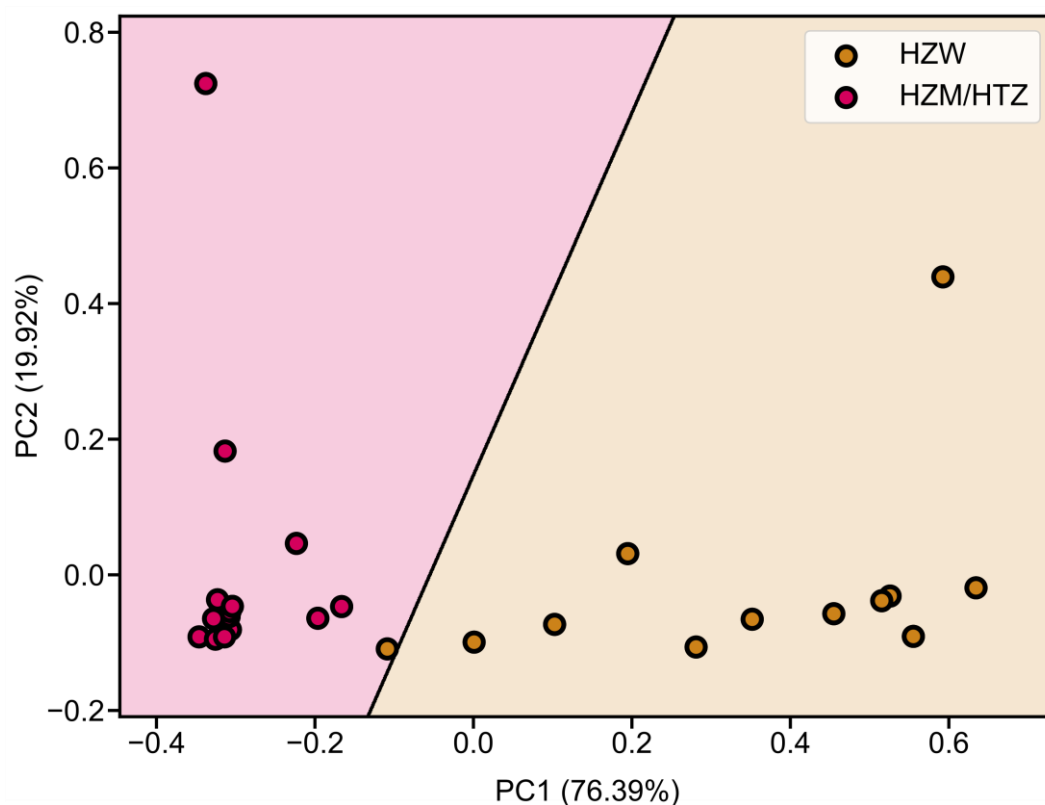


Figure 5.10. First derivatives of melting curves of gene variations (M694V, V694V and M694M). Inset figure represents the data of total 26 genomic DNA studied in this chapter.

To standardize the conjugated polyelectrolyte based PCR-free method, the fluorescence intensities of rWT-CPE and rMT-CPE complexes in the analysis of HZW, HZM, and HTZ was furthermore investigated by data analysis methodologies. The data analysis was performed in Python 3 using scikit-learn library.¹⁰⁵ Principal component analysis (PCA) was first used with 4 variables (the two emission wavelength for both rWT-CPE and rMT-CPE) for genomic DNA sample to lower the number of dimensions by maximizing variance. The total explained variance of the first two principal components (PC1 and PC2) was found to be 96.31 percent, with individual explained variances for PC1 and PC2 of 76.39 percent and 19.92 percent, respectively. The 2D scores plot alone gave a distinct separation of homozygous wild and homozygous mutant-heterozygous samples, as well as a depiction of these four variables. Furthermore, Support Vector Machine (SVM) classification was applied to PCA scores (just PC1 and PC2) as a supervised classification approach, yielding an optimal linear decision boundary. Figure 5.9 depicts the combined results of the PCA and SVM techniques. Only one sample belonging to homozygous wild was misclassified by a narrow margin out of 26 samples (12 homozygous wild, 14 heterozygous mutant), achieving a total classification accuracy of 96 percent. Since the mutant class is known as the positive class, the model's sensitivity and specificity were calculated to be 100 and 92 percent, respectively. The first PC which is the main axis for classification, separates the HZW samples (right side of SVM boundary) from the HZM-HTZ samples (left side of SVM boundary) except single HZW sample seen in Figure 5.9.



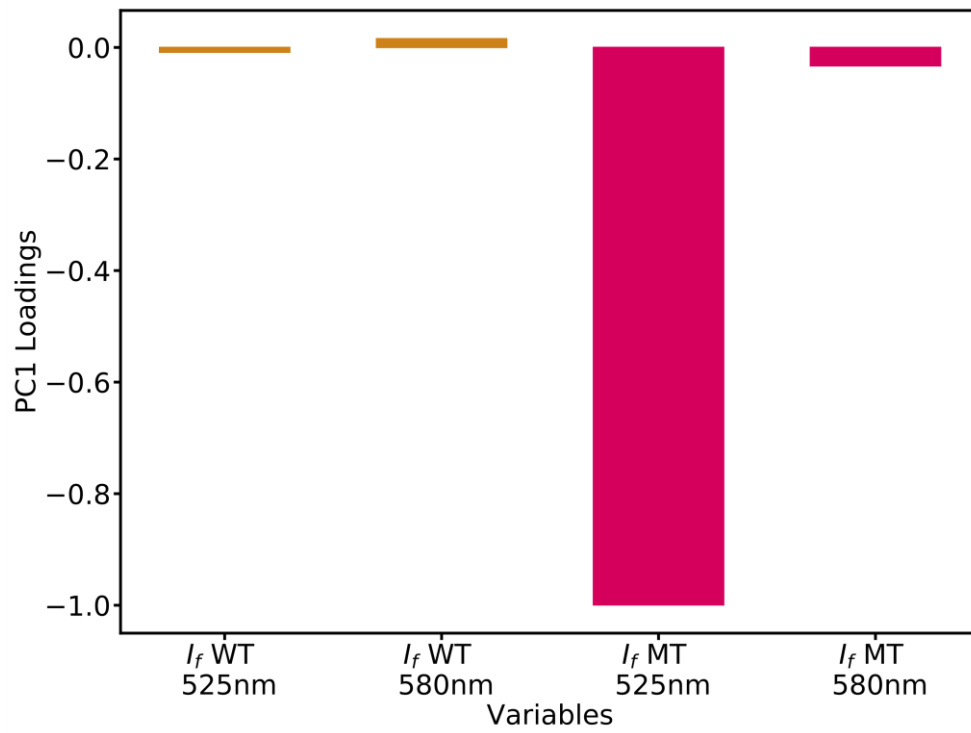


Figure 5.12. Loadings plot for principal component 1 (PC1).

CHAPTER 6

NUCLEAR PENETRATION OF PDOT IN BREAST CANCER CELL TYPES

Great progress has been recorded in the field of cell and tissue imaging as a result of the development of advanced fluorescent nanoparticles prepared from conjugated polyelectrolytes. Because of their photophysical characteristics and small particle size, conjugated polymer dots (Pdots) have been widely used for bioimaging. Ultra-small particle size allows them to be highly penetrable into cell compartments while fluorescence emission provides highly detectable signal for tracking them in the biological environment. Fluorescence emitting nanoparticles in the visible area have been used to conduct 2D cell imaging experiments.¹⁰⁶⁻¹⁰⁹ For 3D tissue imaging, mostly IR emitting Pdots, on the other hand, have been utilized.¹¹⁰⁻¹¹² Here in this chapter, a comparative study of 2D cancerous cell imaging of MCF-7 (human epithelial breast adenocarcinoma), MDA-MB-231 (human epithelial breast adenocarcinoma), and NIH 3T3 (mouse fibroblast) cell line by Pdots form of a cationic polythiophene fluorescence reporter poly(1-(3-((4-methylthiophen-3-yl)oxy)propyl)-1,4-diazabicyclo[2.2.2]octan-1-ium).

MDA-MB-231 is a triple negative breast cancer which constitutes approximately 10-20% of all breast cancer types. It has lack of estrogen (ER), progesterone (PR), and human epidermal growth factor receptor 2 (HER2) receptors. Therefore, MDA-MB-231 cell can be diagnosed by ER-, PR, and HER2-negative responses.^{113,114} Another breast cancer type is MCF-7 which is a hormone dependent and has estrogen and progesterone receptors on cell membrane for growth and proliferation.¹¹⁵

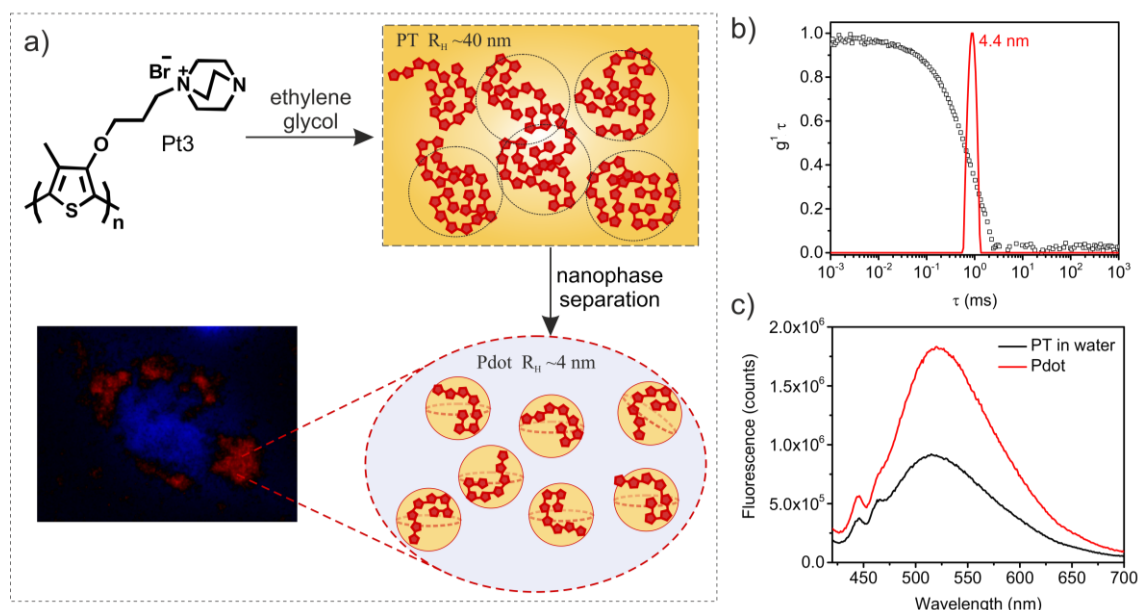


Figure 6.1. a) Schematic representation of polymer dot (Pdot) formation. b) DLS autocorrelation function $g_1(t)$ of Pdot with size distribution. c) Fluorescence spectra of PT and Pdot.

6.1. Materials and Methods

MCF-7 (human epithelial breast adenocarcinoma, ATCC HTB-22), MDA-MB-231 (human epithelial breast adenocarcinoma, ATCC HTB-26), SH-SY5Y (human bone-marrow neuroblastoma, ATCC CRL-2266), SAOS 2 (human bone osteosarcoma, ATCC HTB-85) cancer cell lines and NIH/3T3 (mouse fibroblast, ATCC CRL-1658) healthy cells lines were cultured in DMEM of high glucose medium including L-glutamine and cell culture medium was supplemented with 10% Fetal Bovine Serum and 1% penicillin/streptomycin solutions. BCE CD-1b (cow endothelial eye/cornea, ATCC CRL-2048) healthy cells lines were cultured in DMEM, 10% fetal bovine serum, 1% penicillin/streptomycin and additionally 1% sodium pyruvate mediums. DMEM, bovine serum, antibiotic, and sodium pyruvate solutions were purchased from GIBCO, Thermo Fischer Scientific. The cells were cultured up to $\sim 90\%$ confluency in a humidified environment ($5\% \text{ CO}_2$, 37°C). The harvested cells were used for further 2D and 3D cell culture studies.

PT-2D cell culture studies. Cancer and healthy cells were used to investigate interaction of Pdot and cells in various cell density (1×10^4 and 5×10^4 cell/well). $60 \mu\text{M}$

of Pdot concentration were applied to cells and analysis was performed using a fluorescence microscope (Zeiss Axio Observer) after 24h culturing time.

CytoCalcein™ Green (AAT Bioquest) was applied to evaluate cell viability of spheroids. Cells were incubated in the dye solution at 37°C for 30 min for staining. DAPI (AAT Bioquest) solution was then added to the culture for 5 minutes before the rinsing procedure. After nucleus staining accomplished, rinsing was finally applied to spheroids three times and fluorescence images of spheroids were captured by fluorescence microscope (Zeiss Axio Observer).

6.2. Results and Discussion

For the investigation of triple negative and hormone dependent breast cancer types, conjugated polymer dots of polythiophene were utilized in 2D cell culture. Pdots having small size (R_H around 4 nm) are known to penetrate the nucleus of hepatocellular carcinoma cell. From this knowledge, Pdots were used as a fluorescent probe in imaging of MCF-7 (a hormone dependent breast cancer cell line), MDA MB 231 (a triple negative breast cancer), and NIH 3T3 fibroblast cell lines.

A custom Python 3.8 algorithm using opencv and numpy libraries (the whole script can be found in Appendix B) was developed for image analysis of fluorescence micrographs of cells which are incubated with 60 μM of Pdots to understand the RGB code discrepancy and the localization of Pdots. The design of this algorithm is based on collecting RGB codes and then reducing them into a single channel. Following this step, the single-channel color codes are normalized as the minimum is 0 and the maximum is 255. Finally, the matrix difference is applied to fluorescence images of cells obtained by Pdot and DAPI excitation channels. The functions utilized in the algorithm are as following:

```
normbwimage(img):
```

```
newimg = np.float64(img.copy())
```

```
newimg = ((newimg - np.min(newimg)) / (np.max(newimg) - np.min(newimg))) * 255
```

```
newimg = np.int64(np.round(newimg))
```

```
return newimg
```

```
diffimage(img1,img2,c1='r',c2='b'):
```

```

diff = img1 - img2
img1dominant = diff.copy()
img1dominant[img1dominant < 0] = 0
img2dominant = diff.copy()
img2dominant[img2dominant > 0] = 0
img2dominant = img2dominant * -1
merged = np.zeros([img1.shape[0],img1.shape[1],3],np.uint8)

```

New RGB codes for overlapping Pdot and DAPI staining in the same pixel are obtained from fluorescence emission in the images. The fluorescence emission of red intensities (Pdot) and blue intensities (DAPI) are calculated in percent after matrix difference. Comparison of ultra-small sized Pdot behavior in triple negative and hormone dependent breast cancer cell lines are performed using the percentages. Ratios of red and blue intensities were calculated as following:

$$I_{red/blue} = \frac{I_{red/blue} (after\ matrix\ diff.)}{I_{red/blue} (after\ norm.)} \times 100 \quad (6.1)$$

I_{red} and I_{blue} indicates the percentage of remaining red and blue intensities corresponding to Pdot and DAPI, respectively, of a cell image acquired after normalization and matrix difference with respect to the color codes after normalization before matrix difference function. The matching red and blue codes, due to the emission from Pdot and DAPI, in the exact pixels cancel each other out at the matrix difference step. Therefore, red intensity after the image processing is specifying the final Pdot contribution excluding the red intensities overlapping with the blue intensity from DAPI, and vice versa. In other words, I_{red} expresses the percent Pdot fluorescence emitted from different location than DAPI.

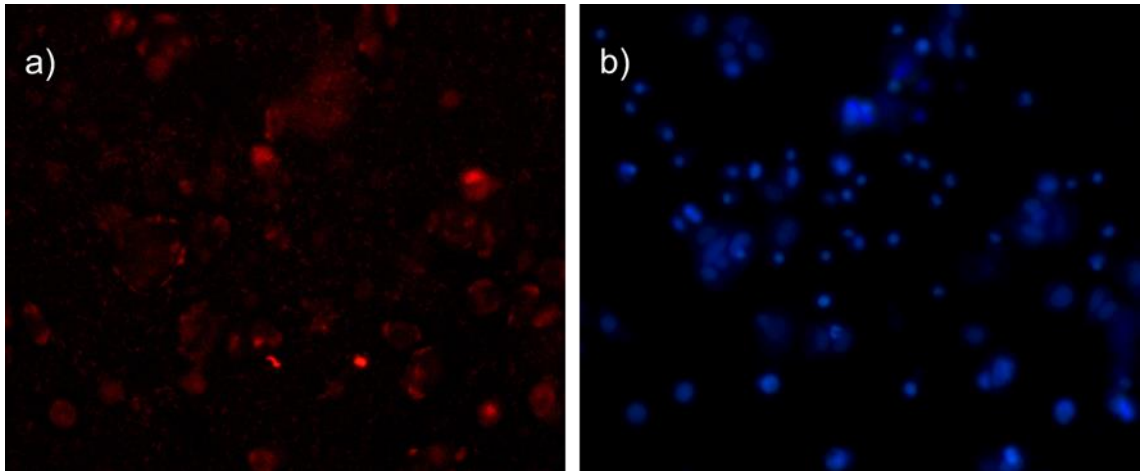


Figure 6.2. Fluorescence microscope images of MCF-7 cells (10000 cells/well) incubated in a) Pdot and b) DAPI. (20X magnification)

Figure 6.2 demonstrated the fluorescence microscope images of MCF-7 cell line which contains 10000 cells per well and is cultured with Pdot and DAPI. Since MCF-7 is a hormone dependent breast cancer type, most of the breast cancer types have estrogen and progesterone receptors are usually located nuclear membrane for growth and proliferation.¹¹⁶

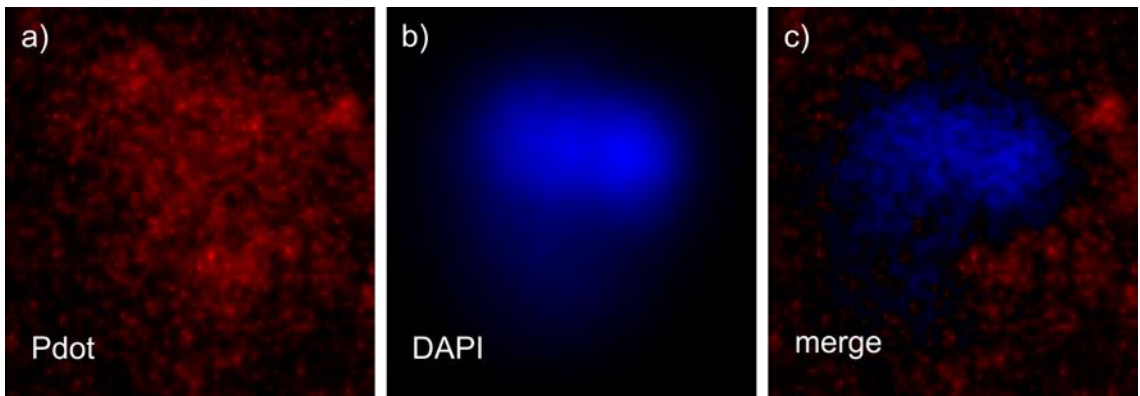


Figure 6.3. A typical normalized fluorescence images of a) Pdot, b) DAPI in MCF-7 cells, and c) matrix difference of images a and b.

Normalized fluorescence image of a single cell processed with the python script is illustrated in Figure 6.3. Each individual cell was cropped with exact pixel precision through the script then the normalization and matrix difference were applied to new images. The microscope images of MCF-7 cells collected from Pdot and DAPI incubation in Figure 6.3 a and b, respectively after normalization and their merged image after

normalization and matrix difference was given in Figure 6.3 c. Pdot and DAPI staining were first normalized by the RGB code with the range of 0 and 255, they were then subtracted from each other by a RGB code matrix difference function. Therefore, the total overlapping signals of Pdot and DAPI appear as black in the merged image and the dominant color code remains in the image after subtraction. In other words, if the equivalent Pdot and DAPI signals are existing in the same location, the combination of red and blue codes from Pdot and DAPI results in zero which indicates the color code of black. If the signal of Pdot is greater than that of DAPI, the subtraction leads remnant red code in which Pdot appears as dominant character in the merged image or vice versa. From the equation 6.1, the percent remaining red intensity (I_{red}) of MCF-7 cells after matrix difference was found to be 23%. which indicates that most Pdots was localized in the same region accompanied by DAPI and diminished intensity was observed due to overlapping.

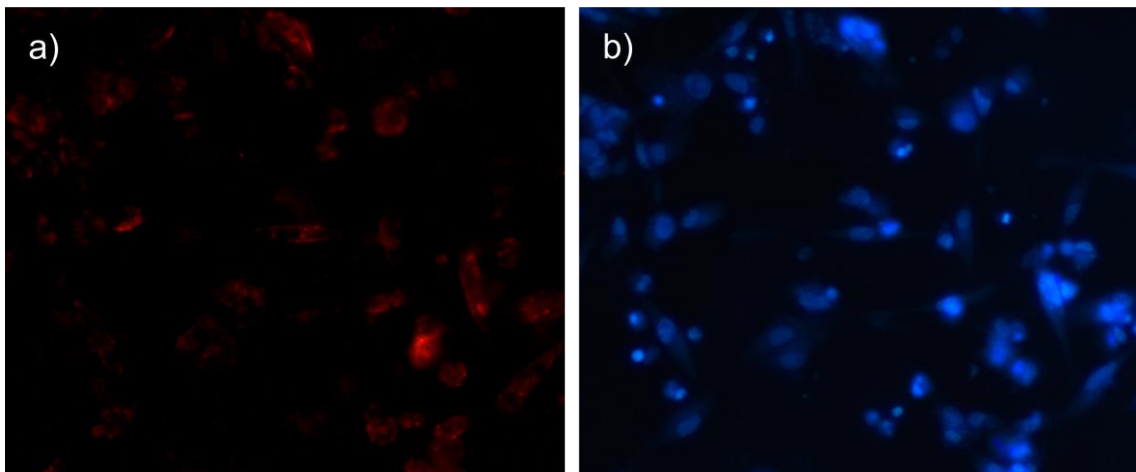


Figure 6.4. Fluorescence microscope images of MDA-MB-231 cells (10000 cells/well) incubated in a) Pdot and b) DAPI. (20X magnification)

Fluorescence microscope images of MDA-MB-231 cell line obtained from Pdot and DAPI channel are demonstrated in Figure 6.4. Pdot and DAPI accumulation is seen to be located in similar areas which indicates nuclear penetration of Pdot in MDA-MB-231 cells compared to MCF-7 cells. The invasive characteristics of MDA-MB-231 cells were reported in numerous studies. Upon loss of cell-substrate connection creates greater nuclear deformities such as grooves, invagination, lobes, and semicircular contour in the invasive cells.¹¹⁷ This feature can be attributed to the more nuclear penetration of Pdot in MDA-MB-231 cells compared to MCF-7.

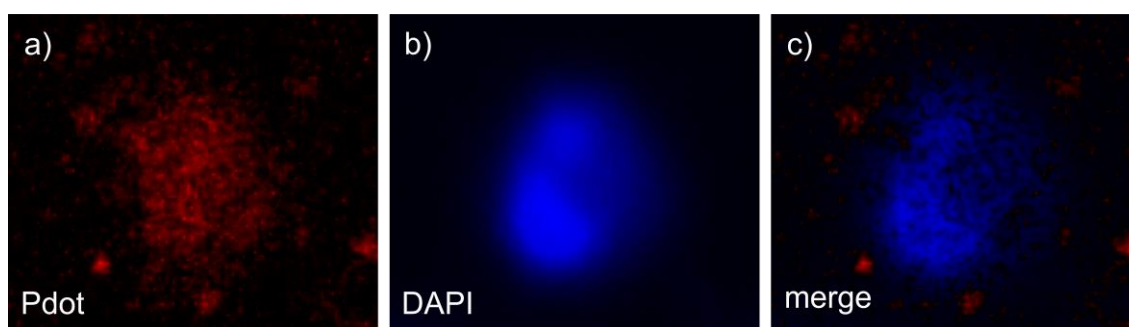


Figure 6.5. A typical normalized fluorescence images of a) Pdot, b) DAPI in MDA-MB-231 cells, and c) matrix difference of images a and b.

Figure 6.5 illustrates typical images of individual MDA-MB-231 cell cropped by Python algorithm after normalization and matrix difference as well. The nucleus border of the cell can be smoothly discriminated in both images (Figure 6.5 a and b) from Pdot and DAPI channels. The invasive nature of MDA-MB-7 cells causes nuclear deformities, allowing greater amount Pdot to penetrate into cell nuclei thus nucleus-staining property of small molecule DAPI is achieved by a fluorescent polyelectrolyte selectively. The merged image given in Figure 6.5c represents the combined red and blue intensities after normalization followed by matrix difference of Pdot and DAPI. The red intensity (I_{red}) was calculated by equation 6.1 as 17% which indicates lower amount of Pdot remain out of the MDA-MB-231 cell nucleus.

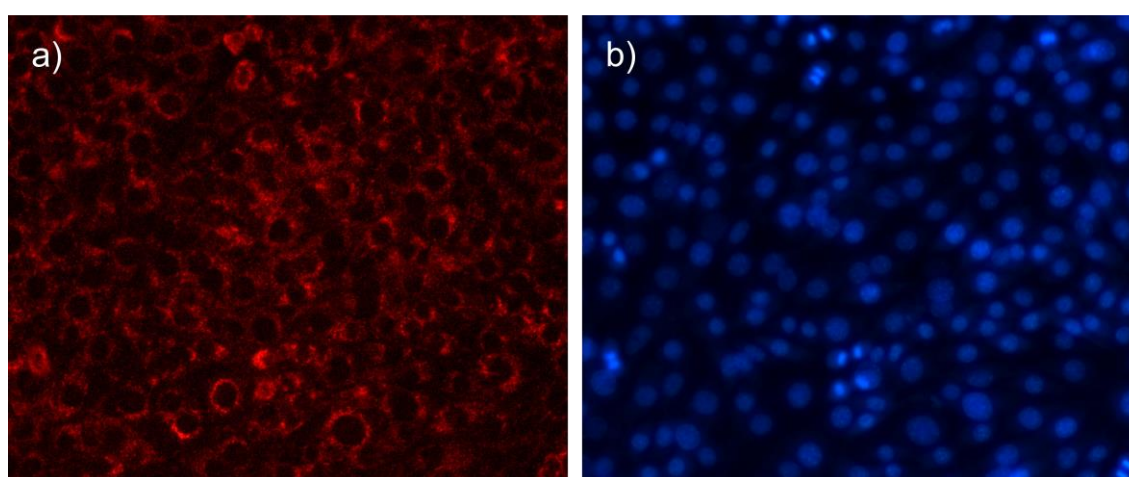


Figure 6.6. Fluorescence microscope images of NIH 3T3 cells (10000 cells/well) incubated in a) Pdot and b) DAPI. (20X magnification)

In 2D cell culture experiments were conducted by utilization of NIH 3T3 healthy cells in Pdot - DAPI comparison. In healthy cells, generally, the size of nuclear pore complex is relatively smaller than cancerous cells and the integrity of nuclear envelope is preserved for the selective cargo transport between nucleus and cytoplasm.¹¹⁸ The fluorescence microscope images of NIH 3T3 fibroblast cells with an identical cell population, were displayed in Figure 6.6 a from Pdot channel and b from DAPI channel. Ring like structure in fluorescence emission of Pdot introduced to healthy fibroblast cells is further evidence to selective nuclear translocation of Pdot.⁶² Pdot accumulation in NIH 3T3 cell cytoplasm just around the nucleus were ubiquitously observed in Figure 6.6a and routine nucleus staining of DAPI is represented in Figure 6.6b.

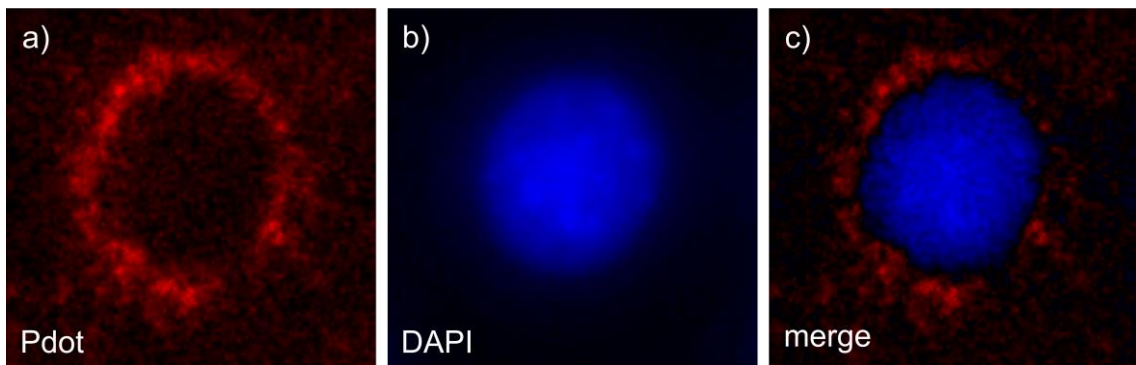


Figure 6.7. A typical normalized fluorescence images of a) Pdot, b) DAPI in NIH 3T3 cells, and c) matrix difference of images a and b.

A single NIH 3T3 cell cropped from the fluorescence microscope image is shown in Figure 6.7. The RGB-normalized images from Pdot channel and DAPI channel represented in Figure 6.7 a and b, respectively, were found to be complementary to each other as the border of NIH 3T3 has distinguishable inner margin of the ring-shaped Pdot staining.

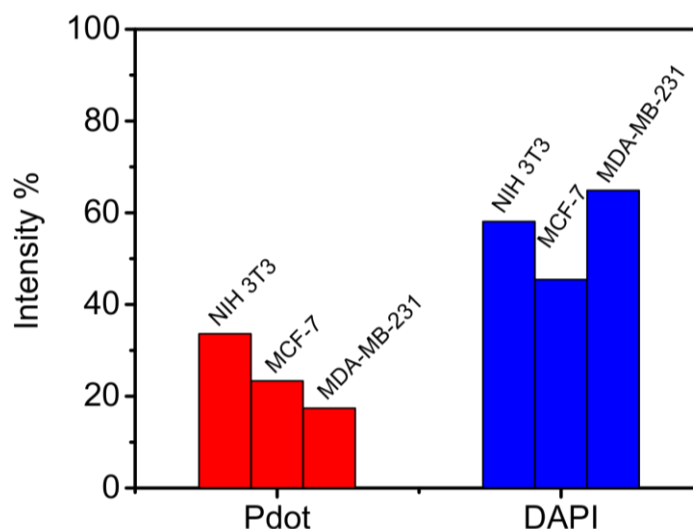


Figure 6.8. Average red and blue intensities from Pdote and DAPI, respectively for 30 cells for each cell lines.

The red and blue intensities (I_{red} and I_{blue}) was calculated from equation 6.1 is illustrated in Figure 6.8 as the intensity average of 30 cells for each cell lines: MCF-7 non-invasive breast cancer, MDA-MB-231 invasive breast cancer, and NIH 3T3 healthy fibroblast cell. The red bars indicate the I_{red} calculated from the images processed via aforementioned algorithm of MCF-7, MDA-MB-231, and NIH 3T3 cells, respectively. Decreasing percent intensity of Pdote from left to right in Figure 6.8 expresses the increase in nuclear penetration of Pdote in cancerous cells specially in invasive cells. However, the blue intensities calculated from three cell types are not correlating with staining characteristic of Pdote and it is attributed to the discrepancy in initial intensities of Pdote and DAPI due to the fluorescence nature of small molecule and polyelectrolyte. Therefore, the initial total intensities acquired from the algorithm is then involved in principal component analysis (PCA) to get a reliable discrimination of three target cells.

CHAPTER 7

CONCLUSION

Ionic conjugated polythiophene a class of polyelectrolyte possessing optical responses to target through reversible conformational backbone changes, have been widely utilized in especially biological applications, from biosensors to photodynamic therapy. Nevertheless, polyelectrolytes require advancements caused by complexity of living entity and increasing needs. This thesis is mainly focuses on characterization of polyelectrolytes (CPE) and polymer dots (Pdot) with regard of improving its optical and structural properties, by spectroscopic and scattering techniques, for utilization in nucleic acid detection and cancerous cells imaging.

Solvation effect on emissive and structural characterization of CPE and Pdot was performed in four solvents, water, ethylene glycol, DMSO and 1,4-butanediol were chosen for investigation of. After detailed spectroscopic and scattering characterization, ethylene glycol was found to be “good solvent” for polyelectrolyte yielding an excellent emissive and tunable ultra-small size property. Two hydroxyl groups on ethylene glycol molecule provide very hydrophilic microenvironment to cationic conjugated polyelectrolyte, exhibiting strong electrostatic interaction with quaternary ammonium on pendant group of CPE. Therefore, approximately 10-fold increase in fluorescence intensity of polyelectrolyte dissolved in ethylene glycol among the other solvents. Single photon counting also proves that ethylene glycol solution of CPE is approaching to monomodal emissive characteristic due to the narrowed distribution of conjugation length, polyelectrolyte has on the random coil backbone conformation. However, DMSO has also significant property on fluorescence emission that red-shifted fluorescence maximum at around 560 nm was observed in DMSO solution of CPE with a slight decrease in fluorescence intensity despite its lower polarity. On the other hand, size adjustment of polyelectrolyte can be easily achieved by “nanophase separation” method between CPE-rich ethylene glycol phase and water for preparation of Pdots . The average hydrodynamic radius (R_H) of Pdot was found to be in the range of 3-10 nm and it is also feasible to obtain slightly larger particles by changing the ethylene glycol volume fraction in the protocol. 1,4-Butanediol possesses ultra-small sized Pdots by the same method, as

well, however, low fluorescence intensity and quite higher viscosity could be problematic in biological application. Thus, ethylene glycol solutions of CPE and Pdot are promising as fluorescent probe for detection of biological materials and cell imaging.

CPE-based PCR-free protocol was developed for detection of familial Mediterranean fever (FMF) as a model genetic disease with a single nucleotide polymorphism (SNP). The detection mechanism relies on fluorescence ON / OFF assay at 525 nm with respect to hybridization of complementary and non-complementary primers to the target gene. After denaturation (step 1), hybridization (step 2), and centrifugation (step 4) are applied to the separate solution of target gene and primers prior to CPE titration (step 4), fluorescence emission is observed at 525 nm indicating twisted conformation if the primer is complementary to the target. Otherwise, CPE exhibits a fluorescence signal transition from 525 to 580 nm which is the fluorescence OFF case due to backbone planarization on polyelectrolyte. Data analysis applied in the fluorescence signals of CPE at 525 and 580 nm for total 26 FMF-related clinical samples reveal a separation of healthy subjects from FMF patients and carriers with a 96% accuracy.

As a demonstrative example of fluorescent Pdot probe for cell staining, hepatocellular carcinoma (HuH-7) and healthy liver (THLE-2) cells were analyzed. Nuclear translocation of Pdot in HuH-7 cells was explicitly differentiated from the THLE-2 cells. It was observed that Pdots can penetrate into cell nucleus of HuH-7 with a seven fold increase in fluorescence intensity ratio of Pdot at nucleus to cytoplasm while accumulated around nuclei of THLE-2 cells. Rather than selective nuclear translocation of Pdot among cancerous and healthy liver cells even in the co-cultured study, Pdot also exhibits chromosomal staining in mitotic division.

REFERENCES

- (1) Leclerc, M.; Morin, J.-F. *Design and Synthesis of Conjugated Polymers*; Wiley-VCH, 2010.
- (2) Wise, D. L. (Donald L. *Photonic Polymer Systems : Fundamentals, Methods, and Applications*; M. Dekker, 1998.
- (3) Reynolds, J. R.; Thompson, B. C.; Skotheim, T. A. *Conjugated Polymers : Perspective, Theory, and New Materials*; CRC Press, 2019.
- (4) Nilsson, K. P. R.; Inganäs, O. Chip and Solution Detection of DNA Hybridization Using a Luminescent Zwitterionic Polythiophene Derivative. *Nature Materials* **2003**, 2 (6), 419–424. <https://doi.org/10.1038/nmat899>.
- (5) Price, S. C.; Stuart, A. C.; Yang, L.; Zhou, H.; You, W. Fluorine Substituted Conjugated Polymer of Medium Band Gap Yields 7% Efficiency in Polymer–Fullerene Solar Cells. *J Am Chem Soc* **2011**, 133 (12), 4625–4631. <https://doi.org/10.1021/ja1112595>.
- (6) Gross, M.; Müller, D. C.; Nothofer, H. G.; Scherf, U.; Neher, D.; Bräuchle, C.; Meerholz, K. Improving the Performance of Doped π -Conjugated Polymers for Use in Organic Light-Emitting Diodes. *Nature* **2000**, 405 (6787), 661–665. <https://doi.org/10.1038/35015037>.
- (7) Yildiz, U. H.; Sheng, C. W.; Mailepessov, D.; Xueqi, D. C.; Shochat, S. G.; Liedberg, B. Real-Time Determination of the Activity of ATPase by Use of a Water-Soluble Polythiophene. *Analytical and Bioanalytical Chemistry* **2012**, 404 (8), 2369–2375. <https://doi.org/10.1007/s00216-012-6341-8>.
- (8) Rajwar, D.; Ammanath, G.; Cheema, J. A.; Palaniappan, A.; Yildiz, U. H.; Liedberg, B. Tailoring Conformation-Induced Chromism of Polythiophene Copolymers for Nucleic Acid Assay at Resource Limited Settings. *ACS Applied Materials & Interfaces* **2016**, 8 (13), 8349–8357. <https://doi.org/10.1021/acsami.5b12171>.
- (9) Yucel, M.; Koc, A.; Ulgenalp, A.; Akkoc, G. D.; Ceyhan, M.; Yildiz, U. H. PCR-Free Methodology for Detection of Single-Nucleotide Polymorphism with a Cationic Polythiophene Reporter. *ACS Sensors* **2021**, 6 (3), 950–957. <https://doi.org/10.1021/acssensors.0c02130>.
- (10) Xia, F.; Zuo, X.; Yang, R.; Xiao, Y.; Kang, D.; Vallée-Bélisle, A.; Gong, X.; Yuen, J. D.; Hsu, B. B. Y.; Heeger, A. J.; Plaxco, K. W. Colorimetric Detection of DNA, Small Molecules, Proteins, and Ions Using Unmodified Gold Nanoparticles and Conjugated Polyelectrolytes. *Proc Natl Acad Sci U S A* **2010**, 107 (24), 10837–10841. https://doi.org/10.1073/PNAS.1005632107/SUPPL_FILE/PNAS.1005632107_SI.PDF.

- (11) Ho, H.-A.; Najari, A.; Leclerc, M. Optical Detection of DNA and Proteins with Cationic Polythiophenes. *Accounts of Chemical Research* **2008**, *41* (2), 168–178. <https://doi.org/10.1021/ar700115t>.
- (12) Ghosh, R.; Chatterjee, D. P.; Das, S.; Mukhopadhyay, T. K.; Datta, A.; Nandi, A. K. Influence of Hofmeister I– on Tuning Optoelectronic Properties of Ampholytic Polythiophene by Varying PH and Conjugating with RNA. *Langmuir* **2017**, *33* (44), 12739–12749. <https://doi.org/10.1021/acs.langmuir.7b03147>.
- (13) Ho, H.-A.; Béra-Abérem, M.; Leclerc, M. Optical Sensors Based on Hybrid DNA/Conjugated Polymer Complexes. *Chemistry – A European Journal* **2005**, *11* (6), 1718–1724. <https://doi.org/https://doi.org/10.1002/chem.200400537>.
- (14) He, F.; Feng, F.; Duan, X.; Wang, S.; Li, Y.; Zhu, D. Selective and Homogeneous Fluorescent DNA Detection by Target-Induced Strand Displacement Using Cationic Conjugated Polyelectrolytes. *Analytical Chemistry* **2008**, *80* (6), 2239–2243. <https://doi.org/10.1021/ac702415p>.
- (15) Liang, J.; Li, K.; Liu, B. Visual Sensing with Conjugated Polyelectrolytes. *Chemical Science* **2013**, *4* (4), 1377–1394. <https://doi.org/10.1039/C2SC21792A>.
- (16) Ho, H.-A.; Boissinot, M.; Bergeron, M. G.; Ve Corbeil, G. ; Dore, K.; Boudreau, D.; Leclerc, M.; O×reilly, M. S.; Holmgren, L.; Shing, Y.; Chen, C.; Rosenthal, R. A.; Moses, M.; Lane, W. S.; Cao, Y.; Sage, E. H.; Folkman, J. *Colorimetric and Fluorometric Detection of Nucleic Acids Using Cationic Polythiophene Derivatives***.
- (17) Feng, X.; Liu, L.; Wang, S.; Zhu, D. Water-Soluble Fluorescent Conjugated Polymers and Their Interactions with Biomacromolecules for Sensitive Biosensors. *Chemical Society Reviews* **2010**, *39* (7), 2411–2419. <https://doi.org/10.1039/B909065G>.
- (18) Garreau, S.; Leclerc, M.; Errien, N.; Louarn, G. Planar-to-Nonplanar Conformational Transition in Thermochromic Polythiophenes: A Spectroscopic Study. *Macromolecules* **2003**, *36* (3), 692–697. <https://doi.org/10.1021/ma021358d>.
- (19) Yildiz, U. H.; Alagappan, P.; Liedberg, B. Naked Eye Detection of Lung Cancer Associated MiRNA by Paper Based Biosensing Platform. *Analytical Chemistry* **2013**, *85* (2), 820–824. <https://doi.org/10.1021/ac3034008>.
- (20) Aydın, H. B.; Cheema, J. A.; Ammanath, G.; Toklucu, C.; Yucel, M.; Özenler, S.; Palaniappan, A.; Liedberg, B.; Yildiz, U. H. Pixelated Colorimetric Nucleic Acid Assay. *Talanta* **2020**, *209*, 120581. <https://doi.org/https://doi.org/10.1016/j.talanta.2019.120581>.
- (21) Ammanath, G.; Yeasmin, S.; Srinivasulu, Y.; Vats, M.; Cheema, J. A.; Nabilah, F.; Srivastava, R.; Yildiz, U. H.; Alagappan, P.; Liedberg, B. Flow-through Colorimetric Assay for Detection of Nucleic Acids in Plasma. *Analytica Chimica*

Acta **2019**, *1066*, 102–111.
<https://doi.org/https://doi.org/10.1016/j.aca.2019.03.036>.

- (22) Rajwar, D.; Ammanath, G.; Cheema, J. A.; Palaniappan, A.; Yildiz, U. H.; Liedberg, B. Tailoring Conformation-Induced Chromism of Polythiophene Copolymers for Nucleic Acid Assay at Resource Limited Settings. *ACS Appl Mater Interfaces* **2016**, *8* (13), 8349–8357.
<https://doi.org/10.1021/acsami.5b12171>.
- (23) Yildiz, U. H.; Sheng, C. W.; Mailepessov, D.; Xueqi, D. C.; Shochat, S. G.; Liedberg, B. Real-Time Determination of the Activity of ATPase by Use of a Water-Soluble Polythiophene. *Anal Bioanal Chem* **2012**, *404* (8), 2369–2375.
<https://doi.org/10.1007/s00216-012-6341-8>.
- (24) Yildiz, U. H.; de Hoog, H.-P. M.; Fu, Z.; Tomczak, N.; Parikh, A. N.; Nallani, M.; Liedberg, B. Third-Party ATP Sensing in Polymersomes: A Label-Free Assay of Enzyme Reactions in Vesicular Compartments. *Small* **2014**, *10* (3), 442–447. <https://doi.org/10.1002/sml.201300060>.
- (25) Sinsinbar, G.; Palaniappan, A.; Yildiz, U. H.; Liedberg, B. A Perspective on Polythiophenes as Conformation Dependent Optical Reporters for Label-Free Bioanalytics. *ACS Sensors* **2022**, *7* (3), 686–703.
<https://doi.org/10.1021/acssensors.1c02476>.
- (26) Li, S. F. Y.; Wu, Y. S. ELECTROPHORESIS | Capillary Electrophoresis. *Encyclopedia of Separation Science* **2000**, 1176–1187.
<https://doi.org/10.1016/B0-12-226770-2/04321-0>.
- (27) Scharber, M. C.; Sariciftci, N. S. Low Band Gap Conjugated Semiconducting Polymers. *Advanced Materials Technologies* **2021**, *6* (4), 2000857.
<https://doi.org/https://doi.org/10.1002/admt.202000857>.
- (28) Ahumada, G.; Borkowska, M. Fluorescent Polymers Conspectus. *Polymers (Basel)* **2022**, *14* (6), 1118. <https://doi.org/10.3390/polym14061118>.
- (29) Ding, D.; Pu, K.-Y.; Li, K.; Liu, B. Conjugated Oligoelectrolyte-Polyhedral Oligomeric Silsesquioxane Loaded PH-Responsive Nanoparticles for Targeted Fluorescence Imaging of Cancer Cell Nucleus. *Chem. Commun.* **2011**, *47* (35), 9837–9839. <https://doi.org/10.1039/C1CC13237G>.
- (30) Sun, K.; Tang, Y.; Li, Q.; Yin, S.; Qin, W.; Yu, J.; Chiu, D. T.; Liu, Y.; Yuan, Z.; Zhang, X.; Wu, C. In Vivo Dynamic Monitoring of Small Molecules with Implantable Polymer-Dot Transducer. *ACS Nano* **2016**, *10* (7), 6769–6781.
<https://doi.org/10.1021/acsnano.6b02386>.
- (31) Moon, J. H.; MacLean, P.; McDaniel, W.; Hancock, L. F. Conjugated Polymer Nanoparticles for Biochemical Protein Kinase Assay. *Chem. Commun.* **2007**, No. 46, 4910–4912. <https://doi.org/10.1039/B710807A>.
- (32) Yang, Y.; Chen, J.; Yang, Y.; Xie, Z.; Song, L.; Zhang, P.; Liu, C.; Liu, J. A 1064 Nm Excitable Semiconducting Polymer Nanoparticle for Photoacoustic

- Imaging of Gliomas. *Nanoscale* **2019**, *11* (16), 7754–7760.
<https://doi.org/10.1039/C9NR00552H>.
- (33) Yu, J.; Rong, Y.; Kuo, C.-T.; Zhou, X.-H.; Chiu, D. T. Recent Advances in the Development of Highly Luminescent Semiconducting Polymer Dots and Nanoparticles for Biological Imaging and Medicine. *Analytical Chemistry* **2017**, *89* (1), 42–56. <https://doi.org/10.1021/acs.analchem.6b04672>.
- (34) Wu, C.; Schneider, T.; Zeigler, M.; Yu, J.; Schiro, P. G.; Burnham, D. R.; McNeill, J. D.; Chiu, D. T. Bioconjugation of Ultrabright Semiconducting Polymer Dots for Specific Cellular Targeting. *J Am Chem Soc* **2010**, *132* (43), 15410–15417. <https://doi.org/10.1021/ja107196s>.
- (35) Guo, B.; Sheng, Z.; Kenry; Hu, D.; Lin, X.; Xu, S.; Liu, C.; Zheng, H.; Liu, B. Biocompatible Conjugated Polymer Nanoparticles for Highly Efficient Photoacoustic Imaging of Orthotopic Brain Tumors in the Second Near-Infrared Window. *Mater. Horiz.* **2017**, *4* (6), 1151–1156.
<https://doi.org/10.1039/C7MH00672A>.
- (36) Kuo, C.-T.; Thompson, A. M.; Gallina, M. E.; Ye, F.; Johnson, E. S.; Sun, W.; Zhao, M.; Yu, J.; Wu, I.-C.; Fujimoto, B.; DuFort, C. C.; Carlson, M. A.; Hingorani, S. R.; Paguirigan, A. L.; Radich, J. P.; Chiu, D. T. Optical Painting and Fluorescence Activated Sorting of Single Adherent Cells Labelled with Photoswitchable Pdots. *Nature Communications* **2016**, *7* (1), 11468.
<https://doi.org/10.1038/ncomms11468>.
- (37) Li, P.; Liu, L.; Xiao, H.; Zhang, W.; Wang, L.; Tang, B. A New Polymer Nanoprobe Based on Chemiluminescence Resonance Energy Transfer for Ultrasensitive Imaging of Intrinsic Superoxide Anion in Mice. *J Am Chem Soc* **2016**, *138* (9), 2893–2896. <https://doi.org/10.1021/jacs.5b11784>.
- (38) Feng, L.; Zhu, C.; Yuan, H.; Liu, L.; Lv, F.; Wang, S. Conjugated Polymer Nanoparticles: Preparation, Properties, Functionalization and Biological Applications. *Chem. Soc. Rev.* **2013**, *42* (16), 6620–6633.
<https://doi.org/10.1039/C3CS60036J>.
- (39) Ye, F.; Wu, C.; Jin, Y.; Wang, M.; Chan, Y.-H.; Yu, J.; Sun, W.; Hayden, S.; Chiu, D. T. A Compact and Highly Fluorescent Orange-Emitting Polymer Dot for Specific Subcellular Imaging. *Chem Commun (Camb)* **2012**, *48* (12), 1778–1780. <https://doi.org/10.1039/c2cc16486h>.
- (40) Grey, J. K.; Kim, D. Y.; Norris, B. C.; Miller, W. L.; Barbara, P. F. Size-Dependent Spectroscopic Properties of Conjugated Polymer Nanoparticles. *The Journal of Physical Chemistry B* **2006**, *110* (51), 25568–25572.
<https://doi.org/10.1021/jp065990a>.
- (41) Tuncel, D.; Demir, H. V. Conjugated Polymer Nanoparticles. *Nanoscale* **2010**, *2* (4), 484. <https://doi.org/10.1039/b9nr00374f>.
- (42) Sarrazin, P.; Chaussy, D.; Vurth, L.; Stephan, O.; Beneventi, D. Surfactant (TTAB) Role in the Preparation of 2,7-Poly(9,9-Dialkylfluorene-Co-Fluorenone)

- Nanoparticles by Miniemulsion. *Langmuir* **2009**, *25* (12), 6745–6752.
<https://doi.org/10.1021/la900259x>.
- (43) Pu, K.; Mei, J.; Jokerst, J. v.; Hong, G.; Antaris, A. L.; Chattopadhyay, N.; Shuhendler, A. J.; Kurosawa, T.; Zhou, Y.; Gambhir, S. S.; Bao, Z.; Rao, J. Diketopyrrolopyrrole-Based Semiconducting Polymer Nanoparticles for In Vivo Photoacoustic Imaging. *Advanced Materials* **2015**, *27* (35), 5184–5190.
<https://doi.org/https://doi.org/10.1002/adma.201502285>.
- (44) Ye, F.; Sun, W.; Zhang, Y.; Wu, C.; Zhang, X.; Yu, J.; Rong, Y.; Zhang, M.; Chiu, D. T. Single-Chain Semiconducting Polymer Dots. *Langmuir* **2015**, *31* (1), 499–505. <https://doi.org/10.1021/la5038684>.
- (45) Wu, C.; Hansen, S. J.; Hou, Q.; Yu, J.; Zeigler, M.; Jin, Y.; Burnham, D. R.; McNeill, J. D.; Olson, J. M.; Chiu, D. T. Design of Highly Emissive Polymer Dot Bioconjugates for In Vivo Tumor Targeting. *Angewandte Chemie* **2011**, *123* (15), 3492–3496. <https://doi.org/10.1002/ange.201007461>.
- (46) Lakowicz, J. R. Introduction to Fluorescence. In *Principles of Fluorescence Spectroscopy*; Lakowicz, J. R., Ed.; Springer US: Boston, MA, 2006; pp 1–26.
https://doi.org/10.1007/978-0-387-46312-4_1.
- (47) Berardozi, R.; Bourgeois, D.; Byrdin, M.; Glushonkov, O.; Mantovanelli, A.; Rane, L.; Wulffele, J. *Introduction to Fluorescent Proteins Based on the Introduction Chapter of Daniel Thedié's PhD Thesis with Input from Virgile Adam*.
- (48) Frackowiak, D. *News and Views The Jablonski Diagram*; 1988; Vol. 2.
- (49) So, P. T.; Dong, C. Y. Fluorescence Spectrophotometry. In *eLS*; Wiley, 2001.
<https://doi.org/10.1038/npg.els.0002978>.
- (50) Chu, B.; Liu, T. Characterization of Nanoparticles by Scattering Techniques. *Journal of Nanoparticle Research* **2000**, *2* (1), 29–41.
<https://doi.org/10.1023/A:1010001822699>.
- (51) Schärfl, Wolfgang. *Light Scattering from Polymer Solutions and Nanoparticle Dispersions*; Springer, 2007.
- (52) Stetefeld, J.; McKenna, S. A.; Patel, T. R. Dynamic Light Scattering: A Practical Guide and Applications in Biomedical Sciences. *Biophys Rev* **2016**, *8* (4), 409–427. <https://doi.org/10.1007/s12551-016-0218-6>.
- (53) Harding, S. E.; Jumel, K. Light Scattering. *Current Protocols in Protein Science* **1998**, *11* (1). <https://doi.org/10.1002/0471140864.ps0708s11>.
- (54) Berne, B. J.; Pecora, R. *Dynamic Light Scattering: With Applications to Chemistry, Biology, and Physics*. New York, USA: John Wiley & Sons, Inc. 1976.
- (55) Dobrucki, J. W.; Kubitscheck, U. Fluorescence Microscopy. In *Fluorescence Microscopy*; Wiley-VCH Verlag GmbH & Co. KGaA: Weinheim, Germany, 2017; pp 85–132. <https://doi.org/10.1002/9783527687732.ch3>.

- (56) Aryal, S. *Fluorescence Microscopy- Definition, Principle, Parts, Uses*.
- (57) Lichtman, J. W.; Conchello, J.-A. Fluorescence Microscopy. *Nature Methods* **2005**, 2 (12), 910–919. <https://doi.org/10.1038/nmeth817>.
- (58) Carl Zeiss Microscopy. *Principles of Fluorescence and Fluorescence Microscopy*; 2019.
- (59) ThorLabs. *Filters for Fluorescence Microscopy*.
- (60) Hu, W. *Polymer Physics; A Molecular Approach*; Springer Vienna: Vienna, 2013. <https://doi.org/10.1007/978-3-7091-0670-9>.
- (61) Özenler, S.; Yucel, M.; Tüncel, Ö.; Kaya, H.; Özçelik, S.; Yildiz, U. H. Single Chain Cationic Polymer Dot as a Fluorescent Probe for Cell Imaging and Selective Determination of Hepatocellular Carcinoma Cells. *Analytical Chemistry* **2019**, 91 (16), 10357–10360. <https://doi.org/10.1021/acs.analchem.9b02300>.
- (62) Skoog, D. A.; West, D. M. *Principles of Instrumental Analysis*, 2nd ed.; Saunders College: Philadelphia, 1980.
- (63) Haidekker, M. A.; Theodorakis, E. A. Environment-Sensitive Behavior of Fluorescent Molecular Rotors. *Journal of Biological Engineering*. September 15, 2010. <https://doi.org/10.1186/1754-1611-4-11>.
- (64) Eder, T.; Stangl, T.; Gmelch, M.; Remmersen, K.; Laux, D.; Höger, S.; Lupton, J. M.; Vogelsang, J. Switching between H- and J-Type Electronic Coupling in Single Conjugated Polymer Aggregates. *Nature Communications* **2017**, 8 (1), 1641. <https://doi.org/10.1038/s41467-017-01773-0>.
- (65) Chatterjee, T.; Mandal, M.; Mandal, P. K. Solvent H-Bond Accepting Ability Induced Conformational Change and Its Influence towards Fluorescence Enhancement and Dual Fluorescence of Hydroxy Meta-GFP Chromophore Analogue. *Physical Chemistry Chemical Physics* **2016**, 18 (35), 24332–24342. <https://doi.org/10.1039/C6CP04219H>.
- (66) Sakuma, S.; D'Angelo, M. A. The Roles of the Nuclear Pore Complex in Cellular Dysfunction, Aging and Disease. *Semin Cell Dev Biol* **2017**, 68, 72–84. <https://doi.org/10.1016/j.semcdb.2017.05.006>.
- (67) Paine, P. L.; Moore, L. C.; Horowitz, S. B. Nuclear Envelope Permeability. *Nature* **1975**, 254 (5496), 109–114. <https://doi.org/10.1038/254109a0>.
- (68) Simon, D. N.; Rout, M. P. Cancer and the Nuclear Pore Complex. *Adv Exp Med Biol* **2014**, 773, 285–307. https://doi.org/10.1007/978-1-4899-8032-8_13.
- (69) Pu, K.-Y.; Li, K.; Liu, B. Cationic Oligofluorene-Substituted Polyhedral Oligomeric Silsesquioxane as Light-Harvesting Unimolecular Nanoparticle for Fluorescence Amplification in Cellular Imaging. *Adv Mater* **2010**, 22 (5), 643–646. <https://doi.org/10.1002/adma.200902409>.

- (70) Ye, F.; Wu, C.; Jin, Y.; Wang, M.; Chan, Y.-H.; Yu, J.; Sun, W.; Hayden, S.; Chiu, D. T. A Compact and Highly Fluorescent Orange-Emitting Polymer Dot for Specific Subcellular Imaging. *Chemical Communications* **2012**, 48 (12), 1778–1780. <https://doi.org/10.1039/C2CC16486H>.
- (71) Yuzugullu, H.; Benhaj, K.; Ozturk, N.; Senturk, S.; Celik, E.; Toyly, A.; Tasdemir, N.; Yilmaz, M.; Erdal, E.; Akcali, K. C.; Atabey, N.; Ozturk, M. Canonical Wnt Signaling Is Antagonized by Noncanonical Wnt5a in Hepatocellular Carcinoma Cells. *Molecular Cancer* **2009**, 8 (1), 90. <https://doi.org/10.1186/1476-4598-8-90>.
- (72) Harris, C. C.; Cole, K. H.; Lechner, J. F.; reddel, R. Human Liver Epithelial Cell Lines. 5,759,765, June 2, 1998.
- (73) Tomizawa, M.; Shinozaki, F.; Motoyoshi, Y.; Sugiyama, T.; Yamamoto, S.; Ishige, N. Co-Culture of Hepatocellular Carcinoma Cells and Human Umbilical Endothelial Cells Damaged by SU11274. *Biomed Rep* **2014**, 2 (6), 799–803. <https://doi.org/10.3892/br.2014.361>.
- (74) Kawakatsu, T. *Statistical Physics of Polymers*; Springer Berlin Heidelberg: Berlin, Heidelberg, 2004. <https://doi.org/10.1007/978-3-662-10024-0>.
- (75) Bhattacharjee, S. M.; Giacometti, A.; Maritan, A. Flory Theory for Polymers. *Journal of Physics: Condensed Matter* **2013**, 25 (50), 503101. <https://doi.org/10.1088/0953-8984/25/50/503101>.
- (76) Jevtić, P.; Edens, L. J.; Vuković, L. D.; Levy, D. L. Sizing and Shaping the Nucleus: Mechanisms and Significance. *Current Opinion in Cell Biology* **2014**, 28, 16–27. <https://doi.org/10.1016/j.ceb.2014.01.003>.
- (77) Okudela, K. An Association between Nuclear Morphology and Immunohistochemical Expression of P53 and P16INK4A in Lung Cancer Cells. *Med Mol Morphol* **2014**, 47 (3), 130–136. <https://doi.org/10.1007/s00795-013-0052-x>.
- (78) Sukhumsirichart, W. Polymorphisms. In *Genetic Diversity and Disease Susceptibility*; InTech, 2018. <https://doi.org/10.5772/intechopen.76728>.
- (79) Zhang, Y.; Guo, Y.; Quirke, P.; Zhou, D. Ultrasensitive Single-Nucleotide Polymorphism Detection Using Target-Recycled Ligation, Strand Displacement and Enzymatic Amplification. *Nanoscale* **2013**, 5 (11), 5027–5035. <https://doi.org/10.1039/C3NR01010D>.
- (80) Shen, W.; Deng, H.; Gao, Z. Gold Nanoparticle-Enabled Real-Time Ligation Chain Reaction for Ultrasensitive Detection of DNA. *J Am Chem Soc* **2012**, 134 (36), 14678–14681. <https://doi.org/10.1021/ja306265n>.
- (81) Liu, G.; Wan, Y.; Gau, V.; Zhang, J.; Wang, L.; Song, S.; Fan, C. An Enzyme-Based E-DNA Sensor for Sequence-Specific Detection of Femtomolar DNA Targets. *J Am Chem Soc* **2008**, 130 (21), 6820–6825. <https://doi.org/10.1021/ja800554t>.

- (82) Pei, H.; Lu, N.; Wen, Y.; Song, S.; Liu, Y.; Yan, H.; Fan, C. A DNA Nanostructure-Based Biomolecular Probe Carrier Platform for Electrochemical Biosensing. *Advanced Materials* **2010**, *22* (42), 4754–4758. <https://doi.org/10.1002/adma.201002767>.
- (83) Kim, J. H. PCR Free Multiple Ligase Reactions and Probe Cleavages for the SNP Detection of KRAS Mutation with Attomole Sensitivity. *Analyst* **2016**, *141* (23), 6381–6386. <https://doi.org/10.1039/C6AN00909C>.
- (84) Duan, X.; Liu, L.; Feng, F.; Wang, S. Cationic Conjugated Polymers for Optical Detection of DNA Methylation, Lesions, and Single Nucleotide Polymorphisms. *Accounts of Chemical Research* **2010**, *43* (2), 260–270. <https://doi.org/10.1021/ar9001813>.
- (85) Dubus, S.; Gravel, J.-F.; le Drogoff, B.; Nobert, P.; Veres, T.; Boudreau, D. PCR-Free DNA Detection Using a Magnetic Bead-Supported Polymeric Transducer and Microelectromagnetic Traps. *Analytical Chemistry* **2006**, *78* (13), 4457–4464. <https://doi.org/10.1021/ac060486n>.
- (86) Livneh, A.; Langevitz, P. Diagnostic and Treatment Concerns in Familial Mediterranean Fever. *Best Practice & Research Clinical Rheumatology* **2000**, *14* (3), 477–498. <https://doi.org/10.1053/berh.2000.0089>.
- (87) El-Shanti, H. I. Familial Mediterranean Fever and Renal Disease. *Saudi J Kidney Dis Transpl* **2003**, *14* (3), 378–385.
- (88) Settin, A.; El-Baz, R.; Abd Rasool, M.; El-Khalegy, H.; El-Sayed, O.; El-Bendary, M.; Al-Nagar, A.-S. M. Clinical and Molecular Diagnosis of Familial Mediterranean Fever in Egyptian Children. *J Gastrointest Liver Dis* **2007**, *16* (2), 141–145.
- (89) Samli, H.; Dogru, O.; Bukulmez, A.; Yuksel, E.; Ovali, F.; Solak, M. Relationship of Tel Hashomer Criteria and Mediterranean Fever Gene Mutations in a Cohort of Turkish Familial Mediterranean Fever Patients. *Saudi Med J* **2006**, *27* (12), 1822–1826.
- (90) Livneh, A.; Langevitz, P.; Zemer, D.; Zaks, N.; Kees, S.; Lidar, T.; Migdal, A.; Padeh, S.; Pras, M. Criteria for the Diagnosis of Familial Mediterranean Fever. *Arthritis Rheum* **1997**, *40* (10), 1879–1885. <https://doi.org/10.1002/art.1780401023>.
- (91) Caglayan, A. O.; Demiryilmaz, F.; Ozyazgan, I.; Gumus, H. MEFV Gene Compound Heterozygous Mutations in Familial Mediterranean Fever Phenotype: A Retrospective Clinical and Molecular Study. *Nephrol Dial Transplant* **2010**, *25* (8), 2520–2523. <https://doi.org/10.1093/ndt/gfp632>.
- (92) Keles, M.; Eyerci, N.; Uyanik, A.; Aydinli, B.; Sahin, G. Z.; Cetinkaya, R.; Pirim, I.; Polat, K. Y. The Frequency of Familial Mediterranean Fever Related Amyloidosis in Renal Waiting List for Transplantation. *Eurasian J Med* **2010**, *42* (1), 19–20. <https://doi.org/10.5152/eajm.2010.06>.

- (93) Gibbs, R. A. *PERSPECTIVE: ANALYTICAL BIOTECHNOLOGY DNA Amplification by the Polymerase Chain Reaction*; 1990; Vol. 62.
- (94) *PCR Technology, Principles and Applications for DNA Amplification*; Erlich, H. A., Ed.; Palgrave Macmillan London, 1989. <https://doi.org/10.1007/978-1-349-20235-5>.
- (95) Mullis, K.; Faloona, F.; Scharf, S.; Saiki, R.; Horn, G.; Erlich, H. Specific Enzymatic Amplification of DNA In Vitro: The Polymerase Chain Reaction. *Cold Spring Harbor Symposia on Quantitative Biology* **1986**, *51* (0), 263–273. <https://doi.org/10.1101/SQB.1986.051.01.032>.
- (96) Mullis, K. B.; Faloona, F. A. Specific Synthesis of DNA in Vitro via a Polymerase-Catalyzed Chain Reaction; 1987; pp 335–350. [https://doi.org/10.1016/0076-6879\(87\)55023-6](https://doi.org/10.1016/0076-6879(87)55023-6).
- (97) Delidow, B. C.; Lynch, J. P.; Peluso, J. J.; White, B. A. *Polymerase Chain Reaction Basic Protocols*.
- (98) Kadri, K. Polymerase Chain Reaction (PCR): Principle and Applications. In *Synthetic Biology - New Interdisciplinary Science*; IntechOpen, 2020. <https://doi.org/10.5772/intechopen.86491>.
- (99) Britannica. *polymerase chain reaction*. Encyclopædia Britannica.
- (100) Saiki, R. K.; Gelfand, D. H.; Stoffel, S.; Scharf, S. J.; Higuchi, R.; Horn, G. T.; Mullis, K. B.; Erlich, H. A. Primer-Directed Enzymatic Amplification of DNA with a Thermostable DNA Polymerase. *Science (1979)* **1988**, *239* (4839), 487–491. <https://doi.org/10.1126/science.2448875>.
- (101) Pabla, S. S.; Pabla, S. S. Real-Time Polymerase Chain Reaction. *Resonance* **2008**, *13* (4), 369–377. <https://doi.org/10.1007/s12045-008-0017-x>.
- (102) Dragan, A. I.; Pavlovic, R.; McGivney, J. B.; Casas-Finet, J. R.; Bishop, E. S.; Strouse, R. J.; Schenerman, M. A.; Geddes, C. D. SYBR Green I: Fluorescence Properties and Interaction with DNA. *Journal of Fluorescence* **2012**, *22* (4), 1189–1199. <https://doi.org/10.1007/s10895-012-1059-8>.
- (103) Zipper, H.; Brunner, H.; Bernhagen, J.; Vitzthum, F. Investigations on DNA Intercalation and Surface Binding by SYBR Green I, Its Structure Determination and Methodological Implications. *Nucleic Acids Res* **2004**, *32* (12), e103–e103. <https://doi.org/10.1093/nar/gnh101>.
- (104) Pedregosa FABIANPEDREGOSA, F.; Michel, V.; Grisel OLIVIERGRISEL, O.; Blondel, M.; Prettenhofer, P.; Weiss, R.; Vanderplas, J.; Cournapeau, D.; Pedregosa, F.; Varoquaux, G.; Gramfort, A.; Thirion, B.; Grisel, O.; Dubourg, V.; Passos, A.; Brucher, M.; Perrot and Édouardand, M.; Duchesnay, and Édouard; Duchesnay EDOUARD DUCHESNAY, Fré. *Scikit-Learn: Machine Learning in Python* Gaël Varoquaux Bertrand Thirion Vincent Dubourg Alexandre Passos PEDREGOSA, VAROQUAUX, GRAMFORT ET AL. Matthieu Perrot; 2011; Vol. 12.

- (105) Wu, C.; Jin, Y.; Schneider, T.; Burnham, D. R.; Smith, P. B.; Chiu, D. T. Ultrabright and Bioorthogonal Labeling of Cellular Targets Using Semiconducting Polymer Dots and Click Chemistry. *Angewandte Chemie* **2010**, *122* (49), 9626–9630. <https://doi.org/10.1002/ange.201004260>.
- (106) Aparicio-Ixta, L.; Ramos-Ortiz, G.; Pichardo-Molina, J. L.; Maldonado, J. L.; Rodríguez, M.; Tellez-Lopez, V. M.; Martinez-Fong, D.; Zolotukhin, M. G.; Fomine, S.; Meneses-Nava, M. A.; Barbosa-García, O. Two-Photon Excited Fluorescence of Silica Nanoparticles Loaded with a Fluorene-Based Monomer and Its Cross-Conjugated Polymer: Their Application to Cell Imaging. *Nanoscale* **2012**, *4* (24), 7751–7759. <https://doi.org/10.1039/c2nr31925j>.
- (107) Yu, J.; Rong, Y.; Kuo, C. T.; Zhou, X. H.; Chiu, D. T. Recent Advances in the Development of Highly Luminescent Semiconducting Polymer Dots and Nanoparticles for Biological Imaging and Medicine. *Analytical Chemistry*. American Chemical Society January 3, 2017, pp 42–56. <https://doi.org/10.1021/acs.analchem.6b04672>.
- (108) Yu, J.; Wu, C.; Zhang, X.; Ye, F.; Gallina, M. E.; Rong, Y.; Wu, I.-C.; Sun, W.; Chan, Y.-H.; Chiu, D. T. Stable Functionalization of Small Semiconducting Polymer Dots via Covalent Cross-Linking and Their Application for Specific Cellular Imaging. **2012**. <https://doi.org/10.1002/adma.201201245>.
- (109) Chowdhury, P.; Chan, Y.-H. MSDE MINI REVIEW Recent Advances in D-A-D Based Pdots with NIR-II Fluorescence for Deep-Tissue Imaging. **2022**. <https://doi.org/10.1039/d2me00034b>.
- (110) Jin, G.; He, R.; Liu, Q.; Dong, Y.; Lin, M.; Li, W.; Xu, F. Theranostics of Triple-Negative Breast Cancer Based on Conjugated Polymer Nanoparticles. *ACS Applied Materials and Interfaces* **2018**, *10* (13), 10634–10646. <https://doi.org/10.1021/acsami.7b14603>.
- (111) Wu, C.; Hansen, S. J.; Hou, Q.; Yu, J.; Zeigler, M.; Jin, Y.; Burnham, D. R.; McNeill, J. D.; Olson, J. M.; Chiu, D. T. Design of Highly Emissive Polymer Dot Bioconjugates for In Vivo Tumor Targeting. *Angewandte Chemie* **2011**, *123* (15), 3492–3496. <https://doi.org/10.1002/ange.201007461>.
- (112) Tate, C. R.; Rhodes, L. v; Segar, H. C.; Driver, J. L.; Pounder, F. N.; Burow, M. E.; Collins-Burow, B. M. Targeting Triple-Negative Breast Cancer Cells with the Histone Deacetylase Inhibitor Panobinostat. *Breast Cancer Research* **2012**, *14* (3), R79. <https://doi.org/10.1186/bcr3192>.
- (113) Mittendorf, E. A.; Philips, A. v; Meric-Bernstam, F.; Qiao, N.; Wu, Y.; Harrington, S.; Su, X.; Wang, Y.; Gonzalez-Angulo, A. M.; Akcakanat, A.; Chawla, A.; Curran, M.; Hwu, P.; Sharma, P.; Litton, J. K.; Molldrem, J. J.; Alatrash, G. PD-L1 Expression in Triple-Negative Breast Cancer. *Cancer Immunol Res* **2014**, *2* (4), 361–370. <https://doi.org/10.1158/2326-6066.CIR-13-0127>.

- (114) Goffin, V.; Bogorad, R. L.; Touraine, P. Identification of Gain-of-Function Variants of the Human Prolactin Receptor. *Methods in Enzymology* **2010**, *484* (C), 329–355. <https://doi.org/10.1016/B978-0-12-381298-8.00017-4>.
- (115) Kocanova, S.; Mazaheri, M.; Caze-Subra, S.; Bystricky, K. Ligands Specify Estrogen Receptor Alpha Nuclear Localization and Degradation. *BMC Cell Biol* **2010**, *11*, 98. <https://doi.org/10.1186/1471-2121-11-98>.
- (116) Chiotaki, R.; Polioudaki, H.; Theodoropoulos, P. A. Differential Nuclear Shape Dynamics of Invasive Andnon-Invasive Breast Cancer Cells Are Associated with Actin Cytoskeleton Organization and Stability. *Biochem Cell Biol* **2014**, *92* (4), 287–295. <https://doi.org/10.1139/bcb-2013-0120>.
- (117) Schuller, A. P.; Wojtynek, M.; Mankus, D.; Tatli, M.; Kronenberg-Tenga, R.; Regmi, S. G.; Dip, P. v; Lytton-Jean, A. K. R.; Brignole, E. J.; Dasso, M.; Weis, K.; Medalia, O.; Schwartz, T. U. The Cellular Environment Shapes the Nuclear Pore Complex Architecture. *Nature* **2021**, *598* (7882), 667–671. <https://doi.org/10.1038/s41586-021-03985-3>.

APPENDIX A

SUPPORTING INFORMATION FOR CHAPTER 5

A.1. Experimental details about PCR-free assay

Table 1. Concentrations of genomic DNAs (HZW: homozygous wild, HZM: homozygous mutant, HTZ: heterozygous).

DNA type	sample #	concentration (ng/ μ L)	DNA type	sample #	concentration (ng/ μ L)
HZW	1	51.9	HZM	1	45
	2	37.2		2	72.8
	3	54.2		3	37.3
	4	51.3		4	46.6
	5	37.7		5	14.3
	6	42.2		6	57
	7	43		7	47.4
	8	35.4	HTZ	8	33.1
	9	35.1		9	48.2
	10	40		10	60.2
	11	49.9		11	60
	12	49.6		12	42.3
		13		36.9	
		14		47.5	

Isolation of Human Genome

DNA isolation was performed from 200 mL blood samples using the ROCHE (High Pure PCR Template DNA Isolation Kit) isolation kit as follows:

- 180 mL of Tissue Lysis Buffer and 70 mL of Proteinase are added to 200 mL of blood sample, mixed and kept at 56°C for 1 hour (or 37C overnight).
- Then it is vortexed and waited for 1 hour at 90°C.
- 200 mL of Binding Buffer is added to the sample mixture and mixed.
- It is kept at 70°C for 10 minutes.
- Add 100 mL of isopropanol and mix well.
- The entire mixture is transferred to the filter tube and centrifuged at 8000 g for 1 minute. Collection tube is discarded. A new collection tube is added.
- Then 500 mL inhibitor removal buffer is added to the filter tube.

- Centrifuge at 8000 g for 1 minute. Collection tube is discarded. A new collection tube is added.
- Add 500 mL Wash Buffer and centrifuged at 8000 g for 1 minute. Collection tube is discarded. A new collection tube is added.
- Add 500 mL Wash Buffer for a second wash and centrifuge for 1 minute at 8000 g.
- It is transferred to the collection tubes and centrifuged at 13000 g for 1 minute. This allows the filter to dry.
- 1.5 mL Eppendorf tube is placed under the filter tube and elution buffer kept at 70°C is added to the filter tube. It is centrifuged at 8000 g for 1 minute. Pure DNA is obtained.
- DNA samples can be stored at -20°C.

After isolation, DNA concentrations are measured by spectrophotometric (nanodrop Thermo) methods. The concentration and purity of the DNA samples obtained are determined by measuring their absorbance at 260 nm and 280 nm wavelengths. The purity of the isolated DNA is controlled by the ratio of their absorbance at 260 nm and 280 nm, the A_{260}/A_{280} absorbance ratio of ideally pure quality DNA is expected to be 1.8 – 2.0. Generally, 20-100 ng DNA per reaction is thought to be sufficient for mutation detection.

Preparation of LIGHTSNIP FMF M694V (rs61752717) kit

For each mutation, there is a red capped tube containing primers and simple probes in lyophilized form.

105 mL water is added to each of these tubes separately. Vortex and spin.

REAL TIME PCR

Preparation of Real Time Reaction Mixes

Real time mix for each SNP separately is prepared according to the table below:

Using Roche LightCycler® FastStart DNA Master HybProbe		
For single reaction (volume)	For 5 reactions (volume)	Components
10,4 µl	52 µl	Water, PCR-grade (supplied with Roche FastStart)

1,6 µl	8 µl	25 mM Mg2 + solution (supplied with Roche FastStart)
1µl	5 µl	LightSnip M694V Mix (diluted to 105 µl)
2 µl	10 µl	Enzyme Mix (Roche FastStart: tube 1a and 1b combination)
15 µl	75 µl	TOTAL

The prepared mix is distributed in 96 Multiwell wells in the form of 15 mL and 5 mL of DNA is added to the final volume to reach 20 µL and it is worked on the LC480 device with the following instrument protocol.

Real Time PCR Protocol

Open the LC480 software.

Click the new experiment button.

Detection format Simple probe is selected and the PCR protocol below is entered.

Denaturation		Amplification			Melting curve			Cooling
Parameter								
Analysis mode	none	Quantification mode			Melting Curve Mode			none
cycle	1	60			1			1
degree [°C]	95	95	60	72	95	40	75	40
Time [hh:mm:ss]	00:10:00	00:00:10	00:00:10	00:00:15	00:00:30	00:02:00	00:00:00	00:00:30
Ramp.Rate [°C/s]	4,4	4,4	2,2	4,4	4,4	1,5	-	1,5
Acquisition Mode	none	none	single	none	none	none	Continuous	none
Acquisitions Per.							3	

Plate is loaded into the device and run with the start run button.

From the subset editor section, where the samples are placed are selected and called apply.

Sample names are entered from the sample editor section.

APPENDIX B

SUPPORTING INFORMATION FOR CHAPTER 6

Python Algorithm

```
import cv2
import numpy as np

def normbwimage(img):
    newimg = np.float64(img.copy())
    newimg = ((newimg - np.min(newimg)) / (np.max(newimg) - np.min(newimg))) * 255
    newimg = np.int64(np.round(newimg))
    return newimg

def diffimage(img1,img2,c1='r',c2='g'):
    diff = img1 - img2
    img1dominant = diff.copy()
    img1dominant[img1dominant < 0] = 0
    img2dominant = diff.copy()
    img2dominant[img2dominant > 0] = 0
    img2dominant = img2dominant * -1
    merged = np.zeros([img1.shape[0],img1.shape[1],3],np.uint8)

    if c1 == 'r':
        merged[:, :, 2] = img1dominant
    elif c1 == 'g':
        merged[:, :, 1] = img1dominant
    elif c1 == 'b':
        merged[:, :, 0] = img1dominant

    if c2 == 'r':
        merged[:, :, 2] = img2dominant
    elif c2 == 'g':
        merged[:, :, 1] = img2dominant
    elif c2 == 'b':
        merged[:, :, 0] = img2dominant

    return np.uint8(img1dominant),np.uint8(img2dominant),merged

red = np.int64(cv2.imread('PT.png')) #marks polymer
blue = np.int64(cv2.imread('DAPI.png')) #marks only nucleus
# Cropping_the_image
x1=1622
x2=1760
y1=450
y2=560
```

```

red = red[y1-1:y2-1,x1-1:x2-1,:]
blue = blue[y1-1:y2-1,x1-1:x2-1,:]

# Combine channels
red1 = np.sum(red,axis=2)
blue1 = np.sum(blue,axis=2)

# Normalization
red1= normbwimage(red1)
blue1 = normbwimage(blue1)
coloredimgr = np.zeros_like(red,np.uint8)
coloredimgr[:,:,2] = np.uint8(red1)
cv2.imshow('red normalized',coloredimgr)
coloredimgb = np.zeros_like(blue,np.uint8)
coloredimgb[:,:,0] = np.uint8(blue1)
cv2.imshow('blue normalized',coloredimgb)

onlyred = np.zeros_like(red,np.uint8)
onlyred[:,:,2] = np.uint8(red1)
onlyblue = np.zeros_like(red,np.uint8)
onlyblue[:,:,0] = np.uint8(blue1)

# Matrix Difference
A,B,C = diffimage(red1,blue1,'r','b') #ceper

print("Sum signal A: " + str(np.sum(A)))
print("Sum signal B: " + str(np.sum(B)))
print("total red signal: " + str(np.sum(red1)))
print("total blue signal: " + str(np.sum(blue1)))
print("red ratio: " + str(np.sum(A)/np.sum(red1)))
print("blue ratio: " + str(np.sum(B)/np.sum(blue1)))

cv2.imshow('1 dominant',A)
cv2.imshow('2 dominant',B)
cv2.imshow('merged',C)

```

Table 1. Calculated intensity values of MDA-MB-231 cell from 2D cell culture experiment by Python script.

	I_{red}	I_{blue}	total red	total blue
cell1	0.24811	0.601853	370936	1699248
cell2	0.12966	0.745576	46242	909610
cell3	0.14683	0.740571	23703	393163
cell4	0.260138	0.74338	52859	435499
cell5	0.234709	0.598116	331735	1609806
cell6	0.25108	0.775003	44941	461736
cell7	0.140659	0.633902	96044	1016001
cell8	0.160989	0.573994	201103	1412147

(Cont. on next page)

(Cont. of Table 1)

	I_{red}	I_{blue}	total red	total blue
cell9	0.289941	0.779839	100064	868019
cell10	0.187797	0.601753	249250	1628841
cell11	0.263441	0.695259	126343	805917
cell12	0.162508	0.35013	132286	367301
cell13	0.138675	0.634424	145919	1572829
cell14	0.184417	0.875355	20002	621227
cell15	0.143032	0.799488	29448	703492
cell16	0.172033	0.536796	61875	345108
cell17	0.132037	0.60994	61804	635300
cell18	0.139501	0.492402	58902	352455
cell19	0.118756	0.678631	82104	1286580
cell20	0.125935	0.666347	22499	311863
cell21	0.29771	0.822478	95221	1040706
cell22	0.146736	0.593358	70398	597328
cell23	0.135229	0.692496	103597	1491926
cell24	0.134167	0.415579	88826	407620
cell25	0.142937	0.639382	75185	799305
cell26	0.153284	0.686013	80189	967778
cell27	0.201583	0.695489	51612	466887
cell28	0.102166	0.723587	25168	578993
cell29	0.095399	0.699462	21260	469180
cell30	0.182242	0.368745	278557	730152

Table 2. Calculated intensity values of MCF-7 cell from 2D cell culture experiment by Python script.

	I_{red}	I_{blue}	total red	total blue
cell1	0.357456	0.418927	279630	362387
cell2	0.346408	0.451804	223676	347818
cell3	0.21641	0.427384	225347	609001
cell4	0.350676	0.189122	353530	152675
cell5	0.298835	0.570611	100975	314841
cell6	0.226939	0.501145	96660	330781
cell7	0.422273	0.478863	179904	226167
cell8	0.228997	0.52022	98060	357984
cell9	0.2616	0.421795	134971	277916
cell10	0.217909	0.324323	243007	418638
cell11	0.276844	0.538604	105183	320729
cell12	0.386026	0.484353	205109	306427
cell13	0.1712	0.451294	48665	193768
cell14	0.113186	0.454469	37371	243927
cell15	0.273967	0.625192	121934	538997
cell16	0.266783	0.29562	125800	145105

(Cont. on next page)

(Cont. of Table 2)

	I_{red}	I_{blue}	total red	total blue
cell17	0.250561	0.42739	110103	245803
cell18	0.180157	0.387961	197643	570123
cell19	0.21686	0.465662	67807	213397
cell20	0.19384	0.457853	72907	256069
cell21	0.223443	0.329727	92539	158210
cell22	0.148154	0.591774	42390	353319
cell23	0.222739	0.489255	76265	254934
cell24	0.104686	0.491647	29626	245045
cell25	0.157281	0.417813	61720	237329
cell26	0.227995	0.484948	69299	220936
cell27	0.185616	0.538437	46426	237617
cell28	0.196999	0.365081	66077	154872
cell29	0.159438	0.588548	41549	313329
cell30	0.124076	0.446628	61556	350733

Table 3. Calculated intensity values of NIH 3T3 cell from 2D cell culture experiment by Python script.

	I_{red}	I_{blue}	total red	total blue
cell1	0.369091	0.543284	635040	1291261
cell2	0.418339	0.603532	384336	813475
cell3	0.387522	0.564281	432823	885919
cell4	0.383948	0.534253	783924	1442835
cell5	0.333286	0.581612	406382	1130087
cell6	0.331342	0.556384	370414	937526
cell7	0.340486	0.542118	511800	1173722
cell8	0.365218	0.51213	729601	1331171
cell9	0.315696	0.616043	382232	1329336
cell10	0.328722	0.498352	532217	1079691
cell11	0.387091	0.517178	605369	1026728
cell12	0.325237	0.582503	430066	1244891
cell13	0.45134	0.63444	515311	1087178
cell14	0.32137	0.48715	302669	607112
cell15	0.384467	0.536949	563400	1045953
cell16	0.333246	0.637603	312336	1099486
cell17	0.248584	0.70374	118582	851462
cell18	0.270114	0.620709	309948	1370606
cell19	0.333087	0.578608	315329	866911
cell20	0.254946	0.584324	269357	1106538
cell21	0.309801	0.674415	269928	1245670
cell22	0.333168	0.568192	320816	844918
cell23	0.300653	0.627259	369883	1447879
cell24	0.417289	0.65121	492606	1284319

(Cont. on next page)

(Cont. of Table 3)

	I_{red}	I_{blue}	total red	total blue
cell25	0.363034	0.664649	601068	2090189
cell26	0.310242	0.47689	248189	503041
cell27	0.273349	0.574785	205623	738887
cell28	0.246589	0.56998	238692	966647
cell29	0.323907	0.625917	245219	856423
cell30	0.326881	0.562844	367453	974214

VITA

Müge YÜCEL

EDUCATION

Ph.D. in Bioengineering, Izmir Institute of Technology (2022)

M.Sc. in Chemistry, Izmir Institute of Technology (2016)

B.Sc. in Chemistry, Izmir Institute of Technology (2014)

ACADEMIC EXPERIENCE

1. Synthesis of conformational change responsive polythiophene polyelectrolytes and developing of microfluidic platform (μ -DNAmet) for DNA methylation monitoring, TUBITAK – 116z547, 2018-2019.

2. Characterization of Electrostatically Driven Particle Formation of Conjugated Polyelectrolyte-DNA Complexes by Light and Neutron Scattering, TUBITAK – 2214-a, Mar 2021-Nov 2021.

PUBLICATIONS

1. Yucel, M., Koc, A., Ulgenalp, A., Akkoc, G. D., Ceyhan, M., & Yildiz, U. H. (2021). PCR-Free Methodology for Detection of Single-Nucleotide Polymorphism with a Cationic Polythiophene Reporter. *ACS sensors*, 6(3), 950-957.

2. Aydın, H. B., Cheema, J. A., Ammanath, G., Toklucu, C., Yucel, M., Özenler, S., ... & Yildiz, U. H. (2020). Pixelated colorimetric nucleic acid assay. *Talanta*, 209, 120581.

3. Yucel, M., Özenler, S., Tüncel, O., Kaya, H., Özçelik, S., & Yildiz, U. H. (2019). Single chain cationic polymer dot as a fluorescent probe for cell imaging and selective determination of hepatocellular carcinoma cells. *Analytical chemistry*, 91(16), 10357-10360.

4. Yucel, M., Akin, O., Cayoren, M., Akduman, I., Palaniappan, A., Liedberg, B., ... & Yildiz, U. H. (2018). Hand-held volatilome analyzer based on elastically deformable nanofibers. *Analytical chemistry*, 90(8), 5122-5129.

5. Yildiz, B., Ozenler, S., Yucel, M., Yildiz, U. H., & Yildiz, A. A. (2021). Biomimetic and synthetic gels for nanopharmaceutical applications. In *Nanopharmaceuticals: Principles and Applications Vol. 1* (pp. 273-309). Springer, Cham.

6. Yucel, M., Özenler, S., & Yildiz, Ü. H. (2020). Conformational Switching in Nanofibers: A New Bioelectronic Interface for Gas Sensors. In *Switchable Bioelectronics* (pp. 125-160). Jenny Stanford Publishing.

7. Yildiz, U. H., Yucel, M and Ozenler, S. (2021). Tek Zincirli Konjuge Polimer Nokta Üretimi ve Biyolojik Prob Olarak Kullanılması (Turkey Patent No.TR 2020 06455 B). Turkish Patent and Trademark Office.

8. Yucel, M., Groehn, F., Yildiz, U. H. Nanophase Separation for Preparation of Polymer Dots: From Photophysical & Colloidal Characterization to Polyelectrolyte Complexes. (in preparation)

9. Yucel, M., Onbas, R., Yildiz, A. A., Yildiz, U. H. Behavioral Investigation of Ultra-Small Fluorescent Polymer Dots in 2D and 3D Spheroid Model of Triple Negative Breast Cancer. (in preparation)